ADVANCED MATERIALS INTERFACES
www.advmatinterfaces.de

Mechanical, Elastic, and Adhesive Properties of Two-Dimensional Materials: From Straining Techniques to State-of-the-Art Local Probe Measurements

Cinzia Di Giorgio, Elena Blundo, Giorgio Pettinari, Marco Felici, Fabrizio Bobba, and Antonio Polimeni**

2D materials, such as graphene, hexagonal boron nitride (hBN), and transition-metal dichalcogenides (TMDs), are intrinsically flexible, can withstand very large strains (>10% lattice deformations), and their optoelectronic properties display a clear and distinctive response to an applied stress. As such, they are uniquely positioned both for the investigation of the effects of mechanical deformations on solid-state systems and for the exploitation of these effects in innovative devices. For example, 2D materials can be easily employed to transduce nanometric mechanical deformations into, e.g., clearly detectable electrical signals, thus enabling the fabrication of high-performance sensors; just as easily, however, external stresses can be used as a "knob" to dynamically control the properties of 2D materials, thereby leading to the realization of strain-tuneable, fully reconfigurable devices. Here, the main methods are reviewed to induce and characterize, at the nm level, mechanical deformations in 2D materials. After presenting the latest results concerning the mechanical, elastic, and adhesive properties of these unique systems, one of their most promising applications is briefly discussed: the realization of nano-electromechanical systems based on vibrating 2D membranes, potentially capable of operating at high frequencies (>100 MHz) and over a large dynamic range.

1. Introduction

The never-ending quest towards the optimization of the performances of electronic and photonic devices demands the development of new methods for tuning the properties of the underlying materials. Such methods can be static —e.g., via the introduction of dopants in semiconductors—or dynamic, for example through the application of external electric fields. While static methods are often essential to make a material suited to a specific application, by permanently altering its properties, dynamic ones potentially enable their real-time modulation, paving the way for the development of reconfigurable devices.

Within this context, strain engineering has historically been regarded as a "static" tuning method, which exploited the crystal deformations induced by the juxtaposition of materials with different lattice constants to manipulate the properties of semiconductor heterostructures[1] and improve the performance of electronic devices (e.g., CMOS-based logic technologies[2]). In recent years, however, strain-engineering paradigms have begun to shift, leading to the development of new devices, capable of generating a dynamic modulation of the mechanical deformations induced in the active materials (and, thus, of their optoelectronic properties).

Micro- and nano-electromechanical systems (MEMS and NEMS), for example, have long been used for sensing applications, thanks to their ability to transduce external stresses (e.g., applied pressure/weights, molecule adsorption,...) into electrical signals. In the opposite regime they are, at least in principle,

C. Di Giorgio, F. Bobba
Department of Physics E.R. Caianiello
University of Salerno
Fisciano 84084, Italy
E-mail: fbobba@unisa.it

C. Di Giorgio, F. Bobba
INFN
Sezione di Napoli
Gruppo Collegato di Salerno
Complesso Universitario di Monte S. Angelo
Naples 80126, Italy

The ORCID identification number(s) for the author(s) of this article can be found under https://doi.org/10.1002/admi.202102220.

DOI: 10.1002/admi.202102220

E. Blundo, M. Felici, A. Polimeni
Physics Department
Sapienza University of Rome
Rome 00185, Italy
E-mail: antonio.polimeni@uniroma1.it

G. Pettinari
Institute for Photonics and Nanotechnologies (CNR-IFN)
National Research Council
Rome 00156, Italy

F. Bobba
SuPerconducting and other INnovative Materials and Devices Institute (CNR-SPIN)
National Research Council
Fisciano 84084, Italy

capable of converting an applied electric field into a controlled mechanical deformation; in order to achieve a useful, real-time modulation of the material's properties, however, the electromechanical response of these devices has to be fast, reproducible, and it must extend over a large dynamic range. With these requirements in mind, in the last few decades considerable research efforts have been devoted to the development of novel piezoelectric devices, which—when compared to traditional, electrostatically actuated MEMS/NEMS structures—are characterized by a wide dynamic range, low power consumption, and low hysteresis. As in countless other fields, the rise of two-dimensional (2D) materials, such as graphene, hexagonal boron nitride (hBN), and transition-metal dichalcogenides (TMDs) has certainly provided a boost to this emerging research area. Indeed, these materials are inherently flexible, and they can boast exceptional resilience to mechanical deformations.[3–6] Furthermore, in the monolayer limit, TMDs—and particularly MoS_2—are known to display strong piezoelectricity,[7,8] due to the lack of central symmetry of the atomic arrangement in their unit cell. As such, 2D materials are excellent candidates for the realization of novel piezoelectric NEMS devices, displaying nm-level sensing and actuation capabilities.

In addition, strain is known to trigger a variety of effects in the electronic properties of these materials, ranging from a direct-to-indirect bandgap transition in TMD monolayers[9] to the emergence of strain-induced localized states—which have given ample evidence of their ability to emit single photons, both in TMDs[10,11] and in hBN[12]—and to the generation of huge pseudomagnetic fields in graphene.[13] Finally, exfoliated 2D layers are also straightforward to pick up and deterministically transfer on the substrate of choice,[14] thus making it relatively easy to achieve good mechanical coupling with any straining device, or, e.g., to fabricate MEMS/NEMS resonators based on suspended, vanishingly thin, membranes.[15,16]

The goal of the present work is to present the current state of the art on the study of the elastomechanical properties of 2D materials.

To date, a large number of original research and reviews have been devoted to mechanics of 2D materials, as well as to the technical advancements of their related measurements techniques. For instance, Zhang et al.[17] reviewed the progress of experimental and theoretical studies on the fracture behavior of graphene; Megra et al.[18] reviewed the adhesion properties of 2D materials, mainly focusing on measurement methods and adhesion; Al-Quraishi et al.[19] focused on the development of experimental techniques—including AFM-nanoindentation, micro-/nano-mechanical devices, and pressurized bulge testing—to visualize and quantify the mechanical properties of 2D materials; Wei et al.[20] reviewed the use of in situ techniques based on scanning electron microscopy (SEM), atomic force microscopy (AFM) and transmission electron microscopy (TEM), for the mechanical investigation of 2D materials; Cao et al.[21] focused on the most insightful results of nanoindentation experiments; Akinwande et al.[22] comprehensively reviewed the theoretical and experimental studies related to the mechanics of 2D materials as well as addressed the coupling between the mechanical properties and other physical properties. As the study of the mechanics of 2D materials expands extremely fast, the quest for updated reviews stating the state of the art in this field increases accordingly. Thus, starting from a pre-existing very rich background, we will review recent advancements in the mechano-elastic studies of 2D membranes. In particular, we will focus on the novel straining production strategies, on one side, and on the most recent and intriguing results obtained by local probe measurements, on the other.

Our work is structured as follows. In Section 2, we begin by surveying the main methods developed to induce mechanical deformations in these materials, either statically or dynamically. First of all, we mention substrate-driven deformations, which in recent years went from being a nuisance—associated with the unwanted wrinkling phenomena unavoidably associated with the growth/transfer of 2D materials on a substrate with different structural properties and/or thermal expansion coefficient—to being exploited for the realization of controlled deformation methods. As discussed in greater detail in the following Section, these methods mainly rely on pre-stressed[23] or patterned[24–30] substrates, as well as on local heating protocols.[31] This latter method also allows for the achievement of a dynamic, albeit slow (<3 Hz modulation frequency) control of the obtained lattice deformations. Afterwards, Section 2 moves on to the description of membrane indentation methods, which typically rely on an AFM tip to achieve a controlled, real-time deformation of a suspended 2D membrane.[32,33] Third, Section 2 also includes a thorough examination of blisters and bubbles, characterized by a similar, dome-like shape and by the establishment of a strong (few %) biaxial strain at their summit.[9,34–39] Bubbles, in particular, display a high durability (up to several years) and can be fabricated with precisely controlled size and position.[39] The final part of Section 2 is devoted to the discussion of the main methods for the characterization of the morphology and of the electronic properties of mechanically deformed 2D materials. In Section 3, we discuss recent experiments aiming at the identification of the analytical relationships existing between the applied stress and the elastic properties of the materials, providing an overview of the methods which can be employed to probe the Young's modulus of 2D materials, and collecting the values obtained for the most common materials with those methods. In Section 4, instead, we show how, besides allowing for the measurements of the elastic parameters of 2D materials, some specific microscopic mechanical deformations—insofar an accurate model to describe them is developed—can be exploited also to achieve precious information on the adhesion properties of the material with the underlying substrate. In the same section, we collect the adhesion energies measured for a variety of 2D material/substrate combinations with various methods. Finally, in Section 5 we provide an overview of the prospective applications that can arise from the development of innovative strain engineering protocols in 2D materials. In particular, we focus on the fabrication of NEMS resonators based on thin layers, especially with respect to the possibility of modulating the device properties over a large dynamical range and at a high speed (nanomechanical oscillators based on 2D materials can reach frequencies in excess of 100 MHz).[16]

2. Mechanically Deforming Two-Dimensional Materials on a Mesoscopic Scale

Deformation methods leading to controlled elastic strains are an appealing means to modulate the electronic, optical and

transport properties of semiconductor materials and their nanostructures. Furthermore, mechanical deformations are an unavoidable presence in most instances, like in lattice-mismatched heterostructures[40] or in CMOS technologies, where stress may offer beneficial effects.[2] The rigidity of semiconductor bulk crystals, though, limits the number of techniques that can be employed to deform reversibly samples and devices. Likewise, nanostructures, such as quantum wells and quantum dots, are typically embedded in a bulk lattice and cannot be easily stressed. Apart from the strain inherent to lattice mismatch growth,[41] the main methods to induce strain are hydrostatic pressure[42] and bending devices.[43] Hydrostatic pressure can be applied to three-dimensional semiconductors[44] and bulk-embedded nanostructures[45] using anvil[42] or clamp cells[46] via a suitable transfer medium. Bending is instead particularly suited for micro- and nano-wires.[47] On the contrary, the nearly all-surface nature of two-dimensional (2D) crystals, along with their exceptional flexibility and robustness,[32] boosts the number of methods—as well as their effectiveness—that can be exploited to modify and control the physical properties of these materials. In addition, those same methods can be used to characterize the elasto-mechanical response to external mechanical perturbations.

Differently from 3D semiconductors, in 2D materials it is possible to create strain gradients on a mesoscopic scale. Since the earliest investigations of 2D materials, the morphology of high-quality crystals has been the subject of much attention, given the theoretical expectations of truly new fascinating phenomena occurring because of rippling, bending, and straining the 2D membranes. It was immediately clear that this class of materials is unavoidably affected by intrinsic uncontrollable deformations, showing up as local nanometer-size strained areas, with random spatial distribution. For instance, early electron-diffraction studies of free-standing graphene monolayers indicated the presence of an intrinsic rippling, with ≈1 nm-high out-of-plane corrugations over a characteristic lateral scale of 10–25 nm.[48] These corrugations, observed many times in graphene monolayers deposited on top of insulating substrates,[49–54] were theoretically argued as necessary to stabilize the suspended sheets against the thermal instabilities present in ideal 2D systems.[55] However, Lui et al.[56] were able to demonstrate that the rippling can be eventually fully suppressed by depositing the graphene onto an appropriate substrate. Indeed, a topographic corrugation less than 25 pm in height, over micrometer-length scale, was demonstrated by performing non-contact atomic force microscopy (AFM) of graphene mechanically exfoliated on mica. The finding of the so-called ultraflat graphene first demonstrated the importance of the appropriate substrate selection, as atomically thin membrane may simply reflect the roughness of their underlying support.

However, uncontrolled substrate-driven deformations may also arise because of the fabrication strategy. As the quest for large coverage of high-quality 2D materials increased, chemical vapor deposition (CVD) growth was widely adopted to this aim, disclosing new experimental challenges and opportunities. The CVD growth of 2D materials, indeed, is profoundly affected by the presence of wrinkles, originating during the post-growth cooling, because of the different thermal expansion coefficient between the 2D sheet and the metallic substrate.[57–62] The epitaxial growth of vertical stacks of thin films, or planar heterostructures, also generally gives rise to strain at the interface. However, this approach is not suitable for planar stacks of 2D heterostructures given the weak van der Waals interaction between the 2D layers, and the ease of interlayer sliding. A more effective procedure to transfer controllable amounts of strain on 2D crystals relies on stitching them side by side, to build lateral 2D heterojunctions and superlattices. To date, epitaxial growth of lateral 2D heterostructures has been successfully explored in several 2D materials, including MoS_2/$MoSe_2$,[63] MoS_2/WS_2,[64,65] $MoSe_2$/WSe_2,[66,67] WS_2/WSe_2.[68] For instance, Xie et al.[68] used a sophisticated application of metal-organic CVD to grow a lateral heterostructure made by alternating WS_2 and WSe_2 monolayers in the same growth plane. The resulting superlattice was then affected by a tensile (compressive) strain within the WS_2 (WSe_2) region.

Additionally, uncontrollable deformations take place when transferring and manipulating 2D materials. During this process, gases or liquids (e.g. air, water and/or hydrocarbons) get trapped between the 2D layer and its substrate, or in between stacks of 2D heterostructrures, giving rise to spontaneously formed nanometer-size blisters.[38,69–72] These nanometric protrusions have been used as the signature of adhesion quality between the 2D material and its substrate, thus ensuring the presence of contaminant-free large inter-blisters areas.[73]

However, while all the examples above enable the observation of interesting effects and can be exploited to investigate several material properties, their formation is almost uncontrollable, and their spatial distribution is random. For this reason, a huge effort has been devoted to developing experimental approaches for obtaining controllable deformations of 2D materials. Such deformations were created, for instance, by (i) exploiting the mismatch between the thermal coefficient expansion of the 2D crystal and that of the substrate on which growth occurs;[74] (ii) transferring the 2D crystal on top of pre-stretched elastomeric substrates, to be relaxed afterwards;[23] (iii) using pre-patterned, 3D-micro and 3D-nanostructured interfaces. Several geometries, such as nanorods, nanotents,[24–27] nanogaps,[28] nanowires,[29] and nanocones[30] were used as substrate architectures, and, due to the exceptional flexibility of single- and multiple-layered 2D materials, these latter exhibited the capability of conforming to the underneath substrate shape.

Other techniques to induce strain at the micro-scale were developed, based on indentation or bulging of a 2D material. These classes of straining methods hold particular relevance since—besides giving rise to intriguing phenomena such as carrier funneling, pseudo-magnetic fields, and much more—at the same time they represent unique platforms to explore the mechano-elastic and adhesive properties of the layered materials. In the following subsections we will thus describe these methods in more detail.

2.1. Indented Membranes

Indentation of 2D crystals is usually achieved by pressing the membrane with the tip of an atomic force microscope. To make

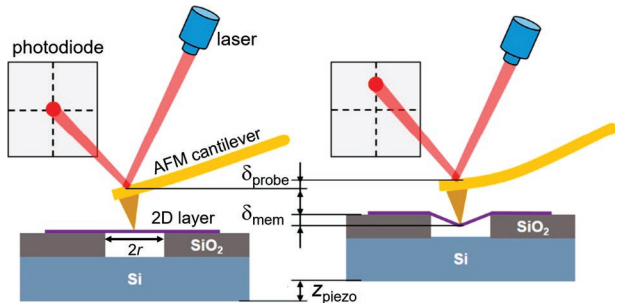

Figure 1. Sketch of an indentation experiment using an atomic force microscope on a 2D layer deposited over a microcavity with radius *r* created on a Si/SiO_2 substrate. The reflection of the laser by the microscope cantilever is monitored on a photodiode. The indentation depth δ_{mem} is determined by z_{piezo}–δ_{probe}, where z_{piezo} is the moving distance of the sample stage and δ_{probe} is the deflection of the AFM tip. Reproduced with permission.[75] Copyright 2019, American Chemical Society.

this method effective, the membrane is held suspended on micrometer-sized apertures created by lithography on a suitable substrate.[32,33,75,76]

Figure 1 shows the sketch of an indentation experiment. The tips feature a relatively large radius of the order of few tens of nm to avoid abrupt fractures of the samples. The tip pressure induces a biaxial strain leading to a vertical deflection, δ_{mem}. This latter is equal to the difference between the height variation of the piezo stage, z_{piezo}, and the deflection of the microscope tip, δ_{tip}, namely $\delta_{mem} = z_{piezo} - \delta_{tip}$. Indenting is a particularly insightful technique since the known applied force is proportional to δ_{mem} via constants that depend on the elasto-mechanical properties of 2D crystals. Typically:

$$F = A \cdot \delta_{mem} + B \cdot \delta_{mem}^3 \quad (1)$$

A and *B* are coefficients that depend on the specific geometry of the aperture on which the membrane is deposited and on the thickness of the membrane itself. Importantly, as it will be discussed in Section 3.1, those coefficients contain information on the elastic properties of the 2D crystal, comprising the in-plane Young's modulus, the Poisson's ratio and the tension of the membrane before the indentation is applied.[4,75,78] Indentation is a technique employed not only for determining the elastic and mechanical properties of 2D materials, but also to tune the crystal band gap and, thus, to characterize the material's opto-mechanical properties.[79]

As schematically shown in **Figure 2**, it is indeed possible to perform optical measurements while indenting the sample. In this manner, the exciton diffusion[77] and charge state[80] could be dynamically modified under the AFM tip action, thus proving the versatility of this method and the wide range of effects it allows to observe. It is worth mentioning that indentation can also be employed on 2D crystals deposited on soft substrates made of polymeric materials.[79] Indeed, it was shown that permanent deformations of monolayers over nanometer-sized regions can be achieved after indentation, resulting in strain-modulated patterns[81] or in the formation of single-photon emitters.[82]

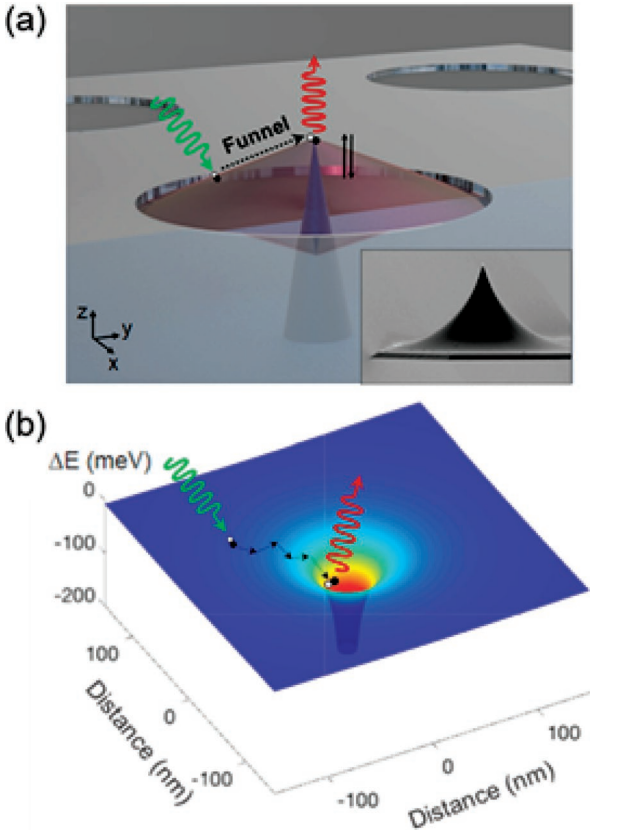

Figure 2. a) Sketch of an indentation experiment, where the AFM tip presses a WSe_2 monolayer on the bottom side (see scanning electron microscope image in the bottom-right inset). The strain gradient so created acts as a funnel for excitons that drift toward the highest-strain region located right above the AFM tip. b) Variation of the WSe_2 band gap due to the tensile strain caused by the tip. The band gap reaches a minimum at the tip location. Reproduced with permission.[77] Copyright 2020, American Chemical Society.

2.2. Bulging Membranes

2.2.1. Wrinkles

The interest for wrinkles in 2D materials is intrinsically related to the isolation and deposition methods. In fact, single layers of these crystals are commonly isolated by making bulky flakes stick to a polymeric film. From time to time, single layers remain on the film, which is then brought in contact with the desired substrate and slowly peeled off. With this procedure, the monolayer (ML) flake remains on the substrate. The use of polymeric films for this process may be exploited to induce wrinkles in the ML, as demonstrated in a series of earlier studies on thin films. For instance, Bi-oriented polypropylene films (with thicknesses from 15 μ to 90 μm) were deposited on a soft polymeric substrate (vinylpolysiloxane) and therein adhered by van der Waals (vdW) forces. Relative to this initial state, the polymeric substrate is then uniaxially compressed in a linear stage, as shown in **Figure 3**a. For the adhered thin film, however, compression is energetically expensive compared with bending. Therefore, above a critical value of substrate compression, the thin film wrinkles with a well-defined periodicity

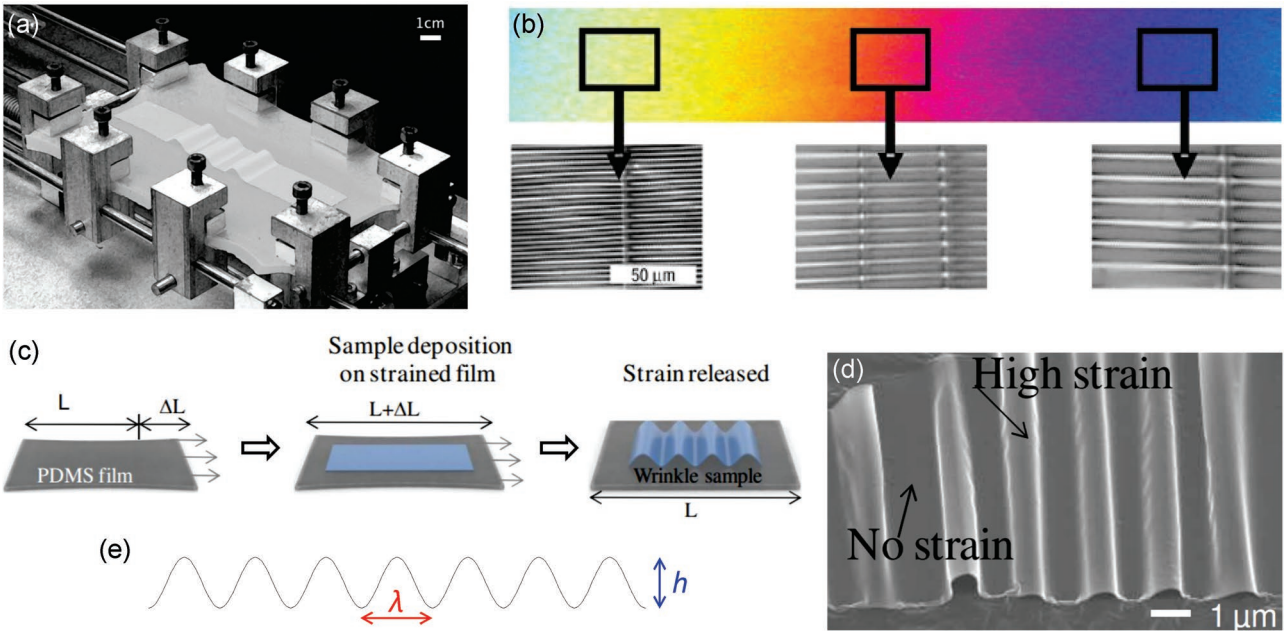

Figure 3. a) Macroscopic experimental setup for studying the delamination of thin films stick to soft substrates. The thin film stick to a soft polymeric substrate by van der Waals forces, which is then uniaxially compressed in a linear stage. Since compression is energetically expensive compared with bending for the thin film, the substrate compression results in a wrinkling of the film. Reproduced with permission.[83] Copyright 2009, The Authors, published under an exclusive License by the National Academy of Sciences. b) Optical micrograph of a polystyrene thickness gradient on a silicon wafer (140 to 280 nm). Greyscale insets show optical micrographs of the film after transfer to PDMS and application of strain to induce buckling. The doubling of the film thickness from left to right results in a doubling of the buckling period. Reproduced with permission.[84] Copyright 2004, Springer Nature. c) Schematic diagram demonstrating the process to induce periodic wrinkle structures in 2D materials using flexible substrates. d) SEM image showing periodic wrinkle structures in a 2D flake. c,d) Reproduced with permission.[85] Copyright 2017, American Chemical Society. e) Sketch of a periodic wrinkle structure, highlighting the meaning of wavelength (λ) and height (*h*).

(or wavelength).[83,84] Under further compression wrinkling becomes unstable: the thin film locally de-bonds and buckles further out of plane. Analogous results can be obtained if the substrate is stretched prior to the thin film deposition, and the polymer strain is then released.

The wrinkles are typically characterized by a sinusoidal profile described as:

$$h(x) = \frac{h_0}{2}\left[1+\cos\left(\frac{2\pi x}{\lambda}\right)\right] \quad (2)$$

where h_0 is the maximum height and λ is the periodicity. Interestingly, the periodicity itself depends on the thin film thickness, as highlighted in panel (b) for a film with variable thickness. As we will discuss in the following sections, λ embeds information both on the film thickness and the elastic parameters of the thin film and the substrate.

Recently, the same procedure just discussed was applied to 2D materials deposited on PDMS (polydimethylsiloxane). In this case, as sketched in Figure 3c, the PDMS is initially stretched; a 2D flake is then deposited on the PDMS and finally the strain is released, resulting in the wrinkling of the 2D material. The wrinkles, such as those in Figure 3d, host tensile strains of the order of 1%,[85,86] while the regions outside are expected to be flat and strain-free. The way the strain is transferred from the PDMS to the monolayer is however nontrivial, and the expected strain often differs from the nominal one in the wrinkle geometry. To this respect, it should be noticed that the Young's modulus of the PDMS is about two orders of magnitude lower than that of layered crystals, resulting in a non-complete strain transfer. Lee et al. showed how, by exposing the PDMS to O_2 plasma, the PDMS surface stiffness increases remarkably (up to about 70 GPa), resulting in a more effective strain transfer.[87] Regardless of the effectiveness in the strain transfer, the top parts of the wrinkles always show a redshift of the photoluminescence (PL) and Raman peaks with respect to the valleys (i.e., the regions between wrinkles), indicating the presence of a larger tensile strain or of a reduced compressive strain on the tops.[85–87] This geometry, in which the strain varies on the micro- or nano-meter scale, is particularly interesting since the consequent local bandgap variation leads to exciton funneling.[86,87] A sketch of the exciton funneling process is provided in **Figure 4**a: indeed, the photoexcited electron-hole pair drifts toward the band gap minimum and thus toward the wrinkle top.

Figure 4b shows the microscope view, PL intensity, and PL peak energy maps of triangular 1L-WS_2, with and without the wrinkled strain profile. In the absence of strain (ε_{xx} = 0%) the PL emission is spatially uniform (apart from marginal variations at the center and at the edges). By applying a uniaxial 5% compressive strain to the substrate (ε_{xx} = 5%), periodic lines of PL contrasts appear in the 1L-WS_2 flake, due to the wrinkle formation. The top regions of the wrinkles exhibit lower PL peak energy values than the valley regions. Some representative PL spectra of the unstrained flake, and of the top and valley regions of the wrinkled 1L-WS_2 are shown in Figure 4c,

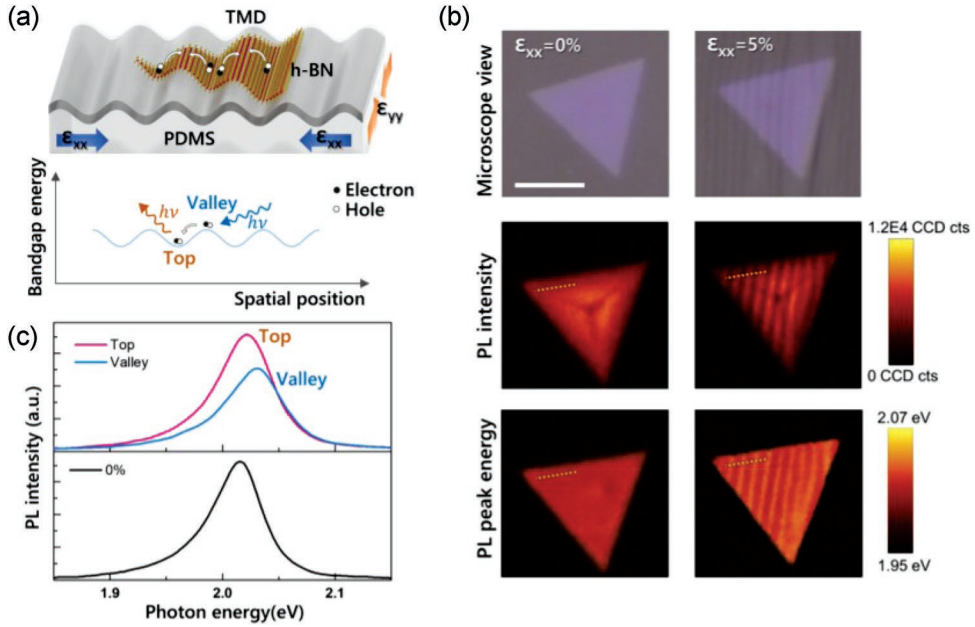

Figure 4. Switchable funneling of 2D excitons by variable uniaxial strain modulation on an O_2 plasma-treated PDMS bilayer substrate. a) Schematic of tunable exciton funneling. Photoexcited excitons drift from the high band gap region (valley) to the low band gap region (top). b) Microscope view, integrated PL intensity, and peak energy mapping of a 1L-WS_2 with (a ε_{xx} = 5%; strain value was applied to the substrate) and without (ε_{xx} = 0 %) uniaxial strain. Dotted lines show the location of cross-sectional profiles shown in Figure 2. Scale bar: 5 µm. c) Representative PL spectra of the top and valley region with (top panel, ε_{xx} = 5%) and without (bottom panel, ε_{xx} = 0 %) uniaxial strain. Reproduced with permission.[87] Copyright 2021, American Chemical Society.

showing how the PL peak in the top region is red-shifted by ≈20 meV and that the PL intensity is ≈30% higher compared to the valley regions.[87]

2.2.2. Blisters

Another approach to induce controllable and high biaxial strain fields is based on the bulging of a 2D membrane obtained by establishing a pressure difference between the two sides of the membrane itself. **Figure 5** shows a method, which exploits the pressure difference Δp that can be created between the sides of a 2D layer sealing a cavity in order to make it bulge upwards or downwards, as shown in panel (a). The cavity is usually formed by etching cylindrical micro-holes on a Si/SiO_2 substrate. The 2D sample is then deposited over the hole and the system (cavity+membrane) is pressurized by N_2, Ar, He or H_2 up to about p_{int} = 1000 atm.[34–37] When the system is removed from the pressurization chamber and is brought to ambient pressure (1 atm) a sizable $\Delta p = p_{\text{int}} - p_{\text{ext}} > 0$ establishes and the membrane bulges upwards. A sketch of the device is shown in Figure 5b, while optical images of real devices can be observed in panel (c). Such a bulging subjects the 2D layer to a biaxial tensile strain at the top of the inflated layer, whose extent can be in excess of 2%.[34] A deformation with the opposite concavity can be obtained if the system is first evacuated and then brought to ambient pressure in such a way that $\Delta p < 0$, as shown in the top panels in Figure 5a. The bulging method is particularly suited to investigate the elastic and adhesive properties of layered materials. In ref. [88], it was shown that by applying a tensile strain (up to 0.60%) by a bulging system like that discussed before, see **Figure 6**a, the friction on a graphene sheet can be reduced up to reaching a superlubricating state. By using the same bulging method,[35] it was possible to determine the energy needed to separate MoS_2 mono- and multi-layers from a SiO_2 substrate and the Young's modulus of a MoS_2 monolayer, thus providing complementary information to those derived by indentation experiments. One of the main drawbacks of the bulging method employing pressurization through the two sides of a membrane is the long time required to bulge the 2D layer (from several hours[37] to many days[89]). In addition, the bulge itself tends to deflate after many days, as shown in Figure 5d. This indeed limits the potential integration of the blisters into actual devices. Nevertheless, the same approach was employed to investigate the porosity of graphene to different molecular gas species in ref. [89]: By purposely creating pores on the graphene sealing membrane, the deflation of the bulge was time-monitored and selective molecular sieving effects were observed. Finally, the bulging method discussed so far can be used to characterize the response of the optical properties to the application of strain, or, the other way around, to deduce the strain status by simple and non-invasive optical techniques, such as micro-PL and micro-Raman. Figure 6a shows the AFM images of graphene layers subjected to a different pressurization, resulting in different values of the tensile strain $\Delta\varepsilon$ at the top of the inflated membrane. Figure 6b shows the evolution with strain of the G and 2D Raman modes, corresponding respectively to the doubly degenerate E_{2g} mode at the Brillouin zone center (G band) and to the second-order double resonant Raman scattering from zone boundary K+ΔK phonons (2D band).

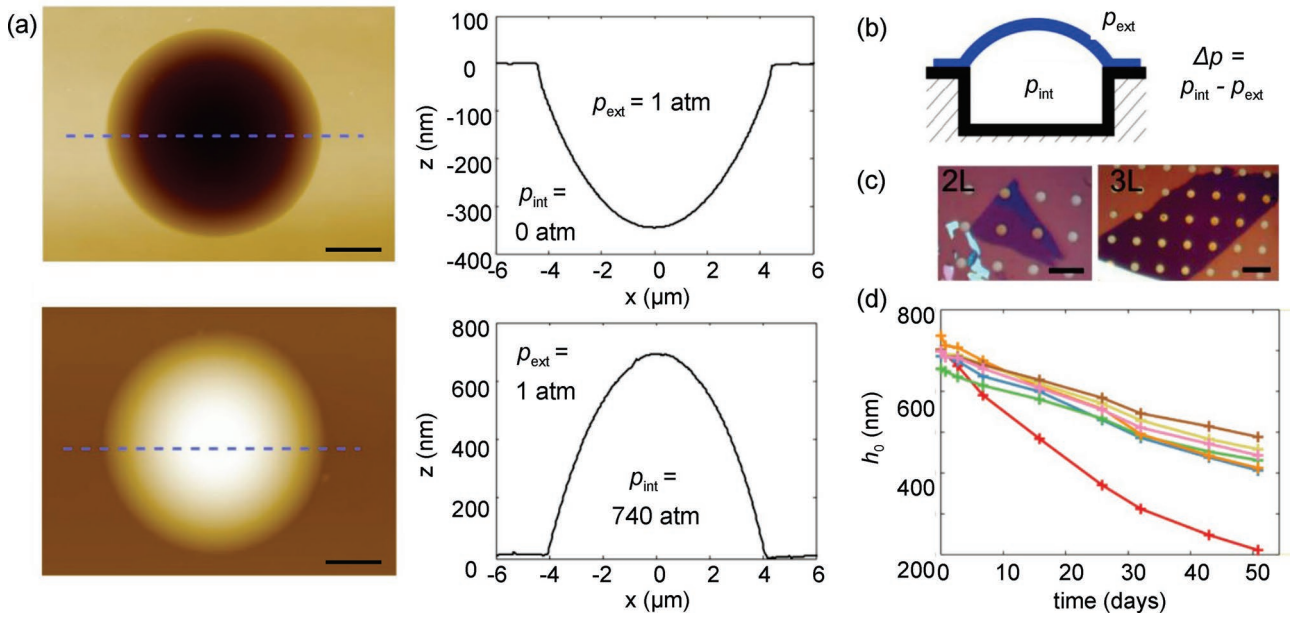

Figure 5. a) 2D AFM images (left, the scale bar is 2 μm) and AFM profiles extracted along the blue dashed lines (right) of two MoS_2 blisters. In the top one, the 2D membrane was caused to bend inside a circular cavity; in the bottom one, the 2D membrane was caused to bulge. This was obtained by applying a pressure difference between the internal and external side of the cavity, according to the sketch of panel (b). c) Optical images of two typical devices consisting of CVD-grown MoS_2 membranes suspended over cylindrical cavities after the transfer (the scale bar is 15 μm). d) The maximum height (h_m) of seven different CVD-grown MoS_2 devices pressurized with nitrogen was monitored over time for 50 days. a–d) Reproduced with permission.[34] Copyright 2016, American Chemical Society.

As expected, the measurements reveal a phonon softening upon the application of tensile strain. The exact characterization of the strain status of the membrane can indeed be exploited for a quantitative estimation of the phonon shift rates with strain.[90]

2.2.3. Bubbles

As discussed in the previous section, while the blisters are highly controllable and allow one to achieve high strains, they suffer from lack of durability. Indeed, similar structures—featuring a remarkably longer durability (several years)—can be formed directly interfacing 2D materials with a flat substrate (either a layered material or a Si or metallic substrate) rather than a holey substrate. Such structures are referred to as bubbles or domes. Among the first experimental observations of nanobubbles, Levy et al.[13] reported how, by cooling down a graphene sample after the graphene growth process, nanobubbles with irregular shape formed as a result of the differing thermal expansion coefficients of graphene and the metallic substrate, see **Figure 7**a. Scanning tunneling spectroscopy (STS) studies on those bubbles demonstrated that strain was altering the Landau levels behavior, producing an analogous effect to that expected for magnetic fields as high as 300 T. This result triggered the interest for bubbles in 2D materials, and just a few years later Lu et al.[91] reported on a method to engineer nanobubbles formed at the interface between graphene and a metallic substrate. The authors exploited the buckling instability existing for graphene grown on Ru(0001) owing to the compressive strain between lattice-mismatched Ru and graphene. The mismatch was observed to give rise to a periodic blistering of the graphene sheet, with undulating Moiré valleys and humps consisting of graphene domains attached to, or lifted off, the Ru substrate, respectively. Starting from this observation, the authors performed oxygen intercalation procedures: At high temperatures and oxygen pressure, O_2 molecules can diffuse through step edges and surface defects and permeate between graphene and ruthenium through the hump regions of the Moiré structures. The intercalated molecules cut the C–Ru bonds, leading to a local delamination of graphene from the substrate over nm-scale regions, and in turn to the convolution of different humps to form graphene nanobubbles.[91] The shape of the nanobubble varies depending on the number of humps that coalesce, as demonstrated in Figure 7a for a triangular (left), trapezoidal (center) and hexagonal (right) bubble.

Quite in the same period, Stolyarova et al.[92] demonstrated the formation of irregularly shaped graphene microbubbles, see Figure 7b. In that case, graphene flakes were deposited on a SiO_2 substrate and then irradiated with high-energy hydrogen ions (500 keV). The penetration depth of these ions was estimated to be of several μm. This process resulted in the formation of bubbles, which was attributed to an additional gas release (mostly oxygen) from the irradiated SiO_2 substrate, with the gas remaining trapped at the flake-substrate interface. Analogous results were obtained by exposing the flakes to HF vapor.

While these two examples demonstrated the possibility to create bubbles, the methods proposed to create them did not gain a widespread diffusion, while novel and somehow simpler methods were developed and became predominant. Such methods can be classified either as top-down or bottom-up methods, as sketched in **Figure 8**a–b.

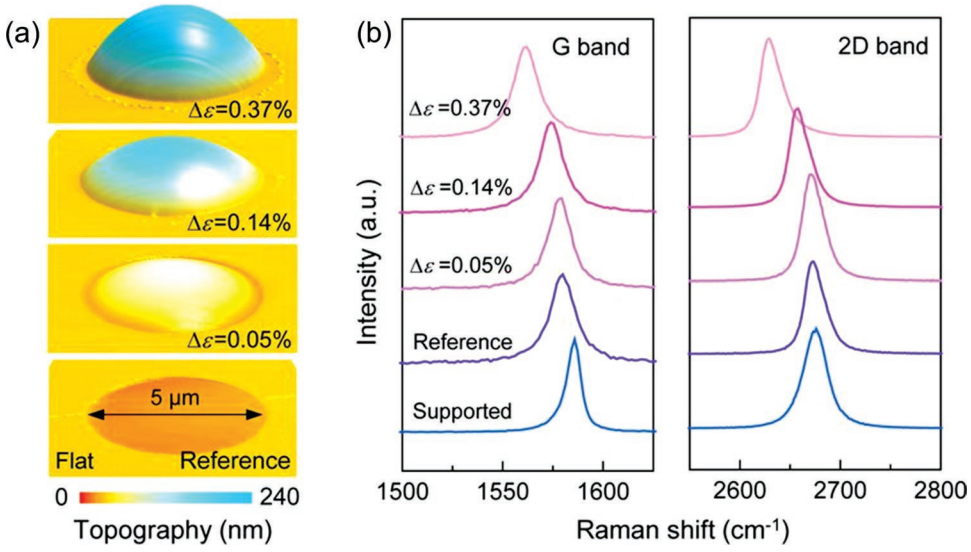

Figure 6. a) 3D atomic force microscope images of graphene pressurized in a bulging device at different differential pressures and featuring different strain values Δε. b) Micro-Raman spectra of the graphene membrane with varying strains, measured at the center region of the graphene bubble. a,b) Reproduced with permission.[88] Copyright 2019, National Academy of Sciences.

Bubble Creation via Top-Down Methods: The deposition of one-layer-thick or few-layer-thick flakes on a substrate or on a different layered crystal represents a fundamental step in the preparation of 2D materials and heterostructures. Such deposition process often leads to the formation of bubbles and sometimes wrinkles on the sample surface, which is typically due to the trapping of unavoidably present contaminants at the interface between the deposited flake and the material beneath.[38,93] Interestingly, in this process the attractive vdW forces between the thin flake and the substrate squeeze out the trapped contaminants (mostly water and hydrocarbons), leading to the formation of μm and sub-μm bubbles and leaving the surrounding interface atomically sharp. This self-cleansing process is optimized by annealing the sample. Khestanova et al.[38] verified that an annealing at 150 °C for ≈30 min is sufficient for the bubbles to reach their equilibrium shape and size.

The bubbles created with this method are characterized by various shapes: from triangular, to rhomboid, to pentagonal, etc., up to circular ones, as shown in Figure 8c. Whenever the shape is non-circular, the formation of the bubbles is accompanied by the formation of wrinkles that branch off starting from the bubble corners.

While this method is successful to form bubbles in 2D materials and allow their formation at the interface between different crystals, it presents several drawbacks: i) the bubbles form randomly, so that their shape, size and position cannot be controlled; ii) the deposition process requires the initial surface on which the 2D flake is deposited to be clean and perfectly flat; if not so, many small bubbles will form, having small aspect ratio, being extremely unstable (they can easily move under an AFM tip, for instance[72]) and leaving the surrounding areas not that clean and flat.

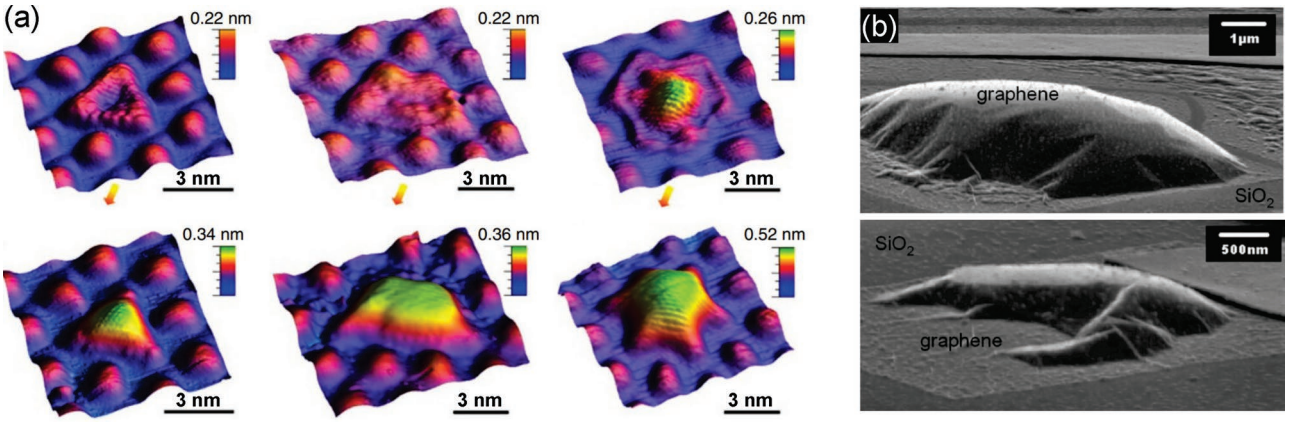

Figure 7. a) Three-dimensional scanning tunneling microscopy (STM) images ($I_{tunneling}$ = 40 pA, V_{sample} = 200 mV) of a graphene monolayer on Ru(0001), showing the coalescence of graphene humps following oxygen intercalation, to form triangular, trapezoidal, and hexagonal graphene nanobubbles. Reproduced with permission.[91] Copyright 2012, Springer Nature. (b) SEM image of a single layer graphene flake after exposure to HF vapor, taken at a 75° angle with respect to the sample plane. The formation of gas at the graphene/silicon dioxide interface lifted the flake with respect to the underlying SiO_2 substrate. Reproduced with permission.[92] Copyright 2009, American Chemical Society.

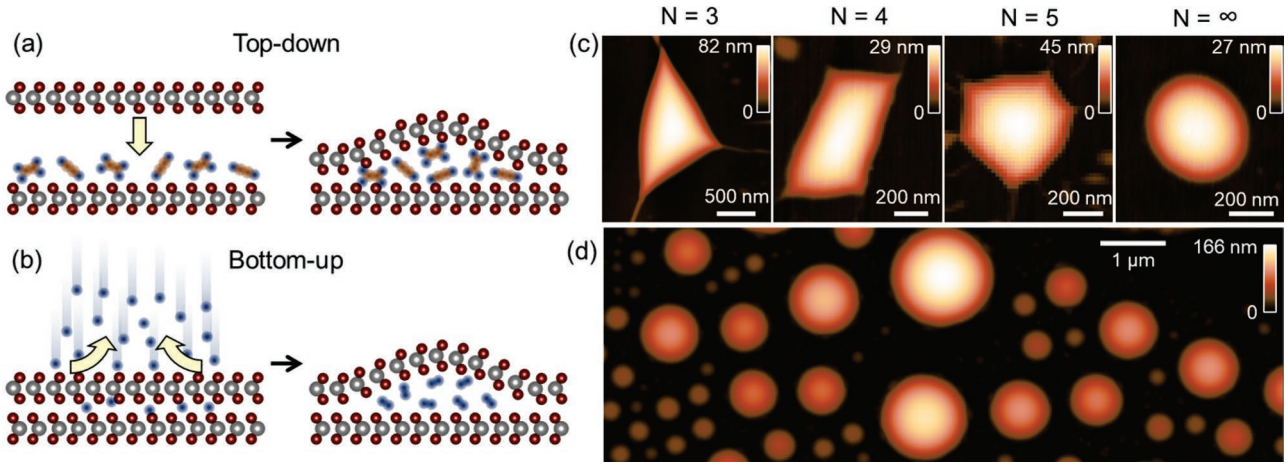

Figure 8. a) Sketch of the top-down approach: A 2D material is deposited onto another crystal and contaminants remain trapped in between; the contaminants coalesce to form a bubble. b) Sketch of the bottom-up approach: A bulk crystal is irradiated with H ions that penetrate through it; molecular hydrogen forms and coalesces. a,b) Reproduced with permission.[72] Copyright 2021, American Physical Society. c) AFM images of several TMD bubbles created by the top-down approach. The bubbles are characterized by different polygonal shapes, where *N* indicates the number of sides. d) AFM image of TMD bubbles created by the bottom-up approach.

Bubble Creation via Bottom-Up Methods: More recently, alternative methods for the creation of bubbles were developed, based on bottom-up approaches. This has the advantage that the 2D membrane constituting the dome is detached by its parent substrate via the accumulation of gases in between. In such a manner, the interface between the dome and the substrate does not enter in contact with the external environment, which guarantees an optimal cleanness and in turn the best possible adhesion.

The pioneering works where these bottom-up approaches were developed are both based on hydrogen irradiations: Either via a low-energy ionized beam—as reported by Tedeschi et al. in TMDs[39]—or via an H-plasma treatment—as reported by He et al. in hBN.[94] Unlike the first work by Stolyarova et al.,[92] in this case very mild conditions and low H beam energies are employed (<30 eV). With this process, the ions are able to penetrate only for a few nm (one or a few layers). Therein, thanks to the ground contact, hydrogen molecules form and remain trapped, see Figure 8d. This mechanism is supported by previous studies on the gas permeability of 2D crystals, showing how protons are able to penetrate through graphene, hBN and TMD MLs while hydrogen molecules cannot.[95] When using these bottom-up approaches, the bubbles are characterized mostly by a circular shape.[39,94] These methodologies present several advantages with respect to the top-down approach: i) a much higher bubble density is achieved and the size and position of the bubbles can be controlled by lithography-based methods, as demonstrated by Tedeschi et al.[39] and Blundo et al.;[6] ii) the samples can be exfoliated and kept in air since the interface where the bubbles form will anyway remain clean. The only drawback of this method if compared to the top-down ones is that the dome and the parent substrate are of the same material, while this approach has not been tested so far for heterostructured systems.

The bubbles have attracted great interest since they host high strains (total strains ≈4%) and were shown to give rise to a plethora of intriguing effects, such as behaving as second-harmonic generation or luminescence hotspots,[39] hosting pseudo-magnetic and piezoelectric fields,[13,96,97] originating funneling of the photo-generated carriers and profound modifications of the electronic properties of the material,[9] and huge Raman shifts.[72]

Indeed, the mechanical and strain properties of bubbles with arbitrary shape can be modeled numerically via finite-element method calculations.[39,72,98]

For bubbles with circular shape (with maximum height h_0 and footprint radius R), instead, analytical models were developed. The general idea is that one has to start by some assumptions on the height profile and radial displacement and the strain tensor can then be calculated by exploiting the Green–Lagrange equations. In a series of works, it was assumed that the height profile should follow the linear plate model in the case of small bubbles (*i.e.*, whenever the height of the bubble h_0 is comparable to its thickness t):[99]

$$h(r) = h_0\left[1-\left(\frac{r}{R}\right)^2\right]^2 \tag{3}$$

while the height profile should follow the membrane model for larger bubbles (i.e., for $h_0 \gg t$):[71,99,100]

$$h(r) = h_0\left[1-\left(\frac{r}{R}\right)^2\right] \tag{4}$$

For large bubbles, slightly different models were also sometimes employed, adding a fourth-order term to the membrane profile.[38,96] Coupled with these assumptions on the height profile, several different assumptions on the radial displacements were done, as discussed in more detail in ref. [72]. In all cases, however, the analytical model could not match the numerical results, either being just quantitatively discrepant[71] or being even qualitatively different.[99,100] A model capable of showing better agreement with both the experimental data and numerical results was recently proposed, assuming as height profile the following expression:[72]

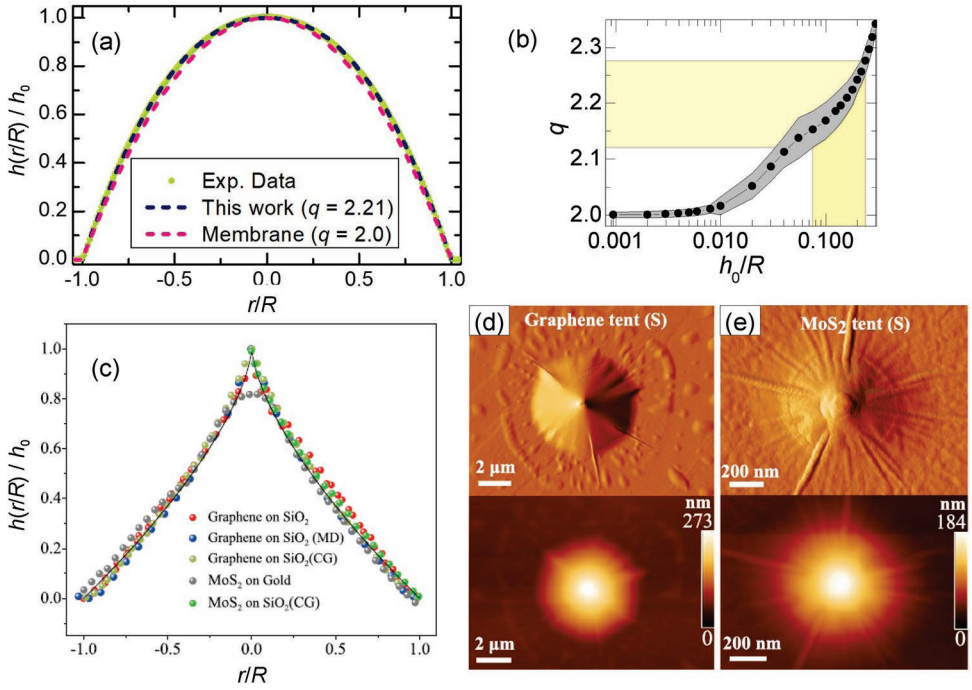

Figure 9. a) Experimental profile measured along a diameter of a WSe_2 bubble created by H ion irradiation. The data were fitted by Equation (5), resulting in a q value equal to 2.21. The membrane model is also displayed for comparison. b) Numerical calculations of the constant q in Equation (5) vs. h_0/R. The black dots concern MoS_2, while the gray-shaded area embeds other 2D materials ($MoSe_2$, $MoTe_2$, WS_2, WSe_2, WTe_2, hBN, and graphite). The orange-shaded areas highlight the range of aspect ratios measured experimentally in 2D-material bubbles. Reproduced with permission.[72] Copyright 2021, American Physical Society. c) Normalized tent profiles measured experimentally or simulated numerically (by molecular dynamics, MD, or coarse-grained modeling, CG). The black line is was drawn via Equation (5) setting $q = 2/3$. d–e) AFM phase (top) and height images (bottom) of a multilayer graphene tent on SiO_2 (d), and of a CVD-MoS_2 tent on a gold film. c–e) Adapted or reproduced with permission.[71] Copyright 2018, American Physical Society.

$$h(r) = h_0\left[1-\left(\frac{r}{R}\right)^q\right] \tag{5}$$

where q is a fitting parameter which is found to be $q \approx 2.2$. It was also shown that starting from that assumption, the strain components can be expressed as:

$$\varepsilon_r(r) = f(\nu,q)\frac{h_0^2}{R^2}\left[1-g(\nu,q)\left(\frac{r}{R}\right)^{2q-2}\right],\quad \varepsilon_\theta(r) = f(\nu,q)\frac{h_0^2}{R^2}\left[1-\left(\frac{r}{R}\right)^{2q-2}\right] \tag{6}$$

where f and g are functions of the Poisson's ratio ν and of q:

$$f(\nu,q) = \frac{q}{8}\left[\frac{2q-1-\nu}{q-1}\right],\quad g(\nu,q) = 2q-1-\frac{4q(q-1)}{2q-1-\nu} \tag{7}$$

The excellent agreement between this formulation and the experimental results is exemplified in **Figure 9**a, where the experimental profile acquired along a diameter of a WSe_2 bubble was fitted by Equation (5). The fit (blue dashed line) perfectly captures the experimental data for $q = 2.21$. The membrane profile (corresponding to $q = 2.0$) is also shown for comparison (pink dashed line). To interpret the fact that the experimental data are reproduced for q values greater than 2, we have to consider that q is expected to be equal to 2 only under the hypothesis that $h_0/R \ll 1$. To achieve a better understanding of the meaning of this condition, numerical estimates of the constant q as a function of h_0/R were obtained in ref. [72], and are displayed in Figure 9b. Indeed, $q \approx 2.0$ for $h_0/R < 0.01$, while it is larger for the aspect ratios typically measured in 2D-material bubbles, whose range is highlighted by the orange-shaded area. Indeed, for the real aspect ratio, a q value around 2.2 is estimated numerically, in excellent agreement with the experiments. Interestingly, this model can also be adapted to different kinds of deformations, such as those obtained by depositing 2D materials on a protruding object, namely tents. The experimental and numerical profiles of 2D tents were analyzed by Dai et al.,[71] showing how they are well reproduced by setting $q = 2/3$, as shown in Figures 9c–d.

To conclude this section, it should be noticed that remarkably high total strains—of the order of 4%—are obtained in the bubbles. Interestingly, strain is purely uniaxial at the edges, and it becomes equi-biaxial at the bubble summit. Furthermore, the strain magnitude increases from the edges to the center, as highlighted by Equations (6) and shown in **Figure 10**a, where the AFM profile of a WS_2 bubble and the corresponding strain distribution (estimated via finite element method, FEM, calculations) are displayed.

Such a strain distribution induces a peculiar ring-like pattern of the PL, as shown in Figure 10b. This pattern is ascribable to relevant strain-induced modifications in the electronic properties of the material, as a consequence of the high strains achieved at the bubbles summit: as predicted theoretically, high tensile strains induce a direct-to-indirect band gap transition, due to a crossover of the valence band K and Γ states.[101–104]

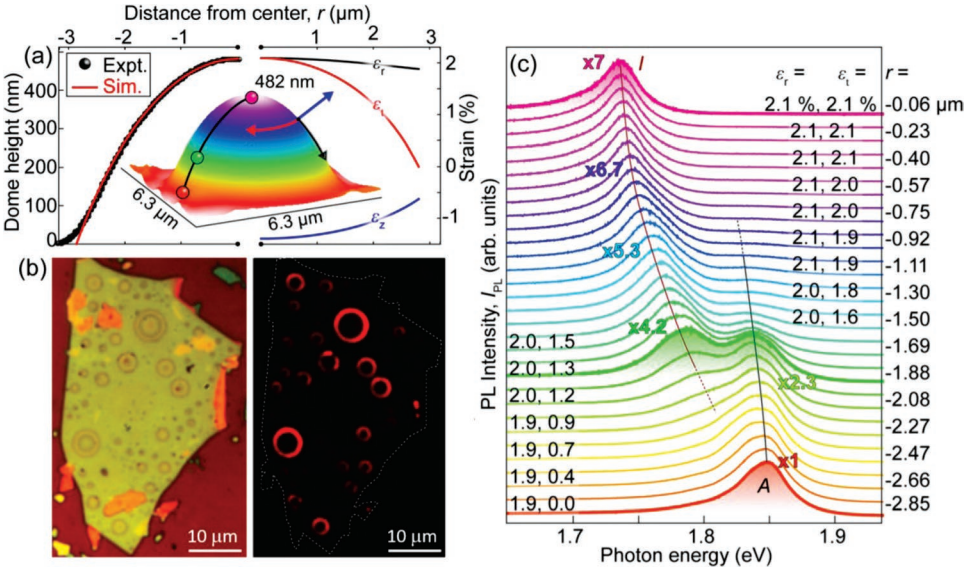

Figure 10. a) Left: Height profile of a WS_2 bubble formed after H irradiation, measured by AFM (black dots; the AFM image is shown as inset), and computed by FEM calculations (solid red line). Right: Dependence along the dome radius of the strain tensor components, represented as color-coded arrows in the inset. The three dots (purple: top; green: intermediate; orange: edge) correspond to the shadowed spectra in (c). b) Left: Optical image of a WS_2 flake, where many relatively large bubbles formed after H irradiation. Right: Laser-excited red luminescence coming from the same flake shown on the left. c) Normalized emission spectra of the bubble as the laser spot is scanned from the left edge (bottom) to its apex (top). Intensity factors are displayed for some selected spectra. Spectra are labeled with the laser spot position and with the values of the radial (ε_r) and circumferential (ε_θ) strain components. The solid lines follow the energy shift of the direct (*A*, black line) and indirect (*I*, red line) exciton transition. Reproduced under the terms of the CC-BY 4.0 license.[9] Copyright 2020, The Authors, published by American Physical Society.

Such a band gap transition was clearly experimentally observed in the bubbles, where the spectra at the edges are dominated by the direct A (or K_{CB}–K_{VB}) exciton, while a new band appears while moving toward the center. This new band, attributable to the indirect *I* (or K_{CB}–Γ_{VB}) exciton, indeed dominates the PL spectrum at the bubble center.[9]

Before discussing the characterization tools used to investigate the elasto-mechanical properties of 2D membranes, we summarize the main features of the methods presented so far for deforming them. **Figure 11** depicts a qualitative assessment of the different characteristics of the methods employed to mechanically deform 2D crystals. At variance with bubbles and wrinkles, indenting methods require rather bulky devices that hampers the possibility to incorporate them into different set-ups and thus their manageability. Indenting and blistering have respectively modest and low (see Figure 5d) durability, while wrinkles and bubbles maintain their shape for very long times (see, e.g., ref. [39] for the bubble case). Very high control in the positioning, as well as in the spatial extent of the strained region, can be achieved by blistering, indenting and bubble formation. The first twos permit also an excellent dynamical tunability, which is instead absent in the case of static bubbles and wrinkles.

2.3. Topological Characterization

The investigation of the peculiar nanoscale landscapes induced in 2D materials by mechanical deformations (wrinkles, blisters, bubbles, ripples), and the study of their topology and implications on the material's band structure, have largely profited from high-resolution metrology tools based on scanning probe microscopies (SPM).[105] Indeed, the "SPM" label identifies a comprehensive family of experimental techniques capable of correlating the sample morphology with the local elasto-mechanical and electronic properties at the nanoscale. The

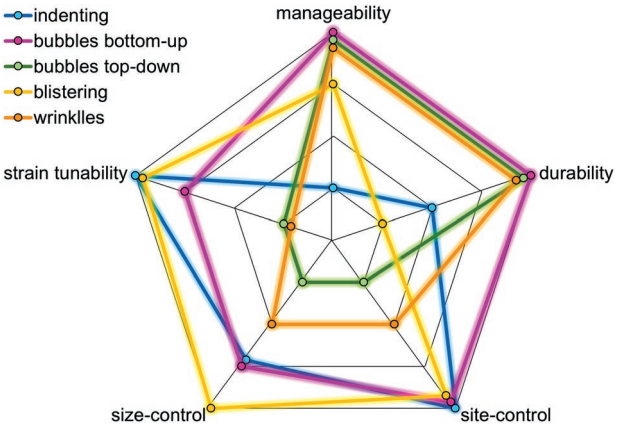

Figure 11. Radar plot showing the main qualitative features (from low to high on going from center to edge) of the different methods described in Sections 2.1 and 2.2. Indenting refers to the approach employing the tip of an AFM as outlined in Figure 1 (and Figure 2). As for the bubbles, the definition of bottom-up and top-down is given in Figure 8. Manageability indicates the ease of inserting the deformed membranes into diverse set-ups. Durability refers to lifetime of the induced deformation status. Site- and size-control indicates, respectively, to which degree the given method allows for inducing strain in a specified location and with a given spatial extension. Finally, strain-tunability indicates the possibility to modify the induced strain.

aim of this section is thus to present an overview of the most significant results and advancements in the nanoscale study of deformed 2D materials, achieved by employing different SPM techniques.

Section 2.3.1 will be devoted to the investigation of the peculiar morphological landscapes occurring in deformed 2D materials, as studied by AFM and AFM-based techniques. We will review some AFM studies of pre-deformed 2D materials, as well as we will discuss some peculiar examples of AFM-induced deformations and manipulation of 2D membranes. Hints on the nanoscale frictional characteristics of strained 2D materials, obtained by lateral force microscopy (LFM), will be finally discussed.

Section 2.3.2 will be focused on the study of the electronic properties of deformed 2D materials, performed by employing a large variety of AFM-based techniques, such as conductive atomic force (C-AFM), piezo-response force microscopy (PFM), electrostatic force (EFM), and Kelvin probe microscopy (KPFM or KFM).

Section 2.3.3 will review the main results obtained by performing scanning tunneling microscopy and spectroscopy (STM/S) experiments on strained 2D materials.

Finally, Section 2.3.4 will discuss innovative strategies for simultaneously inducing and measuring strain in 2D materials, by employing a dual-probe approach. The latter is obtained by combining multiple SPM techniques at the same time (AFM/AFM, AFM/STM), or by integrating an SPM technique with another characterization method (AFM/Raman, AFM/scanning electron microscopy, SEM).

Before detailing some of the most recent results obtained by SPMs on strained 2D materials, we summarize the main features and capabilities of these characterization techniques, in terms of applicability field, technical requirements and limitations (such as the probe type and the best lateral resolution), and provided physical quantities (outputs). **Table 1** is thus introduced to this aim.

2.3.1. Strain-Induced Topographic Landscapes: AFM Studies

As the possibilities to induce strain in atomically thin membranes are many and variegated, the nanoscale topology of the resulting landscapes evolves accordingly. In the following, we will mainly discuss the typical topological strain-induced features arising in 2D materials, either spontaneously, because of the fabrication techniques, or in a controllable manner because of engineered straining methods.

As discussed in Section 2, spontaneously induced local strained areas commonly arise in CVD-grown 2D materials. Indeed, during the CVD post-growth cooling process, the (typically metallic) substrate contracts more than the 2D material, due to their different thermal coefficients, and an overall compressive strain sets up, resulting in wrinkle/buckle formation.[57–62] For instance, **Figure 12**a shows the AFM topography of a wrinkle occurring in CVD-grown graphene on top of a Cu substrate.[106] Importantly, such features are expected to host both compressive and tensile strains, with the former predicted to arise at the bases of the wrinkle, characterized by a concave profile. The tensile strain occurring at the top (convex region), on the other hand, is proportional to $\frac{h_0}{w}$, where h_0 is the height at the wrinkle's summit, and w is its width.[107] The influence of wrinkled topography on the electronic properties of 2D

Table 1. Features and capabilities of the main SPM techniques used in the characterization of strained 2D materials. Each listed technique, and the forthcoming results, will be further discussed in the next sections.

SP microscopy	Acronym	Applicability	Probe	Outputs	Resolution	Mode
Atomic force	AFM	Unlimited	Cantilever-based	Topography, Roughness	>1 nm	Contact
						Tapping
						Non Contact
Friction force	FFM	Unlimited	Cantilever-based	Friction	>1 nm	Contact
Tortional force	TFM	Unlimited	Cantilever-based	Friction	>1 nm	Contact
Conducting force	C-AFM	Conductors, Semiconductors	Cantilever-based, Conducting	Current maps	>1 nm	Contact
				Resistance maps		
				IV characteristics		
Piezoresponse force	PFM	Piezoelectrics	Cantilever-based	Piezo-displacement	>1 nm	Contact
		Ferroelectrics	Conducting	Piezo-coefficients		
Electrostatic force	EFM	Conductors, Semiconductors	Cantilever-based, Conducting	ΔV_{CPD}	>1 nm	Lift
				Work function		
				F vs. *V*		
Kelvin probe force	KPFM	Conductors	Cantilever-based	ΔV_{CPD}	>1 nm	Lift
		Semiconductors	Conducting	Work function		
Scanning tunneling	STM	Conductors, Semiconductors	Wire, Conducting	Topography	<1 nm	Non Contact
				IV characteristics		
				Conductance		
				DOS		

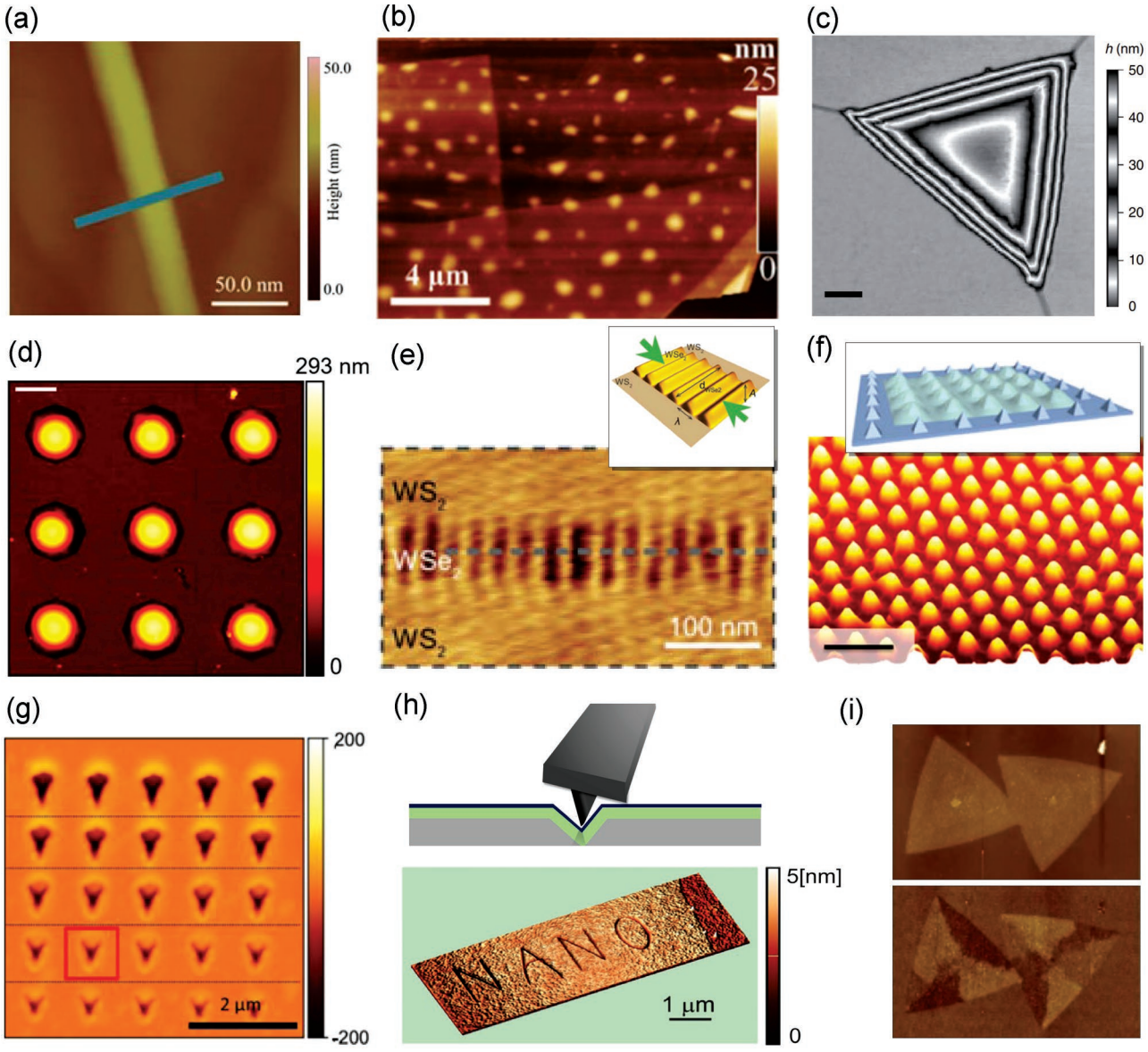

Figure 12. a) AFM morphology of graphene on Cu substrate. Wrinkles appear because of the compressive strain generated by different graphene/Cu thermal coefficient. Reproduced under the terms of the CC-BY 4.0 license.[106] Copyright 2017, The Author(s), published by Springer Nature. a,b) AFM topography of transfer-induced nanoscale bubbles of circular (b) and triangular (c) shape. b) Reproduced with permission.[71] Copyright 2018, American Physical Society. c) Reproduced under the terms of the CC-BY 4.0 license.[38] Copyright 2016, The Authors, published by Springer Nature. d) AFM image of engineered bubbles pattern obtained by plasma treatment. Reproduced with permission.[6] Copyright 2020, Wiley-VCH. e) WS_2-WSe_2 lateral heterostructure showing ripples due to lattice mismatch and compressive strain. Schematic illustration of ripple formation (inset) and AFM map (main). Reproduced with permission.[68] Copyright 2018, American Association for the Advancement of Science. f) Deformation of 2D materials on 3D architectures. Schematic illustration (inset) and AFM map (main). Inset: reproduced with permission.[23] Copyright 2015, American Chemical Society. Main: Reproduced under the terms of the CC-BY 4.0 license.[30] Copyright 2015, The Authors, published by Springer Nature. g) Pattern of local strained areas obtained by modulating the cantilever displacement during indentation. Reproduced with permission.[82] Copyright 2019, American Chemical Society. h) 3D AFM image of structures fabricated by DPL in graphene. Reproduced with permission.[108] Copyright 2013, IOP Publishing Ltd. i) AFM topography (top) and LFM (bottom) images of CVD-grown MoS_2 flakes. Reproduced under the terms of the CC-BY 4.0 license.[109] Copyright 2018, The Authors, published by Springer Nature.

materials, and the invaluable use of SPM techniques for their study, will be further discussed in Sections 2.3.2 and 2.3.3. On the other hand, uncontrollable deformations can take place as a consequence of transferring or mechanically exfoliating the 2D materials on top of a substrate or on stacks of vdW heterostructures. As a consequence of local gas or liquid trapping in the interlayer crystal region, nanometric protrusions of variegated shapes can form in the 2D membrane, thus hosting a local strain.[38,69–72] For instance, Figures 12b and c show the AFM imaging of some spontaneously formed blisters, in the shape of circular and triangular protrusions, respectively, as formed in a graphene layer after transferring.[38,71] In both cases, the strain

of the membrane is dictated by the ratio between its geometrical parameters (maximum height h_0, and radius R or length L) and can thus be estimated from AFM measurements. In particular, spherical blisters or bubbles, as the ones shown in Figures 12b and d, hold an anisotropic tensile in-plane strain that increases from the edge towards the summit, where it becomes isotropic biaxial. The link between the strain distribution and the blister/bubble morphology and, more specifically, its aspect ratio h_0/R, is indeed highlighted in Equations (6), showing how the strain components scale quadratically with h_0/R. AFM imaging, allowing for the measurement of the geometrical parameters of the system with nanometric resolution, is thus an essential tool to probe strain in these systems. Noticeably, AFM measurements have also been used to highlight how bubbles of the same material are always characterized by the same aspect ratio h_0/R, and in turn by an analogous strain distribution, independently of the fabrication method. Such a saturation of the aspect ratio to its so-called universal value is indeed linked to the energy minimization conditions,[38,72] and its value ranges from ≈0.1 in hBN[38,72,94] to almost ≈0.2 for monolayer $MoSe_2$.[39,72]

However, as discussed in Section 2.2.3, micro- and nanoscale localized protrusions, such as bubbles and blisters, can be also created ad-hoc in 2D materials, with different fabrication methods.[39,94] In this respect, external constraints have been additionally exploited to manipulate the system in a controlled manner and eventually overcome the strain limitation imposed by the universal value in free systems. Blundo et al.[6] demonstrated that the bubble aspect ratio, and thus its strain, can be modified by engineering ad-hoc the flake surface prior to H irradiation, by realizing a selective coating with a hydrogen opaque mask. The mask can be designed with quasi-circular holes of the desired dimension (diameter from ≈50 nm to several microns) by electron beam lithography.[6,39] With this approach, the H ions penetrate only in the openings with a consequent bubble formation occurring selectively in the uncoated locations. Bubble patterns of the desired period and size can be thus created, with a consequent full control of the strain location.[5,6,39] If the mask is thick enough, it acts as an external constraint, so that the aspect ratio of the bubbles increases, allowing one to reach strains as high as 12%.[5,6] Figure 12d shows the AFM map of a regular square array of bubbles, with $h_0 \approx 300$ nm and a diameter $D \approx 3$ µm, protruding from the mask-coated surface of a MoS_2 bulk flake, produced with this approach. By playing with the opening diameter, the aspect ratio of the MoS_2 bubbles could be tuned from ≈0.16 (universal value) up to ≈0.3, by reducing the opening size.[6]

As mentioned at the beginning of Section 2, the epitaxial growth of lateral 2D heterostructures has been also explored as a possibility to transfer a controllable amount of strain into the 2D crystals.[63–68] For instance, the bottom panel of Figure 12e shows an AFM image acquired on a lateral heterojunction made by alternating WS_2 and WSe_2 monolayers in the same growth plane,[68] and focusing on a $WS_2/WSe_2/WS_2$ portion of the superlattice. As schematically illustrated in the top panel, WSe_2 hosts the formation of out-of-plane ripples, occurring as a consequence of a compressive strain. These features ran continuously across the WSe_2 stripes, and were shown to be periodic along the heterointerfaces. The superlattice is indeed affected by a tensile (compressive) strain within each WS_2 (WSe_2) region, with direct consequences on the band structure of both materials: the size of the direct band gap decreased (increased) when subjected to tensile (compressive) strain. The magnitude of such strains further exhibited a dependence on the supercell dimension. More recently, in-plane heterostructures were also shown to hold the potential to host the growth of ultralong nano-channels, and ultimately quantum well structures.[110,111] Strain-driven growth mechanisms, controlled by grain boundaries or misfit dislocations, were employed to this aim.

On the other hand, the bottom panel of Figure 12f shows an example of a 3D AFM image of a periodically strained MoS_2 monolayer, obtained by transferring the 2D material on top of a nanostructured substrate. Here, in particular, MoS_2 was transferred on top of SiO_2 nanocone structures,[30] schematically depicted in the top panel.[23] Due to the tendency of 2D materials to adhere to the underlying substrate, the MoS_2 layer conformed to the SiO_2 nanocones, acquiring a non-zero curvature. As a result, and as verified by PL/Raman and STM analysis, the 2D layers resulted successfully affected by a local substrate-driven tensile strain.

The patterning of controlled nanometer-scale strain profiles in 2D materials has also been successfully achieved by AFM manipulation and lithography. These latter techniques, indeed, allow one to encode locally strained areas with nanometric precision, upon the application of a sufficient indentation or interaction force between the AFM probe and the 2D material. In the past, AFM lithography based on indentation and dragging was introduced for precise in-plane cleavage of 2D sheets,[112] resulting in the ability to define graphene nano-constrictions down to 10 nm in width. On the other hand, Rosenberger et al.[82] explored the effect of the local indentation on a 2D layer deposited on top of a deformable substrate. They demonstrated that, if the applied force is sufficient to imprint plastic deformations into the substrate, the 2D membrane will follow the as-produced underlying, deformed profile, thus gaining a local strain. Figure 12g shows a representative AFM map acquired on WSe_2 on top of a substrate made of a topmost, soft layer of poly(methyl methacrylate) (PMMA), 300 nm thick, deposited on SiO_2/Si. Locally deformed areas appear on the WSe_2 surface after performing a grid of AFM indentations, with a blunt tip. Different topographic depths are produced by modulating the maximum cantilever displacement (proportional to the maximum indentation force) from 1000 (lower line) to 2000 nm (upper line). A schematic image of this procedure is shown in the top panel of Figure 12h. Similar results were obtained by indenting on graphene on top of SiO_2/Si.[113] Since the SiO_2 substrate undergoes a plastic deformation before the insurgence of damage in the graphene sheet, a pattern of dots and lines could be obtained by AFM indentation (dots) or by indentation and dragging (lines), wherein graphene was locally strained to follow the substrate deformation. A different AFM-based manipulation technique, the so-called dynamic plowing lithography (DPL), was, instead, developed by Vasic et al.[114] In this case, the cantilever is in alternate contact with the surface, which guarantees a torsion-free interaction, with negligible lateral dragging. By locally modulating the amplitude setpoint to a value 10–100 times smaller than the ordinary scanning (stronger interaction), they were able to imprint different shape patterning (lines, circles, and words) in graphene. The bottom

panel of Figure 12h shows the AFM map acquired after using DPL to pattern the world "NANO" in a graphene layer deposited on top of SiO_2/Si. In conclusion, these results present a general methodology for imparting strain into 2D materials, with nanometer-scale precision, and prove that the AFM is an invaluable tool for on-demand deformation along arbitrarily shaped patterns, also known as quantum calligraphy, with excellent control and repeatability.

Finally, AFM-based LFM, such as friction and torsion force microscopy (FFM and TFM, respectively) have been shown to hold the potential to study the characteristics of locally strained areas in 2D materials, such as atomic-scale, smoothly-varying ripples and periodic deformations, through the measurement of the local friction.[115–118] Differently from conventional AFM, LFM techniques are based on the measurements of the longitudinal, rather than normal, tip-sample interaction force, with the scanning direction parallel to the cantilever in TFM, and perpendicular in FFM. Anisotropic friction domains in exfoliated graphene,[119–121] hBN[121] and MoS_2[122] as well as in CVD-grown MoS_2[109] have been observed by LFM and attributed to either sub-nanoscale ripples (not accessible by AFM topography), or self-assembly of environmental adsorbates on the 2D material surface. A common strategy to discriminate between the two relies on performing an annealing treatment. This procedure is indeed known to be capable of releasing the internal material stress, ultimately resulting in a single-friction domain in the post-annealing imaging. On the contrary, the surface adsorption is expected to be a reversible process, with the absorbates being released during the heating-up phase and re-adsorbed in the post-annealing one, thus still giving rise to anisotropic friction domains. The top panel of Figure 12i shows the AFM image of two MoS_2 monolayers grown by CVD on a Si/SiO_2 substrate. While no grain boundaries or topographic defects are clearly observable in their morphology, the TFM image reported in the bottom panel of Figure 12i displays three distinct friction domains. By comparing the results of sample-rotation angle-dependent TFM imaging and second harmonic generation, Lee et al.[109] were able to demonstrate that such anisotropic friction domains come from linearly aligned strain-induced ripple structures, with aspect ratios far beyond the AFM resolution, aligned along the armchair direction of the crystal lattice. It is indeed expected that the friction anisotropy originates from very smooth ripples with $h/w \leq 1/10$, where the height is $h \sim$ Å and the width is $w \sim$ nm. The interaction of the 2D layer with the substrate is thus considered a possible source of the observed local strain field distribution and resultant ripple structures. Noteworthy, TFM imaging performed after annealing at 350 °C disclosed a uniform friction contrast.

2.3.2. Strain-Induced Variations in Nanoscale Electrical Properties: AFM-Based Studies

AFM-based electrical modes allow for the simultaneous measurement of sample topography and electrical properties, with the incomparable advantage of profiting of nm-scale spatial resolution. Their operation makes use of metallic or metal-coated probes and relies on the application of additional DC and/or AC voltage between the tip and the sample.

In the so-called Conducting-AFM (C-AFM), a DC bias is applied to the tip with the sample grounded (or vice versa) (an exemplary C-AFM schematic is shown as inset in **Figure 13**b). The resulting current I flowing through the nm-sized contact between the probe and the surface can be measured: i) as a function of voltage V, in a fixed location (spectroscopy mode), thus allowing for the acquisition of local I–V curves; ii) as a function of location, at a fixed voltage (microscopy mode), resulting in current (or resistance) maps of the sample surface. In the past, C-AFM has been successfully used to obtain a spatial mapping of the conductivity of graphene on different substrates,[123–125] as well as to measure the Schottky barrier height of epitaxial graphene grown on H-SiC.[126] The effect of the density and energy of surface states on the Schottky barrier at the MoS_2 surface has been also investigated by C-AFM.[127] Notably, Maiti et al.[128] used C-AFM to investigate the local conductivity of a few-layer 2H-$MoTe_2$, integrated on top of a photonic waveguide (step-like ridge structure). Figure 13a shows the 3D AFM topography of the device, with the 2D material conforming to the underneath structure, with a consequent buildup of tensile strain. By performing C-AFM spectroscopic measurements, they collected a series of I–V curves (Figure 13b) in different locations, numbered from 1 to 9, across the strained area. The latter suggested a graded modulation of conductivity across the waveguide, with a maximum near its edge. The authors ascribed this behavior to two possible effects, namely, the reduction of the semiconducting bandgap and the modulation of the Schottky barrier. Given the small bias range considered (subthreshold regime)—with transport dominated by thermally excited carriers—and the shape of the measured curves—symmetric and linear – the authors suggested that the measured electrical transport is mostly dominated by the reduction of the bandgap.[129,130] The comparison of the experimental results with the theoretical expectation suggested the presence of a 2–3% local strain in the $MoTe_2$ region overlaid to the waveguide.

As many 2D materials exhibit strong piezoelectric response,[131–133] piezo-response force microscopy (PFM) has also been shown to hold great potential for their investigation. In this case, an AC voltage is applied, in contact mode, between the tip and the sample. The resulting piezoelectric vibrations of the material are thus recorded, as a function of position, through the local deformation of the AFM cantilever. Recently, PFM was used to investigate novel phenomena occurring in 2D heterostructures. For instance, Bai et al.[134] employed this technique to study the Moiré pattern coming from the lattice twist angle mismatch of a $WSe_2/MoSe_2$ heterobilayer structure. The PFM map (top panel of Figure 13c) and the corresponding FFT (inset) reveal a six-fold symmetry, with a periodicity proportional to the mismatch angle between the layers inside the stack. Additionally, by repeating the measurements in the same topographic locations after transferring the stack on top of a Si/SiO_2 substrate, they found that, in some cases, the Moiré pattern transformed into a distorted 1D Moiré superlattice (bottom panel of Figure 13c), with the FFT clearly displaying a two-fold symmetry (inset). Such a modified symmetry is consistent with the presence of uniaxial and differential strain, which seemed to affect 80% of the investigated sample locations after transferring.

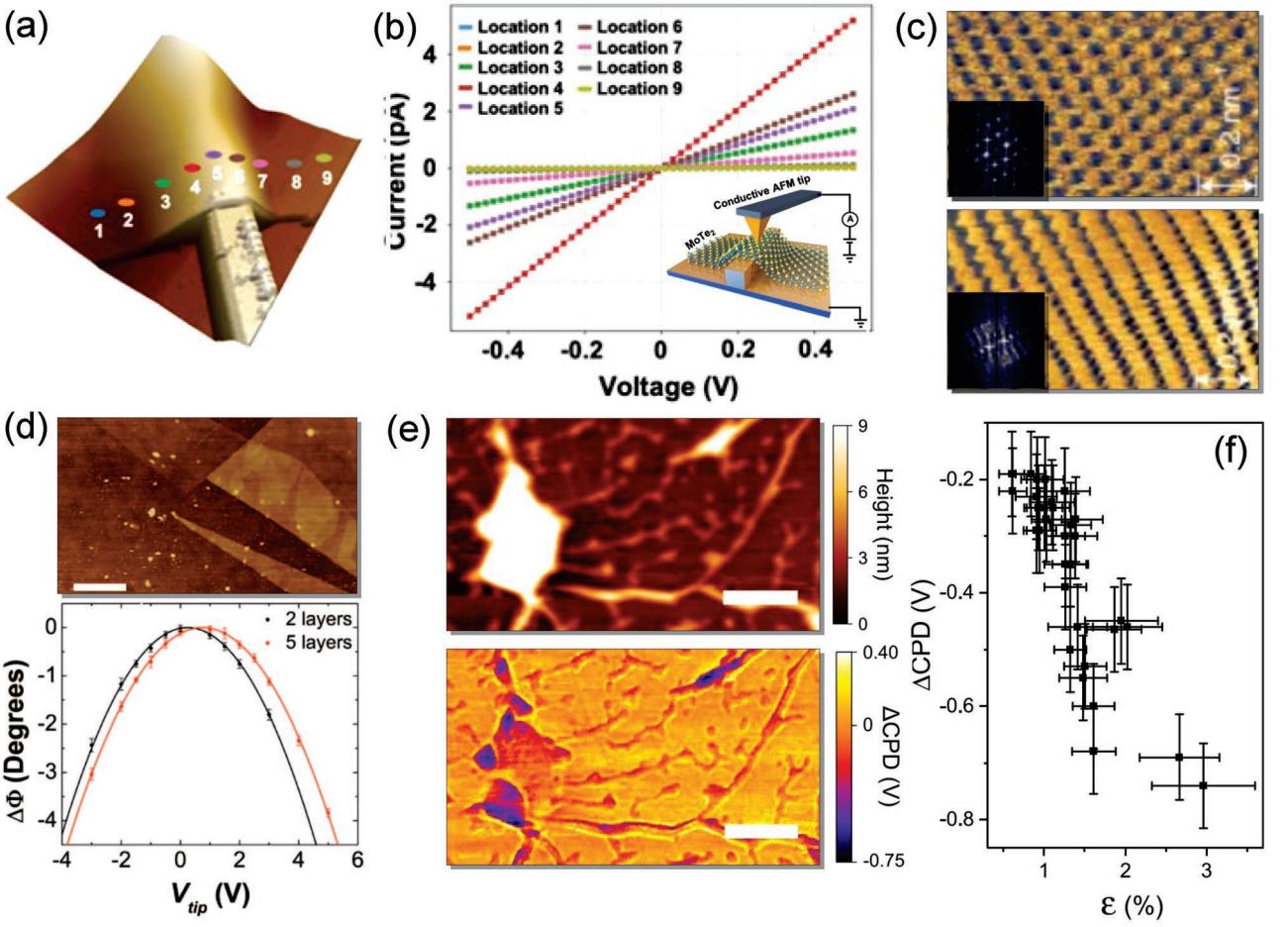

Figure 13. a) 3D AFM topography of a few-layer thick $MoTe_2$ flake on top of a photonic waveguide. b) Main: *IV* curves measured at the different location across the strained area, as numbered in (a). Inset: schematic of C-AFM. a,b) Reproduced with permission.[128] Copyright 2021, American Chemical Society. c) evolution from 2D (top) to 1D-like (bottom) Moiré pattern in $WSe_2/MoSe_2$ heterobilayers measured by PFM. Insets: corresponding FFTs. Reproduced with permission.[134] Copyright 2020, published by Springer Nature. d) Top: AFM topography of few-layer graphene. Bottom: EFM spectroscopy measured on 2 and 5 layer graphene. Reproduced with permission.[135] Copyright 2009, American Chemical Society. e) Top: AFM topography of a wrinkled $MoSe_2/WSe_2$ heterostructure. Bottom: corresponding KPFM image. f) KPFM-measured contact potential difference vs. strain. e,f) Reproduced with permission.[136] Copyright 2020, American Chemical Society

Other effects, such as the strain-induced modifications of the work function, or the charge exchange between a 2D layer and its substrate (or between the different stacks of a 2D heterostructure) can be studied, at the surface, by using electrostatic force microscopy (EFM). This mode relies on the quadratic electrostatic interaction between an AFM probe and the sample, 20–100 nm away from one another, as a consequence of the application of a DC voltage:

$$F_{el} \propto (V - \Delta V_{CPD})^2 \tag{8}$$

where F_{el} is the electrostatic interaction force and $\Delta V_{CPD} = \frac{W_{tip} - W_{sample}}{e}$ is the so-called contact potential difference, or surface potential, with W_{tip} and W_{sample} being the tip and sample work functions, respectively. At the maximum of the parabola, when the external bias matches ΔV_{CPD}, F_{el} is nullified, thus allowing for a differential measurement of W_{sample}. The setting-up of the electrostatic force, and its variation as a function of the bias, can be detected as a pure deflection of the cantilever toward the sample, in static mode, or as a variation of the frequency or phase of the oscillating cantilever, in dynamic mode. Figure 13d shows some EFM measurements acquired on a few-layer graphene flake on top of Si/SiO_2. The AFM topography is reported on top, while the bottom panel shows the quadratic variation of the oscillating cantilever's phase as a function of *V*, for two- and five-layer graphene, with the maximum of the parabola being at higher (positive) voltage in thicker areas. Based on these results, Datta et al.[135] demonstrated that the surface potential of graphene increases strongly (over hundreds of meV) and monotonically with increasing the film thickness. They correlate this variation to the charges transferred to the graphene flake from a thin (<1 nm) interfacial layer of charged traps or defects at the silica surface.

Similar information can be derived by performing the so-called Kelvin probe force microscopy (KPFM or KFM). In this case, the local variations of the maximum of the F_{el} parabola are mapped as a function of location, while scanning the tip on top of the sample surface. A ΔV_{CPD} imaging, to be ultimately

converted into W_{sample} maps, can thus be obtained. Figure 13e shows the AFM morphology (top) and the ΔV_{CPD} map (bottom) of a wrinkled $MoSe_2/WSe_2$ heterostructure. A clear correspondence exists between the topography and the surface potential maps, with the strained areas manifesting a lower ΔV_{CPD} (higher work function). Finally, Figure 13f plots the measured ΔV_{CPD} as a function of the tensile strain ε estimated from the wrinkled topography. The two parameters show a clear correlation, with higher values of tensile strain leading to stronger negative ΔV_{CPD}, providing evidence of the strain-induced surface potential variation.

2.3.3. Strain-Induced Variations in Nanoscale Electrical Properties: STM/S Studies

The STM/S study of 2D materials has been extremely valuable in demonstrating the correlation between electronic properties and number of layers, atomic structure, defects, and grain boundaries. Indeed, besides allowing for the high-resolution mapping of the sample surface, down to the sub-atomic level, the STS acquisition of local $\frac{dI}{dV}$, or conductance spectra, allows for a direct investigation of the material's density of states. In 2D materials, the latter is profoundly affected by mechanical deformations and strains. Compared to other techniques, the advantage of STM relies on the possibility of measuring the conductance and the atomic-resolved topography in the same spot, thus being able to correlate changes in the density of states to the true microscopic atomic lattice strain. Trainer et al.[137] have indeed demonstrated that the local microscopic strain may differ substantially from what would be expected based on the external, 'macroscopic' stress, applied to the sample as a whole. For instance, **Figure 14**a shows modulations of the MoS_2 bandgap from 2.2 to 1.2 eV, when increasing the local, measured strain from 0.2 to 3.1%. It is interesting to note that such strain values, computed by imaging the microscopic distortion of the atomic lattice, are quite different from the ones expected at the macroscopic level, ranging from 0 to 4.9%, and resulting from the geometry of the employed straining device. The partial strain relaxation can be ascribed to the nanoscale formation of wrinkles and ripples, as the ones imaged in the top panel of Figure 14b, acting as local stress-release sites. Here, STM topography (top) and conductance map at –1.72 eV (bottom) display a clear one-to-one correspondence, with the inner-ripples region (affected by higher tensile strain), disclosing an increase of conductance states. Energy gap tunability, as a function of strain, was also recently demonstrated by STM/S in the semi-metal 1T'-WTe_2, in the monolayer limit.[138] Due to the growth conditions, the islands of 1T'-WTe_2 resulted affected by a tensile strain, with higher value for islands with smaller size. A representative STM topography of one of these islands is reported in the top panel of Figure 14c. From the atomic resolution of the crystal lattice, the authors were able to evaluate a tensile strain of 3.4% and 5% along the [100] and [010] crystal directions, respectively. The bottom panel of Figure 14c shows the variation of the WTe_2 bandgap, measured by STS, as a function of the island surface area, thus demonstrating that the bandgap decreases when increasing the island size (reducing the strain). This result corroborates the theoretical calculations[139] predicting a monotonic increase of the WTe_2 monolayer bandgap with strain.

On the other hand, strain is naturally introduced in 2D van der Waals (vdW) heterostructures,[140] as the layers inside the stack try to match their atomic lattices to reach the lowest energy stacking arrangement.[141] Figure 14d shows STM topographies of a MoS_2/WSe_2 heterobilayer. While the Moiré pattern coming from the lattice mismatch is clearly visible in the top panel, atomic-resolved images are reported on the bottom, respectively in the blue, red, and green areas. The different Moiré contrast in each of these regions is due to a different arrangement of atoms between the top and bottom layer. The spatial locations where the Mo atoms are directly on top of the W atoms—denoted as *AA* stacking), in blue—correspond to the Moiré corrugation maxima. The locations where the chalcogen (metal) atoms of the top layer are on top of the (metal) chalcogen atoms of the other layer—denoted as AB_W (AB_{Se}), in red (green)—correspond to the two types of corrugation minima. The height profile along the three locations (more specifically, along the dashed line in the top part of panel (d)) is reported on the top panel of Figure 14e. From the atomic lattice imaging, the authors were able to quantify the local strain at each location, as reported in the bottom plot of Figure 14e. Here, the gray dashed line indicates the strain ideally occurring in MoS_2 when both layers deform toward the average value of their lattice constants. This strain value is matched at the AB_{Se} locations, where the corrugation is the lowest, and thus, the layers are presumably closest together and a relatively large tensile strain occurs in MoS_2. At the *AA* locations, where the layers are furthest apart, the MoS_2 appears to be compressively strained, compensating for the deformation at the AB_{Se} locations by relaxing past its nominal lattice constant. Finally, a compressive strain is measured at the AB_W locations, rather than the DFT-predicted tensile one. In this case, a STM-tip distortion effect is claimed by the author to explain the behavior.[140]

In conclusion, the STM/S study of 2D materials and their heterostructures reveals the high potential of this technique both in the investigation and computation of the local microscopic strain, and in its correlation with the local electronic properties.

2.3.4. Strain Characterization: Dual-Probe Approaches

Recent developments in the characterization of strains and mechanical deformations in 2D materials involve the integration of multiple probes within the same device. The so-called dual-probe approach combines a SPM with another characterization technique, in order to have a full control of the local deformations and/or mechanical manipulations induced by one of the two probes on the 2D membrane. Examples of dual-probe approaches include coupled STM/STM,[142] AFM/STM,[143] AFM/Raman[144] and AFM/SEM.[145] For instance, Eder et al.[142] reported on the measurement of the deformations induced by one STM probe on a free-standing graphene membrane, by using a second, independent STM probe placed at the opposite side of the layer, in the same spot as the first one, as schematically shown by the top panel of **Figure 15**a. After identifying the tunneling conditions for manipulating the membrane with the first probe, the second STM tip was

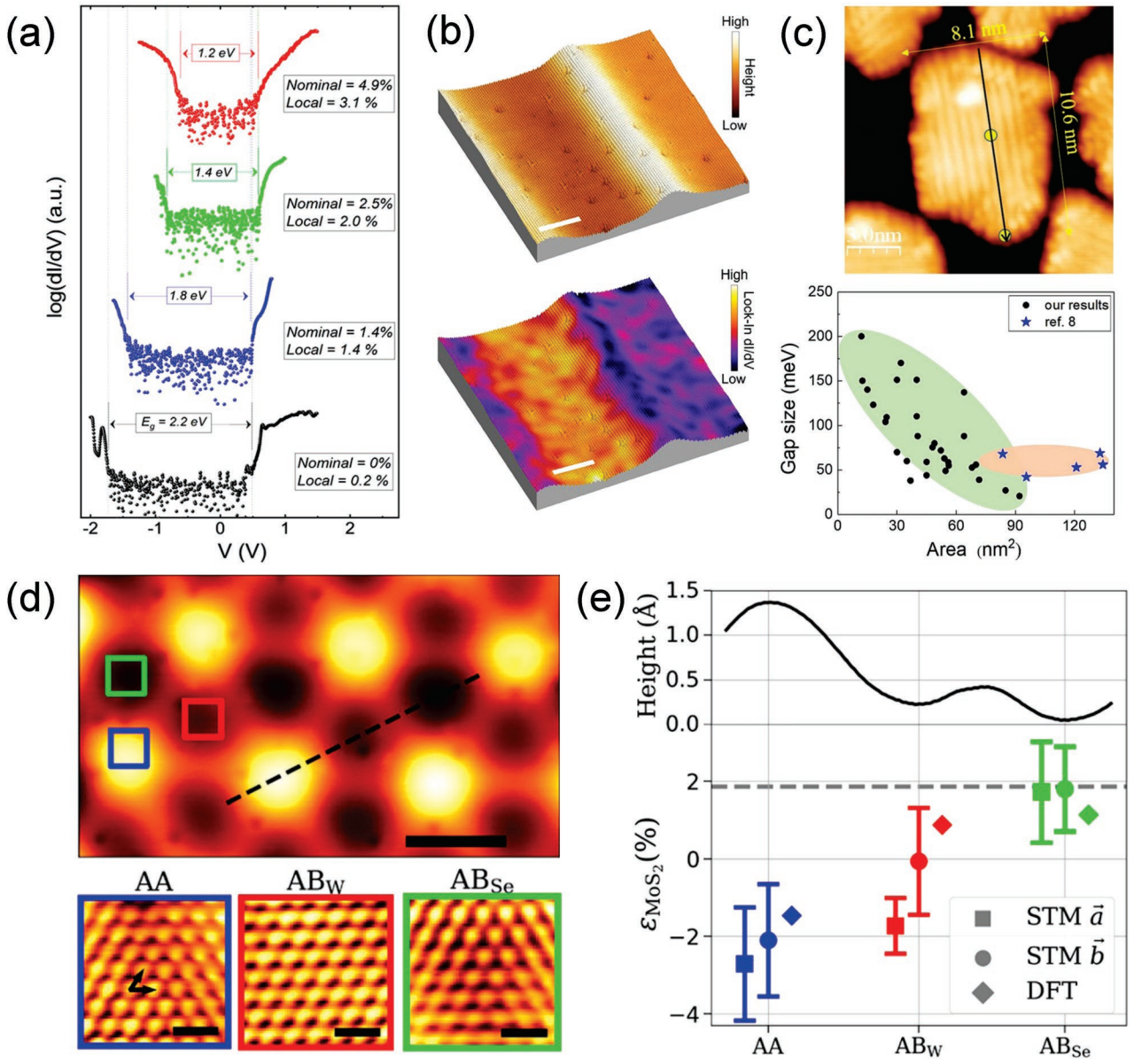

Figure 14. a) STS of MoS_2 as a function of the applied strain. b) Top: STM topography of ripples in MoS_2. Bottom: corresponding zero-bias conductance map. Scale bar is 5 nm. a,b) Reproduced with permission.[137] Copyright 2019, American Chemical Society. c) Top: STM topography of WTe_2 island. Bottom: variation of the bandgap size as a function of the island's area. Reproduced with permission.[138] Copyright 2020, AIP Publishing. d) Top: STM topography of a MoS_2/WSe_2 heterobilayer. Moiré pattern is clearly visible. Scale bar is 5 nm. Bottom: atomic resolution images of the blue, red and green selected areas. Scale bar is 0.5 nm. e) Height and strain variation across the *AA*, AB_w and AB_{Se} position. d,e) Reproduced with permission.[140] Copyright 2020, American Chemical Society.

used to monitor the induced change in morphology. The bottom panel of Figure 15a shows a sequence of images, recorded on one side of the membrane, showing the transformation of a mountain (left) into a valley (right), by gradually pulling the probe on the other side away from the membrane, while maintaining the attraction. In this way, the authors demonstrated to have an accurate control of the local curvature and of the resulting height of the membrane, which leads to new possibilities toward the ad-hoc deformation engineering of 2D materials. A similar concept was developed by Elibol et al.,[143] interfacing AFM and STM probes on opposite sides of a few-layer graphene membrane. A schematic illustration of the setup is reported in the top panel of Figure 15b. They demonstrated novel imaging modes where the local strain induced from one, stationary or scanning, (AFM or STM) probe is investigated by the other scanning (STM or AFM) tip. The bottom images of Figure 15b show, for example, a sequence of tapping mode AFM topographies, obtained with the STM tip approached on the opposite side of the membrane and gradually moving along the *y*-direction. Notably, they also developed the so-called electrical cross-talking imaging (ECT), which allows for recording a current between either tips and

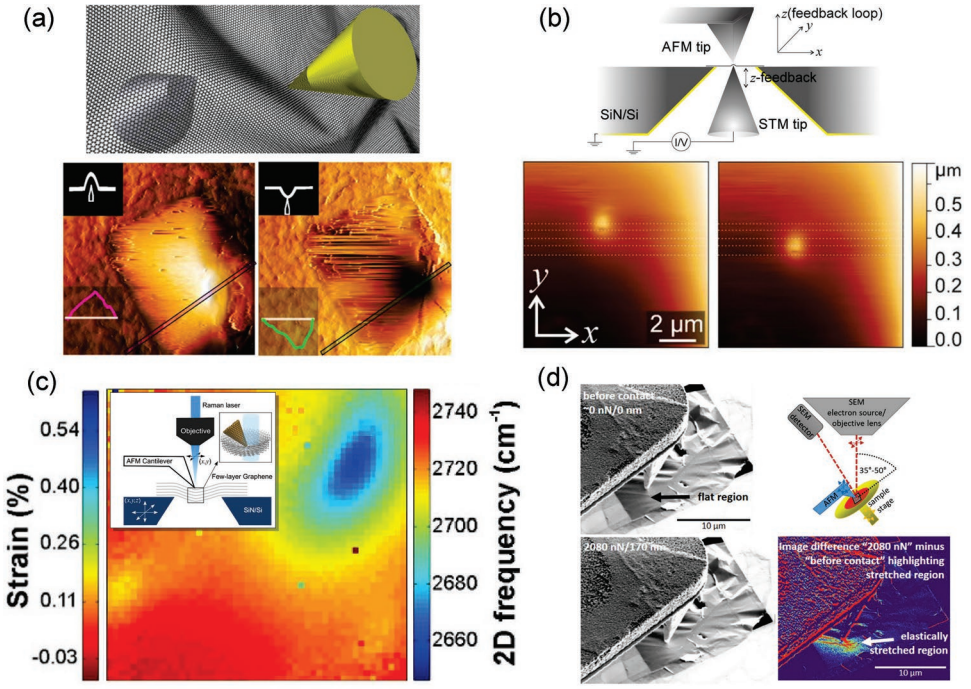

Figure 15. a) Top: Schematic illustration of douple STM probes, coupled through the opposite side of a 2D membrane. Bottom: STM image of a few-layer-thick graphene membrane deformed in mountain- (left) and valley-shape (right) by a second STM tip underneath. Reproduced with permission.[142] Copyright 2013, American Chemical Society. b) Top: Schematic illustration of AFM/STM coupled device. Bottom: AFM images of the top-most surface of a few-layer graphene membrane deformed by an underneath STM tip. Reproduced under the terms of the CC-BY 4.0 license.[143] Copyright 2020, The Authors, published by Springer Nature. c) Main: Raman map of 2D band frequency in few-layer graphene, locally loaded by AFM nanoindentation. Inset: schematic of AFM/Raman coupling. Reproduced under the terms of the CC-BY 4.0 license.[144] Copyright 2016, The Authors, published by Springer Nature. d) Left: SEM micrographs of an unloaded (top) and AFM-loaded (bottom) few-layer graphene membrane. Right: schematic of AFM/SEM coupling (top) and image difference calculated between 2080 nN-loading and before AFM contact images. Reproduced under the terms of the CC-BY 4.0 license.[145] Copyright 2021, The Authors, published by AIP Publishing.

the sample, as a function of i) the position of the scanning tip and ii) the deformation induced by the opposite probe. By doing so, they demonstrated that the surface area affected by higher conductance monotonically expands as the superimposed deformation increases. Interestingly, Elibol et al.[144] also demonstrated a successful example of AFM/Raman coupling to study the deformation induced by the AFM tip into a few-layer graphene membrane (schematic illustration as inset of Figure 15c). They estimated the local strain distribution under and adjacent to the AFM tip via the strain-dependent frequency shifts of the few-layer graphene G and 2D Raman bands, through AFM-based nanoindentation and simultaneous Raman mapping. During the lateral scanning of the Raman laser spot, the AFM tip was kept on a fixed spot on the surface of the suspended few-layer graphene and, upon the application of a highly localized force from the AFM tip, the authors showed the evolution of the G and 2D peak positions toward lower frequencies. Figure 15c shows an exemplary map of the local variations of the 2D Raman band across a sampled area including indented free-standing graphene and SiN/Si supported graphene. A highly localized region of downshifted frequencies, representative of tensile strain, shows up around the indentation point, and increases both in size and maximum downshift as the indentation force increases, up to a spatial extent of ≈7 μm in diameter for an indentation force of ≈6300 nN (Figure 15c). Based on geometrical considerations on the tip size and shape, the authors estimated a contact area between the AFM tip and the membrane of ≈1 μm maximum, thus proving that the strain field from a nanosized SPM probe significantly extends beyond the tip-membrane contact area. Finally, Figure 15d displays an interesting SEM study of AFM-induced deformations in few-layer graphene (schematic on the top-right corner), performed by the same authors.[145] They acquired several SEM micrographs while indenting on the graphene membrane, focusing on the tip apex region. The left column of Figure 15d shows subsequent SEM images obtained before contact (top) and while applying an AFM indentation force of 2080 nN (bottom). By calculating the difference between the 0 nN (before contact) and the full-load images, they estimated that the AFM indentation caused a stretched region in the flat membrane with a lateral extension of ≈6 μm (false color plot of Figure 15d bottom-right). Such a result reasonably agrees with the one obtained by combining AFM and Raman, and demonstrates the capability of coupled, in situ, AFM/SEM to directly visualize, at high resolution, the local deformations induced by AFM-tip loads, with nN control, on the 2D membranes.

In principle, any mode of operation of any scanning probe instrument may conceivably be combined with each other in a similar dual-probe setup, thus opening a large number of new routes for exploring the physics and material properties of ultrathin membranes.

3. Elasto-Mechanical Properties of Two-Dimensional Systems

The outstanding mechanical performances of 2D materials make them appealing for the emerging fields of flextronics and straintronics. However, their manufacturing and integration in 2D crystal-based devices rely on a thorough knowledge of their mechanical properties. Generally, 2D materials can be deformed by in-plane stretching or by out-of-plane bending, thus requiring the introduction of both in-plane and bending moduli for an exhaustive description of their elasticity. In the framework of very thin plates under large deformations,[146,147] Föppl and von-Kármán wrote a system of coupled, non-linear, partial differential equations, establishing the relation between the following quantities: deflection of the plate, stress σ, stretching modulus or Young's modulus of the material *Y*, geometrical dimensions of the plate (lateral size *L* and thickness *t*), applied load, and bending modulus or flexural rigidity $F = \frac{Yt^3}{12(1-\nu^2)}$ (here ν is the Poisson's ratio of the material). It is worth noticing that in the so-called membrane limit, the thickness *t* approaches zero, thus justifying a negligible bending stiffness.[99] The negligibility condition is formally set by the value of the von-Kármán factor (νKf) which weights the contribution of the flexural to the in-plane deformation as $\nu Kf = \frac{E_{2D}L^2}{F}$, ultimately related to the ratio $\frac{L^2}{t^2}$, obtained by introducing the so-called 2D Young's modulus $E_{2D} = Yt$.[148] The thinner the plates, the larger the value of νKf, and thus the weaker the bending/flexural contribution to the deformation. The effect of the bending modulus may thus become substantial only in the case of a multilayer structure: increasing the number of layers would indeed cause a transition from the membrane-like to the linear plate-like behavior.[100,149,150] The elasticity of single layers of 2D materials is thus often characterized by limiting the discussion exclusively to the stretching modulus E_{2D} (or to Y).

Relatively recent theoretical and experimental studies on the mechanical properties of 2D materials have largely pointed out a clear dependence of their elasticity on the extent of the applied load. For instance, first-principle calculations have predicted graphene to exhibit a linear (nonlinear), anisotropic behavior of its stress-strain (σ–ε) diagram when subjected to very small (large) deformation, with the threshold being predicted at a $\varepsilon \sim 5\%$.[151–153] On the other hand, most 2D materials exhibit a linear, isotropic elastic response to small deformations, with the tendency to exert a reduced stiffness for large tensile strains.[154,155] Under moderate to large deformations (lower than the fracture point occurring at the intrinsic stress σ_{int}), continuum thin shell theory establishes the following constitutive relationship:

$$\sigma = E_{2D}\varepsilon + D\varepsilon^2 \tag{9}$$

where the coefficient *D* of the second-order term is expected to be negative, thus reproducing the tendency to exhibit a reduced stiffness with increasing the tensile strain. The intrinsic strength and associated strain are thus defined as:

$$\sigma_{int} = -\frac{E_{2D}^2}{4D} \tag{10}$$

$$\varepsilon_{int} = -\frac{E_{2D}}{2D} \tag{11}$$

Since their intrinsic nanoscale thickness limits the number of approaches capable of measuring the mechanical properties of 2D materials, we will focus our attention mostly on the results of AFM nanoindentation studies. In such tests, the nanometer-sized indenter, the AFM probe, is moved with the typical AFM lateral resolution (≈nm) on selected areas of interest. Local nanoindentation is thus performed by loading the 2D membrane with a controlled force (with sub-nN resolution). The membrane displacement, due to the applied load, is measured simultaneously. The so-called loading force vs. distance curves (FDCs) are then recorded, exploiting the elastic response of the membrane in a σ–ε-like diagram, with the strain being proportional to the membrane displacement caused by the applied load (stress). Finally, the material's mechanical properties are extracted by fitting the measured FDCs to a suitable analytical model.

In this framework, Section 3.1 will review the advancements in the investigation of the elasticity of suspended membranes, both in the doubly-clamped beam and circular thin plate configurations, where no additional, external strain is supposed to play a role, except for the intrinsic membrane pre-strain and for the nanoindentation-induced one. Section 3.2 will be devoted to the elasticity characterization strategies of pre-strained, bulged 2D membranes, in the shape of micro-domes. Finally, we will discuss the elasticity-related wrinkle configuration of 2D materials, in Section 3.3.

3.1. Nano-Indentation of Suspended Membranes

Upon mechanical modeling—typically taking as a starting point Landau's theory of elasticity and the Föppl–von-Kármán equations[146,156]—the relation between loading force *F* and membrane displacement δ_{mem} (see definition in Figure 1) in nanoindentation experiments features linear ($F = A\delta_{mem}$) and cubic ($F = B\delta_{mem}^3$) terms, both in the case of doubly-clamped beams and clamped circular thin plates, subjected to a point force at their center (as previously mentioned in Equation (1)). The coefficients *A* and *B* can be expressed in terms of the relevant geometrical and physical quantities of the system, and they provide information on (i) the Young's modulus *Y* of the material; (ii) the pre-tension (*T*) of the membrane.

The explicit force-displacement relations for circular suspended and doubly-clamped membranes are thus given by Equations (12)[149] and (13),[78] respectively:

$$\text{Circular drum}: \; F(\delta_{mem}) = \left[\frac{4\pi Yt}{3(1-\nu^2)}\left(\frac{t}{R}\right)^2 + \pi T\right]\delta_{mem} + \frac{q^3 Yt}{R^2}\delta_{mem}^3 \tag{12}$$

$$\text{Beam}: \; F(\delta_{mem}) = \left[\frac{\pi^4 wYt^3}{6L^3} + \frac{T}{L}\right]\delta_{mem} + \frac{\pi^4 wYt}{8L^3}\delta_{mem}^3 \tag{13}$$

where *R* is the radius of the hole, *q* is a constant depending on the Poisson's ratio as $q = 1/(1.04912 - 0.14622\nu - 0.15827\nu^2)$,[157] *w* and *L* are the width and length of the suspended part of the stripe, *t* is the membrane thickness. It is worth noticing that Equation (13) has also been used for suspended nanoribbons.[158]

In the case of both Equation (12) and Equation (13), the three terms on the right-hand side of the equation correspond to the bending, pre-tension and stretching contribution to the elastic response of the 2D membrane, respectively. In the limit of small indentations, $\delta_{mem} < t$, the bending contribution dominates the elastic behavior. However, as soon as the indentation depth increases, the stretching term becomes more and more significant, so that, when $\delta_{mem} >> t$, the bending term can be neglected and Equation (12) and (13) can be re-written as:

$$\text{Circular drum}: \quad F(\delta_{mem}) = \pi T \delta_{mem} + \frac{q^3 Yt}{R^2}\delta_{mem}^3 \tag{14}$$

$$\text{Beam}: \quad F(\delta_{mem}) = \frac{T}{L}\delta_{mem} + \frac{\pi^4 wYt}{8L^3}\delta_{mem}^3 \tag{15}$$

It is worth mentioning that Equations (12) to (15) are modeled in the ideal case of a point load, or zero-size indenter. Vella et al.[156] derived the corresponding behavior of F vs. δ_{mem} in the case of a finite size indenter, R_{tip}, indenting on a circular clamped plate of footprint radius R, in the limit $R_{tip} << R$. The authors calculated the explicit expression of $F(\delta_{mem})$ in the limit of small and large indentations, as well as in the intermediate regime, demonstrating that the simple algebraic sum of linear and cubic terms can often lead to inaccuracies in the estimated values of E_{2D} and T. They found the following F vs. δ_{mem} relationships:

$$\text{Small indentation}: \quad F(\delta_{mem}) = \frac{2\pi T^{\frac{1}{2}}}{log\left(\frac{R}{R_{tip}}\right)}\delta_{mem} \tag{16}$$

$$\text{Intermediate indentation}: \quad F(\delta_{mem}) = \frac{2\pi T^{\frac{1}{2}}}{log\left(\frac{4RT^{\frac{1}{2}}}{\delta E_{2D}^{\frac{1}{2}}}\right)}\delta_{mem} \tag{17}$$

$$\text{Large indentation}: \quad F(\delta_{mem}) = \frac{E_{2D}^{\frac{1}{2}}}{R^2}\delta_{mem}^3 + O\left(\frac{R_{tip}}{R}\delta_{mem}^3\right) \tag{18}$$

for small, intermediate and large indentation regimes, respectively.

From a practical point of view, the realization of a circular-plate membrane typically entails the transfer[32,159–163] or the mechanical exfoliation[3,37,164–166] of the 2D material on top of a substrate, previously patterned with cylindrical holes. Similarly, the fabrication of doubly-clamped beams can be obtained by mechanically exfoliating the 2D material on top of patterned trenches,[167] or in slightly more elaborated ways, requiring the 2D material to be first sandwiched in between PMMA layers[168] or SiO_2 and metal electrodes,[169] and subsequently exposed to e-beam lithography or local etching. When doing so, the 2D material binds tightly with the substrate outside of the patterned holes via vdW interactions.[170] Thus, depending on the fabrication procedure, a free-standing circular-shaped or beam-like membrane is made accessible to the AFM indentation, as schematically shown by **Figures 16**a and b, respectively.

Figures 16c and d show AFM and SEM images of a MoS_2 isolated triangular crystal on top of a holey SiO_2/Si substrate[172] and of a doubly-clamped, 7 nm thick graphene sheet suspended above a trench etched in SiO_2.[167]

The relationship between the indentation load F and displacement δ_{mem} can be thus recorded by performing local AFM nanoindentation on the free-standing areas, and the elastic parameters of interests of the 2D material can be extracted by fitting the measured FDC with the appropriate analytical model.

The AFM indentation experiments on free-standing 2D membranes were first pioneered by Lee et al.,[3] who investigated the elastic properties and intrinsic strength of mechanically exfoliated graphene, suspended on a Si wafer with circular holes. Together with a comprehensive investigation of the elasticity of a monolayer, they also studied the mechanics of bilayer and trilayer graphene sheets, which all resulted in having the same Young's modulus of $Y \sim 1$ TPa ($E_{2D} \sim 330$ N m^{-1}).[173] Annamalai et al.[174] achieved a similar result in monolayer graphene, but found a higher value for the Young's modulus of multilayered stacks ($Y \sim 3.2$ TPa), made of two, three and five sheets. These apparently controversial results shed a light on the role of pre-tension and adhesion forces (between the graphene and its substrate, as well as between the subsequent graphene layers) into the mechano-elastic properties of multilayer graphene. Importantly, they all exhibited a very reproducible elastic behavior, upon loading and uploading the sheets, thus excluding the occurrence of plastic deformations or interlayer slippage, up to the fracture point. Since the pioneristic work of Lee et al.,[3] the AFM nano-indentation of free-standing membranes became a standard tool to investigate the elasticity of 2D materials, their fracture strength and the correlation between mechanics and nanoscale defects. For instance, the main panel of **Figure 17**a shows typical examples of FDCs acquired on free-standing circular-plate-like membranes of 2D materials and relative heterostructures.[172] The superimposed white dashed lines are the corresponding fits performed by using Equation (14), thus assuming a negligible bending contribution. At small indentation depths, the elastic response is dominated by the pre-tension of the membrane, thus scaling linearly with the applied load ($F \propto \delta_{mem}$). At large indentation, the applied load follows a cubic relationship with the membrane displacement ($F \propto \delta_{mem}^3$), as shown by the inset of Figure 17a. The fitting of the FDCs with the corresponding model allowed us to extract the estimate of 2D Young's modulus E_{2D} and pre-tension T. For instance, the inset of Figure 17b shows the statistical distribution of E_{2D}, derived by fitting several FDCs acquired on several single-layer MoS_2 circular plates in ref. [172], resulting in $E_{2D} = (171 \pm 11)$ N m^{-1}. With an analogous analysis, the authors also derived and $E_{2D} = (177 \pm 12)$ N m^{-1} for WS_2, $E_{2D} = (314 \pm 31)$ N m^{-1} for MoS_2/WS_2 heterostructures and $E_{2D} = (467 \pm 48)$ N m^{-1} for MoS_2/graphene heterostructures. The built-up of higher 2D Young's moduli in the considered heterostructures was modeled as:

$$E_{2D,tot} = E_{2D,top} + \alpha E_{2D,bottom} \tag{19}$$

where the *top* and *bottom* indexes refer to the surface and sub-surface layer. The interaction coefficient α, ranging from 0 to 1, depends on the interlayer friction coefficient, the vdW

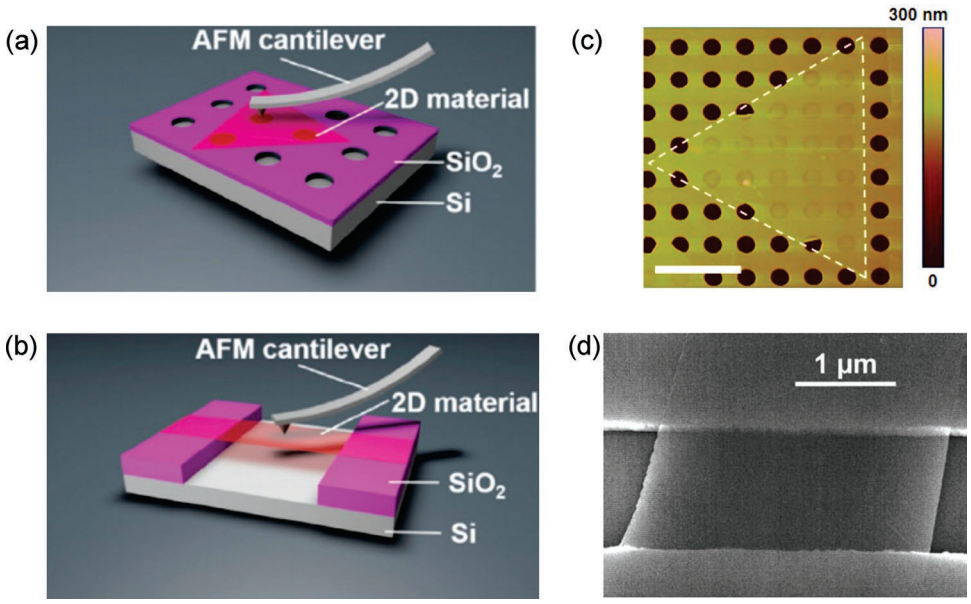

Figure 16. Schematic diagram of AFM nanoindentation on (a) freely-suspended circular drum and (b) doubly-clamped beam. Reproduced under the terms of the CC-BY 4.0 license.[171] Copyright 2019, The Authors, published by John Wiley & Sons Australia, Ltd on behalf of UESTC. c) AFM topography of MoS_2 isolated triangular crystal on top of a holey SiO_2/Si substrate. Reproduced with permission.[172] Copyright 2014, American Chemical Society. d) SEM image of a 7 nm thick graphene sheet suspended above a trench etched in SiO_2. Reproduced with permission.[167] Copyright 2007, American Vacuum Society.

interaction between the layers, the occurrence of slippage, and the indentation-related strain. It is also worth mentioning that their estimates of T in the heterostructures [(0.25 ± 0.05) N m^{-1} and (0.35 ± 0.05) N m^{-1} for MoS_2/WS_2 and MoS_2/graphene, respectively], almost coincide with the sum of the single T of each layer, thus indicating that the pre-tension is simply accumulated as the layers are stacked sequentially by the same transfer process. Figure 17b and **Table 2** summarize the elastic moduli of many different 2D materials, found by using nanoindentation methods, both in the single-layer and few-layer limits. Results from the analysis of the wrinkle profiles (as discussed in the following)[175] and of a few other more complicated methods, including bimodal AFM-based techniques[176] or mechanical resonance measurements,[177] have been also included. Interestingly, the values measured by different groups and using different techniques for the same material are generally in good agreement with each other.

Additionally, AFM-based nanoindentation can be a valuable tool to evaluate the fracture strength of 2D materials.[3] The fracture stress and strain values obtained for different 2D materials are also summarized in Table 2. The main panel of Figure 17c shows the FDC acquired on a free-standing circular membrane of CVD-grown multi-grain single-layer graphene. The red solid line represents the fit by Equation (14), resulting in $E_{2D} = (328 \pm 15)$ N m^{-1}. The authors found that the membrane undergoes a failure when the loading force reaches (2000 ± 420) nN, as shown by the AFM images reported in the inset. By using atomic-scale ab initio density functional theory, they evaluated the correspondent breaking stress of multi-grain graphene and found that it almost coincides with that of pristine, defect-free graphene when in the large-grain configuration (≈40 N m^{-1}), whereas it is slightly reduced in small-grain graphene (≈33 N m^{-1}). Interestingly, Figure 17d compares the fracture loads when indenting on the membrane center (in black) and on selected grain boundaries (GBs) near the center. The fracture loads at the GBs are 20 to 40% smaller, but still correspond to an equibiaxial stress of 30 to 33 N m^{-1}, thus confirming that GBs in graphene can achieve ultrahigh strength.

On the other hand, Frank et al.[167] used AFM nano-indentation experiments to investigate the mechanics of stacks of graphene on patterned trenches, as the one schematically shown in the inset of Figure 17e. By mostly limiting their analysis to the small indentation regime ($\delta_{mem} < t$), the authors acquired the loading FDCs in the center of several beams, differing by the constitutive geometrical parameters (width w, length L, and thickness t). After calibrating the elasticity of the used AFM cantilevers, the authors derived the stiffness, or spring constant k, of the graphene membrane by a linear fit of the FDCs. From Equation (13), neglecting the cubic term, k is expected to be:

$$k = \frac{F}{\delta_{mem}} = \frac{\pi^4 Y}{6} w\left(\frac{t}{L}\right)^3 + \frac{T}{L} \tag{20}$$

Figure 17e shows their results in terms of k vs. $w\left(\frac{t}{L}\right)^3$, for eight different suspended graphene sheets. Given the almost identical beam length L of the different sheets, they modeled the second term in Equation (20) as a constant offset—thus also assuming an almost constant pre-tension T in all the sheets—and confirmed the linear expected behavior of k vs. $w\left(\frac{t}{L}\right)^3$. From the slope of the fit, they derived a Young's modulus of the sheets of 0.5 TPa. Variation of the graphene Y, from 0.4 to 1 TPa were also found by Traversi et al.,[168] performing indentation on a free-standing beam of graphene, sandwiched by two PMMA layers. The observed fluctuations in the Y value were attributed to several possible sources,

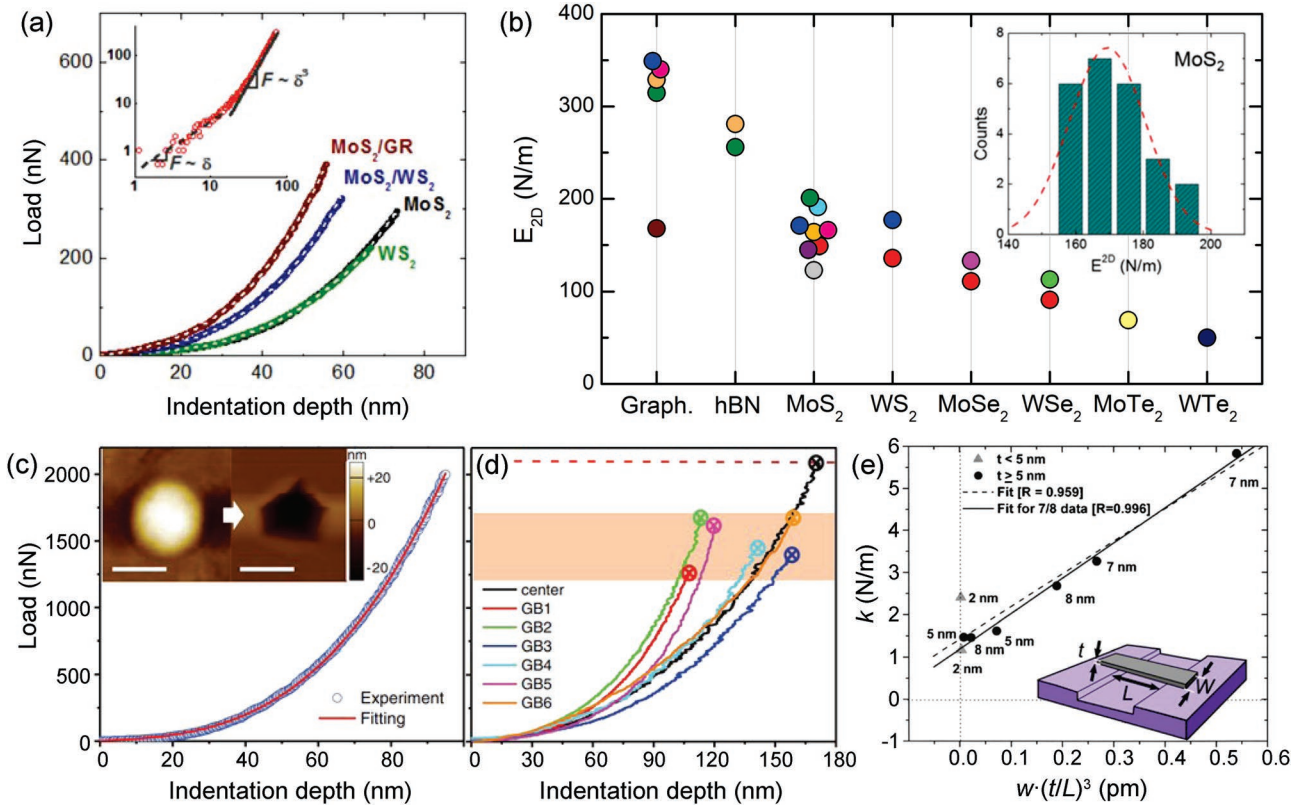

Figure 17. a) Main: FDCs of different CVD-growth monolayers and heterostructures, fitted by Equation (14). Inset: zoom of a typical FDC, highlighting the transition from linear to cubic behavior. Reproduced with permission.[172] Copyright 2014, American Chemical Society. (b) Main: elastic moduli measured experimentally (see Table 2) for the most common 2D materials, including graphene, hBN, and TMDs. All TMDs are in the 2H phase, but for WTe_2 which is in the $1T_d$ phase. These data were measured in refs. [172] (blue) [3], (pink) [178], (olive) [167], (wine) [4], (light-pink) [149], (cyan) [176], (yellow) [32], (purple) [175], (red) [5], (orange) [154], (grey) [179], (magenta) [180], (green) [75], (light-yellow) and (navy) [177]. Whenever E_{2D} was measured for different layer thicknesses, a weighted average of the measured values was here considered. Inset: E_{2D} distribution obtained by a statistics of nano-indentations on several MoS_2 circular membranes. Inset reproduced with permission.[172] Copyright 2014, American Chemical Society. (c) Main: FDC acquired on a CVD-growth graphene circular membrane. Inset: AFM images before and after the membrane's failure point. (d) Comparison of FDCs acquired in the center of a graphene membrane and on grain boundaries (GB). c,d) Reproduced with permission.[160] Copyright 2013, American Association for the Advancement of Science. (e) Inset: sketch of doubly-clamped beam, indicating the constitutive geometrical parameters. Reproduced with permission.[181] Copyright 2014, Wiley-VCH. Main: stiffness k of graphene beams measured by AFM indentation in the center of the suspended region vs. the geometrical parameters of the system $w\left(\frac{t}{L}\right)^3$. Reproduced with permission.[167] Copyright 2007, American Vacuum Society.

such as (i) the crystallographic orientation of graphene with respect to the PMMA windows; (ii) slight changes in clamping condition and point load configuration; (iii) uncertainty in the exact graphene thickness selection; (iv) substrate effect due to the soft PMMA; and (v) PMMA residue on the sheets.

3.2. Nano-Indentation of Micro-Bubbles

The previous section was dedicated to the AFM nano-indentation of free-standing membranes of 2D materials. However, in many cases, the membrane is also subjected to a constant pressure difference, Δp, as in bubbles/blisters of micrometric and sub-micrometric size. These structures have been found spontaneously in 2D materials, as a consequence of the fabrication process, or have been induced ad-hoc and in controlled manners. Both cases have been largely discussed in the previous sections. For instance, the AFM images of Figures 8 and 12b and that in Figure 12d clearly reproduce the two random and engineered configurations for the bubbles. When indenting on a bulged, pressurized membrane, the role of the inner pressurized gas cannot be neglected in the evaluation of the elastic response of the 2D material. By modeling the AFM tip as a finite indenter of radius $R_{tip} \ll R$, where R is the membrane footprint radius, exerting a normal load on the top of the pressurized domes, the problem of indentation on the clamped, pressurized and pre-tensed membrane can be written by incorporating the differential pressure $\Delta p = p - p_0$—where p and p_0 are the internal and external pressure, respectively—in the normal force balance equation:[156]

$$\psi(r)\frac{d\zeta}{dr} = \frac{F}{2\pi} - \frac{\Delta p}{2}r^2 \tag{21}$$

where $\psi(r)$ is the Airy stress function, and $\zeta(r)$ is the out-of-plane membrane displacement due to the simultaneous action of indentation force F. Equation 21 can be solved numerically, together with the strain compatibility equations, in the limits of

Table 2. 2D Young's moduli (E_{2D}) and fracture (or intrinsic) stress (σ_{int}) and strain (ε_{int}) of graphene, hBN and TMDs measured by exploiting mechanical deformations (the specific system used in each work is given). E_{2D} and σ_{int} are calculated for a 1L-thick membrane as $E_{2D}^{1L} = E_{2D}/N$ and $\sigma_{int}^{1L} = \sigma_{int}/N$, where N is the number of layers, in order to have a direct comparison between the displayed values. It should be noticed that different values of the Poisson's ratio ν were used in different works. To have a direct comparison, here we re-scaled some of the values in order to use always the same ν value (displayed in the table) for a given material. As a consequence, the values displayed here might differ slightly from those reported in the original works. The following single-layer thicknesses were considered: $t = 0.625$ nm for TMDs, $t = 0.335$ nm for graphene, $t = 0.333$ nm for hBN.

Material	Ref.	System	Thickness	E_{2D}^{1L} (N m^{-1})	σ_{int}^{1L} (N/m)	ε_{int} (%)
Graphene ($\nu = 0.165$)	Frank et al. [167]	Beam – Indentation	6L–24L	168	/	/
	Wang et al. [182]	Blister – Mechanics	10L–70L	314.7 ± 7.3	/	/
	Lee et al. [3]	Circular drum – Indent.	1L	340 ± 50	43.6 ± 3.4	25
	Falin et al. [4]	Circular drum – Indent.	1L	342 ± 8	41.9	/
			2L	323 ± 8	36.1 ± 1.5	/
			3L	328 ± 3	35.4 ± 2.0	/
			8L	/	28.6 ± 1.8	/
	Liu et al. [172]	Circular drum – Indent.	1L	349 ± 12	/	/
hBN ($\nu = 0.223$)	Wang et al. [182]	Blister – Mechanics	10L–70L	255.9 ± 4.3	/	/
	Falin et al. [4]	Circular drum	1L	287 ± 24	23.5 ± 1.8	~17
			2L	293 ± 19	22.6 ± 2.3	/
			3L	272 ± 15	25.6 ± 0.8	/
MoS_2 ($\nu = 0.250$)	Cooper et al. [154]	Circular drum – Indent.	1L	123 ± 31	16.5	/
	Iguiñiz et al. [175]	Wrinkles	3L–11L	149 ± 21	/	/
	Di Giorgio et al. [5]	Bubble – Indent.	1L	164 ± 39	>15	>12
	Li et al. [176]	Bimodal AFM + FEM	1L	166 ± 8	/	/
	Liu et al. [172]	Circular drum – Indent.	1L	171 ± 11	/	/
	Bertolazzi et al. [32]	Circular drum – Indent.	1L	183 ± 61	15 ± 3	6-11
		Circular drum – Indent.	2L	132 ± 35	14 ± 4	6-11
	Castellanos-Gomez et al. [149]	Circular drum – Indent.	5L–25L	191 ± 40	/	/
	Wang et al. [182]	Blister – Mechanics	10L–70L	200.9 ± 5.4	/	/
WS_2 ($\nu = 0.217$)	Iguiñiz et al. [175]	Wrinkles	3L–8L	136 ± 37	/	/
	Liu et al. [172]	Circular drum – Indent.	1L	177 ± 12	/	/
$MoSe_2$ ($\nu = 0.239$)	Iguiñiz et al. [175]	Wrinkles	5L–10L	133 ± 24	/	/
	Yang et al. [179]	Beam – Stretching	1L	111.9 ± 4.6	1.9 ± 0.4	(1.7 ± 0.4)
			2L	110.2 ± 5.5	3.5 ± 1.8	(3.2 ± 1.8)
WSe_2 ($\nu = 0.196$)	Iguiñiz et al. [175]	Wrinkles	4L–9L	91 ± 22	/	/
	Zhang et al. [180]	Circular drum – Indent.	5L	115.5 ± 4.5	>43	>7.3
			6L	111.4 ± 4.0	/	/
			12L	113.9 ± 4.9	/	/
			14L	111.7 ± 3.9	/	/
2H-$MoTe_2$ ($\nu = 0.235$)	Sun et al. [75]	Circular drum – Indent.	5–6L (3.6 nm)	56	4.5	8.3
			9–10L (6.0 nm)	72	4.4	6.2
			10–11L (6.7 nm)	63	2.8	4.6
1T-$MoTe_2$ ($\nu = 0.235$)	Sun et al. [75]	Circular drum – Indent.	14–15L (9.0 nm)	66	1.7	2.7
			17–18L (11.0 nm)	62	1.6	2.6
T_d-$MoTe_2$ ($\nu = 0.235$)	Sun et al. [75]	Circular drum – Indent.	16–17L (10.5 nm)	66	2.0	3.1
			20–11L (13.0 nm)	65	2.0	3.2
			22–23L (14.0 nm)	55	1.4	2.5
T_d-WTe_2($\nu = 0.16$)	Lee et al. [177]	Nanoresonator	12L–43L	~50	/	/

small and large indentations, leading again to $F = k\delta_{mem}$ (linear regime) and $F = \alpha\delta_{mem}^3$ (cubic regime). Here:

$$k = \frac{2\pi A_\tau (\Delta p R)^{\frac{2}{3}} E_{2D}^{\frac{1}{3}}}{\log\left(\frac{R}{R_{tip}}\right)}, \quad \alpha = f\left(\nu, \frac{R_{tip}}{R}\right)\frac{E_{2D}}{R^2} \tag{22}$$

(A_τ is a tabulated function of Poisson's ratio). It is worth noticing that, differently from indentation on free-standing membranes, the linear stiffness k depends on E_{2D}, as well as on the internal pressure p. By using the expression of k and combining it with the equilibrium height of highly pressurized blisters dictated by Hencky's formula,[183] $h_0 = A_h\left(\frac{\Delta p R^4}{E_{2D}}\right)^{\frac{1}{3}}$ (A_h is a tabulated function of Poisson's ratio), one can demonstrate that the knowledge of both the height of the dome (before AFM indentation) and its stiffness (i.e., the slope of the FDC in the small indentation range) is sufficient for both p and E_{2D} to be inferred.[5,156] Indeed, one can find:

$$E_{2D} = \log\left(\frac{R}{R_{tip}}\right)\frac{A_h^2 R^2 k}{2\pi A_\tau h_0^2} \tag{23}$$

$$\Delta p = \log\left(\frac{R}{R_{tip}}\right)\frac{h_0 k}{(2\pi A_h A_\tau R^2)} \tag{24}$$

where h_0 is the bubble's height at its summit. **Figures 18**a and b show the distribution of both p and E_{2D}, obtained by performing small range indentations on MoS_2 bubbles, and by fitting the results with $F = k\delta_{mem}$. By combining the knowledge of k, and that of the system's geometrical parameters h_0 and R, Di Giorgio et al.[5] used Equation (23) and (24) to quantify E_{2D} and p in two different species of bubbles. Red stars correspond to the nano-indentations performed on bubbles produced randomly by proton irradiation of a MoS_2 bulk crystal. Black scatters result from the indentation of domes produced on demand, with a full control of their lateral size and distribution on top of the sample surface.[39] The measured values of E_{2D} fully lie in the expected range of MoS_2 Young's modulus, highlighted by the yellow region in Figure 18b (see also Table 2), while the estimated p (Figure 18a) discloses an increasing trend as the size of the bubbles is reduced. A similar approach was used by Tan et al.[184] to measure the contents, thickness, and internal pressure of MoS_2 nanoblisters, fabricated by electrochemical water splitting. In particular, the authors compared the pressure evaluated by the model of Vella et al.,[156] by employing nano-indentation on selected blisters, with the one predicted by Hencky's formula[183] and based on the geometry of the bubbles and the elasticity of the membrane. Figure 18c shows the comparison between the two, with ΔP_V and ΔP_H being the differential pressures calculated by using Vella's and Hencky's models, respectively. The two equations produce quantitatively consistent results, thus confirming the consistency between Hencky's and Vella's equations. On the other hand, Khestanova et al.[38] reported on similar results in terms of p vs. bubbles size, in blisters formed spontaneously in mechanically exfoliated graphene and MoS_2. The authors performed nano-indentations experiments and fitted the resulting FDCs by using a model based on the minimization of the total energy of the system. At rest, the total energy is given by:

$$U_{tot} = U_{stretch} + U_{vdW} + U_{int}(V) \tag{25}$$

where $U_{stretch}$ and U_{vdW} are the elastic energy of the membrane and the vdW interaction between the layers (i.e., the energy cost related to the fact that the membrane is detached by the substrate), and $U_{int}(V)$ is the energy of the material inside the bubble, assumed as a function of its volume V. When the bubble is indented, the total energy becomes:

$$U_{tot} = -F\delta_{mem} + U_{stretch}(R,\delta) + U_{vdW}(R) + U_{int}[V(R,\delta_{mem})] \tag{26}$$

where $F\delta_{mem}$ is the work done by the loading force during the indentation. By minimizing Equations (25) and (26), with respect to h_0, R and δ_{mem}, the authors found:

$$P = \frac{E_{2D}}{c_V h_0}\left[4c_1\left(\frac{h_0}{R}\right)^4 + 2c_2\varepsilon_{ext}\left(\frac{h_0}{R}\right)^2\right] \tag{27}$$

$$F = d\left(\nu, \frac{R_{cont}}{R}\right)\cdot E_{2D}\frac{h_0^2}{R^2}\delta_{mem} \tag{28}$$

where $c_{V,1,2}$ are dimensionless constants dependent on the bubble geometry, and ε_{ext} is the membrane external strain, respectively. Equation (28) reproduces the linear behavior of F vs. δ_{mem}, with d being a function of Poisson's ratio, ν, and of the ratio R_{cont}/R, where R_{cont} is the contact radius of the area involved in the loading force application. Figure 18d shows some FDCs acquired by Khestanova et al. and fitted with Equation (28), introducing a nonlinear dependence of the contact area between the AFM tip and the pressurized bubble, able to reproduce the experimentally observed non-linearity. By combining Equations (27) and (28), the authors estimated both E_{2D} and the dependence of p on the bubble size, as reported in Figure 18e. Interestingly, as shown by both Figures 18a[5] and e,[38] the pressure inside these bubbles can easily reach tens of MPa, as their size is reduced.

Additionally, Di Giorgio et al.[185] have also investigated the behavior of MoS_2 bubbles subjected to high loading. As a matter of fact, the cubic F vs. δ_{mem} regime was never reached in the indentation experiments, while the transition between linear and non-linear behavior was clearly observed, as a consequence of moving from the small to the intermediate indentation range. To avoid fitting inaccuracies in the estimate of the system properties, the authors developed a fitting approach based on the combination of linear ($F_L = k\delta_{mem}$) and nonlinear ($F_{NL} = \alpha\delta_{mem}^\omega$) components, both weighted by the Heaviside function $\Theta(\delta_{mem} - \delta_T)$, with δ_T being the depth threshold between the linear and nonlinear regime, at small and intermediate indentation depths, respectively:

$$F(\delta_{mem}) = k\delta_{mem}\cdot\left[1 - \Theta(\delta_{mem} - \delta_T)\right] + \left[k\delta_T + \alpha(\delta_{mem}^\omega - \delta_T^\omega)\right]\cdot\Theta(\delta_{mem} - \delta_T) \tag{29}$$

The stiffness k, the parameter α, the exponent ω, and the threshold δ_T are used as fitting parameters of the measured

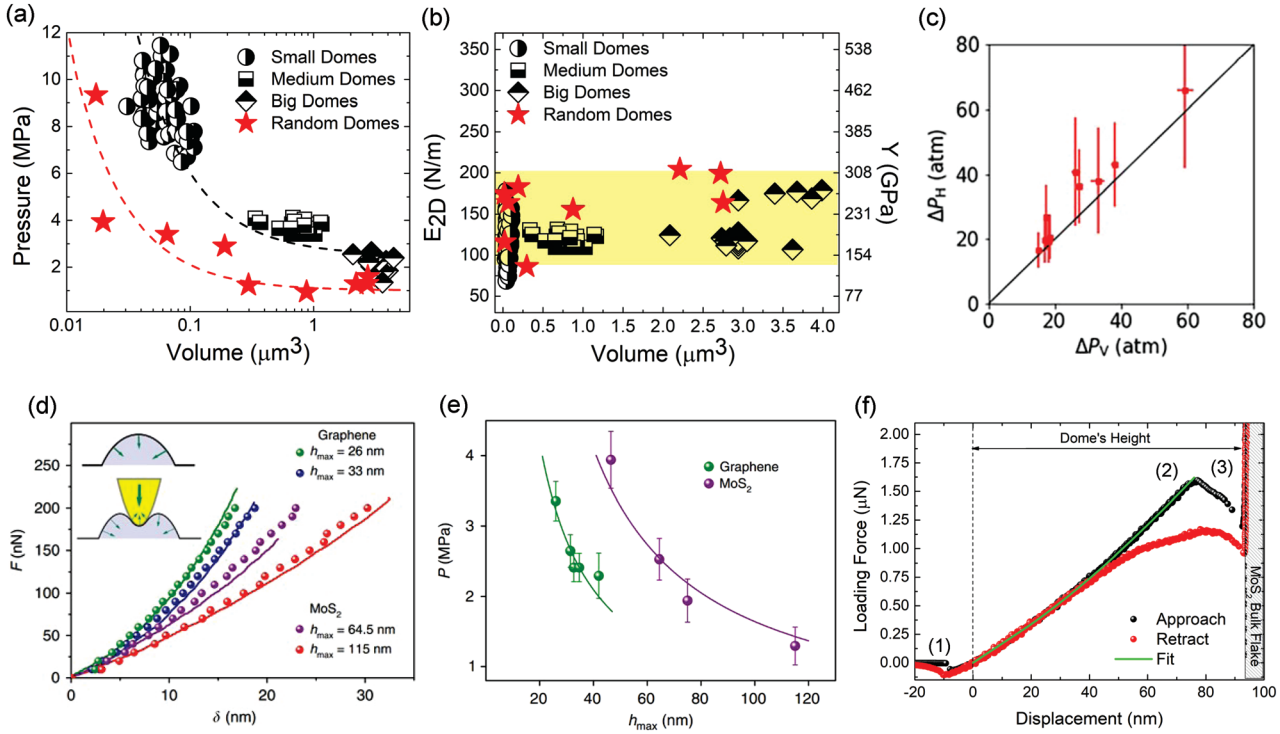

Figure 18. a) H_2 pressure vs. bubble's volume for engineered (half-black scatters) and spontaneous (red stars) domes. Black and red dashed lines work as a guide for the eye to follow the behavior of p versus V. b) Stretching modulus E_{2D} vs. V for engineered (half-black scatters) and spontaneous (red stars) domes. The yellow area highlights the range of E_{2D} values reported in the literature for the MoS_2 monolayer. a,b) Reproduced with permission.[5] Copyright 2020, Wiley-VCH. c) Comparison of pressure estimates, pursued by using the model of Vella et al.[156] ΔP_V, and the one predicted by Hencky's formula[183] ΔP_H. Reproduced with permission.[184] Copyright 2020, American Chemical Society. d) FDCs (solid lines) and numerical fits (symbols) for two graphene bubbles and two monolayer MoS_2 bubbles of different sizes. e) Estimated p vs. h. Solid lines are fits with $\propto \frac{1}{h}$. d,e) Reproduced under the terms of the CC-BY 4.0 license with permission.[38] Copyright 2016, The Authors, published by Springer Nature. f) Typical approach (black scatters) and retract (red scatters) FDCs, with the former fitted by Equation (29) (green line). Reproduced with permission. [185] Copyright 2021, American Chemical Society.

FDCs. Figure 18e shows typical loading (black) and unloading (red) FDCs measured on a MoS_2 dome, produced with site and size control by implementing the method described in refs. [6,39]. The green solid line is the fitting function obtained by using Equation (29). The fit, performed from the tip-membrane snap-to-contact (indicated as feature (1)) to feature (2), agrees with the measured behavior by introducing a non-linearity of $\omega = 1.3$, arising at $\delta_{mem} = (17.1 \pm 0.3)$ nm. Feature (2) has been ascribed by the authors to the emergence of vdW interactions between the bubble membrane and the bulk MoS_2 substrate underneath. The vertical behavior of the FDC at feature (3) corresponds to the indentation of the bulky substrate, reached after the AFM tip has traveled through the bubble by a distance equivalent to its height. Importantly, no irreversible changes are induced in the bubble by the indentation operation, as the unloading curve aligns back to the loading one. The origin of the hysteresis observed between the two curves is attributed to the adhesion between the bubble membrane and the bulky substrate and will be further discussed in Section 4.

3.3. Characterization of Wrinkles

A less common but still valuable strategy to characterize the elasticity of a 2D material consists in the investigation of its wrinkled configuration. As discussed in Section 2.2.1, wrinkled 2D materials can be fabricated by transferring the 2D layers onto either stretchable or thermally shrinkable substrates. A pre-stretched substrate, gradually relaxing, imposes a compressive strain in the overlying 2D material. When reaching a critical strain value, wrinkles develop with an initial periodicity—or wavelength—:[186–188]

$$\lambda = 2\pi t\left[\frac{E_{2D}}{12\Lambda\mu_s(1-\nu)^2}\right]^{1/3} \tag{30}$$

where t is the flake thickness, μ_s is the shear modulus of the substrate, and Λ is related to the pre-strain ε_{pre} of the substrate, as $\Lambda = \frac{1+(1+\varepsilon_{pre})^3}{2(1+\varepsilon_{pre})}$. It can be demonstrated that, under specific conditions, the wavelength (λ) of these ripples is independent of the initial pre-stress of the elastomeric substrate and it only depends on the materials properties of both flake and substrate through the formula:[84,175,189,190]

$$\lambda = 2\pi t\left[\frac{(1-\nu_s^2)E_f}{3(1-\nu_s^2)E_s}\right]^{1/3} \tag{31}$$

where ν_s and ν_f are the Poisson's ratios of substrate and flake, and E_s and E_f are the Young's moduli of the substrate and flake,

respectively. This equation is valid provided that: i) the flake should follow a sinusoidal rippling (see Equation (2)), ii) $E_f/E_s \gg 1$, iii) the substrate is much thicker than the flake, iv) the amplitude of the ripples is much smaller than their wavelength (thus shear forces are negligible), v) the adhesion between the flake and substrate is strong enough to prevent slippage, and vi) all the deformations are assumed to be elastic.

The experimental measurement of the wrinkle period can be thus employed to asses the value of the 2D material elastic modulus; see Table 2. This method has often been referred to as buckling metrology.[84,175]

4. Adhesive Properties of van der Waals Materials

Blisters and bubbles represent excellent candidates to probe not only the elastic properties of the 2D membrane, but also vdW adhesion forces.

This is particularly relevant because such forces rule the fundamental physics of layered materials: if graphene and other 2D materials could be isolated, it is definitely thanks to the fact that the different layers are kept together by weak vdW forces. Despite the importance of vdW adhesion, its experimental quantification remained prohibitive for a long time. Indeed, density functional theory (DFT) calculations allowed for its estimation,[191,192] but the coexistence of weak vdW and strong covalent bonds did not allow for an accurate material-dependent characterization. Experimental methods to probe the vdW adhesion based on blisters and bubbles started to be developed.[70,72,170,185,193,194] Here, we review some of these methods and provide an overview of the in-depth characterization of the vdW adhesion energy they allowed us to achieve.

4.1. Donut Blisters and Nano-Indented Bubbles

An interesting method based on blisters to probe the adhesion between a 2D membrane and a metallic or Si-based surface was developed by Liu et al.[194] Their studies relied on the design of blisters such as those in Figure 5, but in a slightly different geometry. In particular, graphene flakes were in this case suspended over an annular ring etched into a silicon oxide wafer (bare SiO_x or gold-coated SiO_x), forming a graphene-sealed microcavity, such as that shown in **Figure 19**a. The graphene membranes were then pressurized using the approach previously discussed (refer to Figure 5b). In this new geometry, however, if the device is only weakly pressurized, the graphene sheet remains adhered to the inner post and deforms in a donut shape, see Figure 19a, left. At sufficiently high Δp, the force is large enough to overcome the adhesion energy of the graphene flake to the inner post, and the graphene membrane delaminates from it, becoming a spherical cap, see Figure 19a, right.
Indeed, the membrane sticks to the inner post only if the distance between them is low enough, so that the membrane can feel the vdW attraction. To study this phenomenon in more detail, Liu et al.[194] employed the following strategy: After creating deformed spherical caps, the gas was slowly let to diffuse out of the microcavity through the underlying SiO_x substrate, thus decreasing Δp and the corresponding central deflection, h_0, of the graphene membrane, until the membrane was pulled back onto the post due to attractive interactions. This process was monitored in real-time using an AFM. A statistical analysis of the distance at which the membrane sticks to the post—referred to as pull-in distance—could then be carried out; the results are shown in Figure 19b, for graphene flakes of thickness ranging between 1 and 5 layers. The vdW attraction can be modeled in terms of an attractive pressure of the form:

$$P_{\mathrm{vdW}} = \frac{\beta}{h_0^4} \tag{32}$$

where β is a constant which accounts for the vdW attraction. Since P_{vdW} equals the device pressure at the pull-in distance, β can be estimated straightforwardly, as shown in the bottom panel of Figure 19b. Indeed, β scales linearly with the number of layers, confirming the additive nature of vdW forces.[194]

A similar experiment to that just discussed was performed also by Di Giorgio et al. on one-layer-thick MoS_2 bubbles.[185] In this case, the membrane was brought closer and closer to the underlying bulk MoS_2 flake, in order to probe the vdW interaction between ML and bulk. To push the membrane down, an AFM tip was employed, as sketched in Figure 19c. Differently from the indentation experiments discussed before—aimed at probing the elastic modulus of the membrane by pushing it down for a short distance—this study took the full indentation curve into account, up to the point in which the membrane sticks to the bulk. To perform such an experiment, bubbles created in ordered arrays were exploited, such as those shown in Figure 12d. This was essential, since random bubbles (i.e., not contained within openings) slide during indentations, thus not enabling to perform a full indentation procedure.[185] An exemplifying AFM image of a bubble fully indented multiple times is shown in Figure 19d. Notably, no variations can be observed between the bubble morphology before and after the indentation procedures, highlighting how the system fully recovers its initial shape without any membrane damage or gas leakage. Indeed, when performing a full indentation, the initial part of the FDC is analogous to that discussed previously, showing a linear relationship between the force and the distance, see the black curve in Figure 19e. Interestingly, however, by further pushing down the tip, an abrupt decrease in the force is observed (feature (2) in Figures 19c and 19e). Such a decrease continues until the tip/membrane systems touch the substrate (feature (3) in Figures 19c and 19e). Initially, when the tip is retracted, see the red curve in Figure 19e, the curve does not overlap with the approach curve; at large membrane-to-bulk distances, however, the two curves show a near-perfect overlap. This result proves that the bubble can withstand very large deformations without damaging, and suggests an analogy between the bubble system and superelastic materials. This analogy is suggested by the presence of: i) two subsequent elastic branches, representative of indentation on the bulged MoS_2 monolayers, and on the bulk (feature (3)), respectively; ii) a large hysteresis when performing a loading-unloading cycle because of the system transition from ML to bulk (when the ML sticks to the substrate); and iii) full reversibility of the whole process. The observed behavior can be explained in terms of vdW forces between the ML and the bulk, which start playing a role when the membrane is pushed

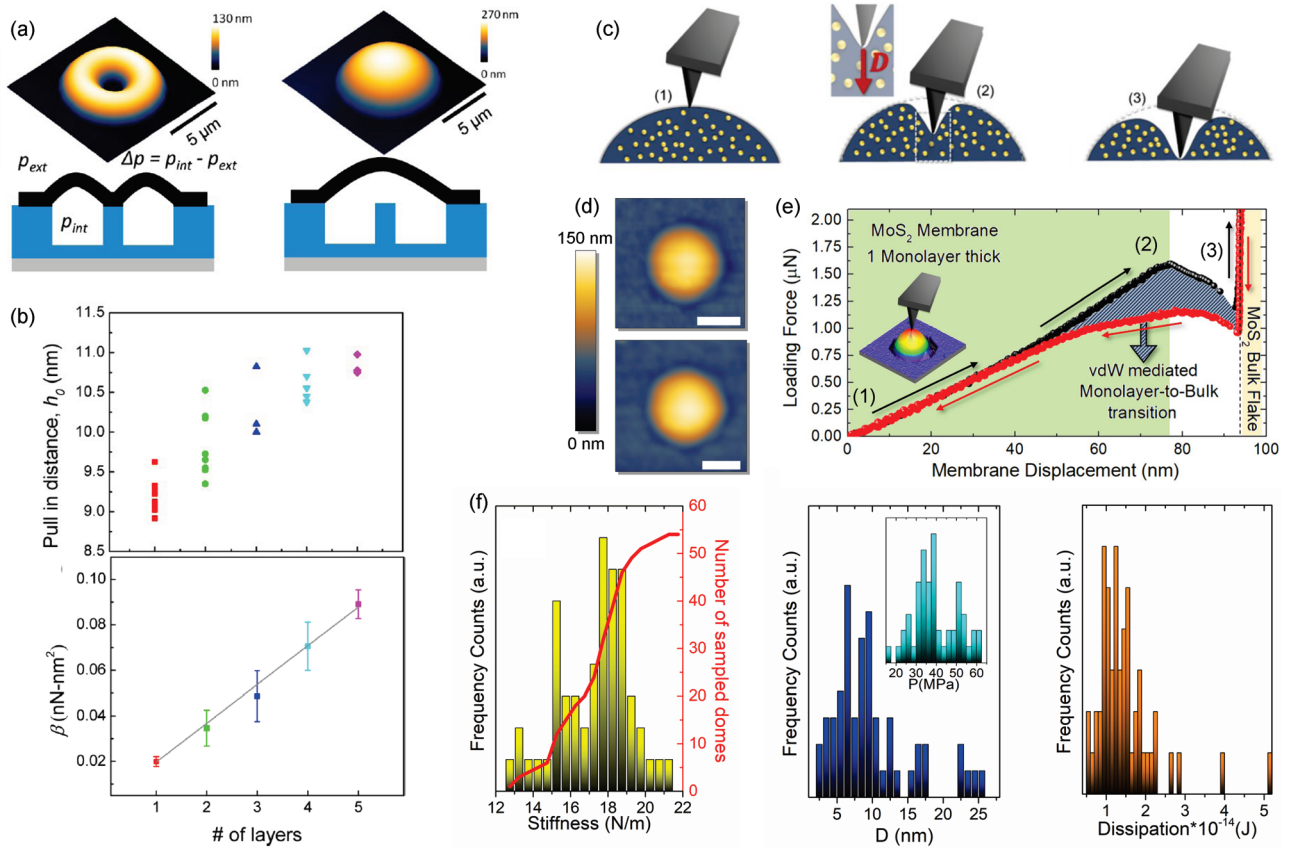

Figure 19. a) Top: 3D AFM image of a pressurized graphene membrane in the annular ring geometry before (left) and after (right) delamination from the inner post. Bottom: Side view schematic of the pressurized suspended graphene on the annular ring. b) Top: Statistical measurements of the pull-in distance h_0 (i.e., distance at which the membrane sticks to the inner post) for graphene membranes of different thickness (between 1 and 5 layers) in an annular ring geometry. Bottom: Calculated values of the constant β in Equation (32) vs. number of layers. A best fit line through the data is also shown which has a slope of 0.017 nN nm^{-2}/number of layers. a,b) Adapted or reproduced with permission.[194] Copyright 2013, American Chemical Society. c) Scheme depicting the main steps of an indentation process of an H_2-filled bubble: (1) The AFM tip approaches the dome; (2) The tip pushes down the membrane, and when the membrane is close enough to the bulk flake beneath (at a distance D), van der Waals forces attract the membrane; (3) The membrane is brought into contact with the bulk flake. d) Tapping-mode AFM topography (of a 1.6 μm × 1.6 μm area) of the same dome before (top) and after (bottom) multiple indentation procedures: No differences can be observed at the end of the process. The scale bar is 500 nm. e) Typical approach (black scatters) and retract (red scatters) FDCs. Steps (1)–(3) refer to the sketches of panel (c). f) Left: Stiffness distribution (histogram) and cumulative function (red line) obtained by fitting 54 approach FDCs with Equation (29). Center: Distribution of the distance D between the feature (2) and the bulk MoS_2 flake (feature (3)); Inset: inner pressure distribution at D. Right: Dissipation distribution evaluated by measuring the hysteresis between the approach and retract FDCs. c–f) Reproduced with permission.[185] Copyright 2021, American Chemical Society.

close enough to the substrate, in analogy with the donut blister experiment. Indeed, the attractive vdW interaction decreases the force needed to push the membrane down, leading to feature (2) in the FDC. Such a peculiar diagram allows one to extract various information on the system. First, by fitting the FDC from feature (1) to feature (2) by Equation (29), it is possible to estimate the membrane stiffness. The stiffness values estimated by performing a full indentation procedure on 54 MoS_2 bubbles are displayed in Figure 19f, left. Second, by making a statistical analysis of the distance D between features (2) and (3), it is possible to observe how the vdW attraction starts to play a significant role at a distance of ≈ 7 nm, see the central panel of Figure 19f. This result is in excellent agreement with the pull-in distance estimated in donut blisters.

The experiment here discussed can provide further information if a more quantitative analysis is carried out. In particular, one can model the problem of an indenter pushing against the pressurized bubble as a quasistatic process where, point by point:[185]

$$F_{\text{probe}} - F_{\text{gas}} + F_{\text{vdW}} = 0 \tag{33}$$

F_{probe} being the force exerted by the AFM tip, F_{gas} that exerted by the gas and F_{vdW} being the vdW interaction force between the dome and the bulk flake beneath. The latter is non-negligible only when the membrane-to-bulk distance D is small enough, see Figure 19f, central panel. If we assume that the only portion of the membrane subjected to the vdW attraction is that close to the indenter tip, and that the membrane acquires the same curvature of the AFM tip (with curvature radius R_{tip}), the vdW interaction can be modeled in the geometry of the sphere-plane interaction, as:[185]

$$U_{\text{vdW}} = -\frac{HR_{\text{tip}}}{6\pi D} \tag{34}$$

where H is the so-called Hamaker constant ($H = 6.51 \times 10^{-19}$ J for a MoS_2 ML on a MoS_2 bulk flake[185]). In turn, the vdW force can be calculated as:

$$F_{\mathrm{vdW}} = -\frac{dU}{dD} = -\frac{HR_{\mathrm{tip}}}{6\pi D^2} \tag{35}$$

Once F_{vdW} is derived, and being F_{probe} a known quantity, it is possible to derive F_{gas} from Equation (33), and thus the gas pressure P_{gas} by dividing F_{gas} by the indented area. The pressure estimated with this approach in the same full indentation procedures made to estimate the stiffness and D is shown as inset in Figure 19f, central panel. Finally, it should be noticed that the hysteresis between the approach and retract FDCs provides information on the energy dissipated during the indentation process. In particular, it can be demonstrated that the total work W done by the tip equals the work done by the vdW force:[185]

$$W_{\mathrm{probe}}^{\mathrm{approach}} - W_{\mathrm{probe}}^{\mathrm{retract}} = -(W_{\mathrm{vdW}}^{\mathrm{approach}} - W_{\mathrm{vdW}}^{\mathrm{retract}}) \tag{36}$$

Figure 19f, right panel, displays a statistical analysis of the energy dissipated when performing full indentation procedures, with values mostly ranging between 0.5 and 2.3×10^{-14} J. By roughly normalizing these values to the tip area ($A_{\mathrm{tip}} = \pi R_{\mathrm{tip}}^2$), one finds $(4.7 \pm 2.5) \times 10^{-21}$ J Å^{-2} = 30 ± 16 meV Å^{-2}, remarkably close to the adhesion energy expected from DFT calculations[191,192] and to that estimated experimentally with the approach we will discuss in the following section.[72]

4.2. Energy Minimization in Microscopic Bubbles

A somewhat simpler approach to estimate the adhesion energy between different vdW materials relies on the study of the equilibrium shape of 2D material bubbles. Indeed, the total energy of the system is given by:

$$U_{\mathrm{tot}} = U_{\mathrm{int}} + U_{\mathrm{stretch}} + U_{\mathrm{bend}} + U_{\mathrm{adh}} \tag{37}$$

where U_{int} represents the internal energy of the fluid within the bubble, U_{stretch} and U_{bend} are the elastic energy contributions associated with stretching and bending, and U_{adh} is related to the detachment of the membrane from the substrate. The bending term is generally negligible, and would contribute only to very small and rather thick bubbles. For sake of completeness, we include it in our equations and we will neglect it a posteriori. These energy contributions can be expressed as:

$$U_{\mathrm{int}} = -\Delta p \int_0^R \int_0^{2\pi} dr \cdot r d\theta \cdot h(r) \tag{38}$$

$$U_{\mathrm{stretch}} = \int_0^R \int_0^{2\pi} dr \cdot r d\theta \cdot \frac{E_{2\mathrm{D}}}{2(1-\nu^2)} (\varepsilon_r^2 + 2\nu\varepsilon_r\varepsilon_\theta + \varepsilon_\theta^2) \tag{39}$$

$$U_{\mathrm{bend}} = \int_0^R \int_0^{2\pi} dr \cdot r d\theta \cdot \frac{D}{2} \left[h''(r)^2 + \frac{1}{r^2} h'(r)^2 + \frac{2\nu}{r} h'(r) h''(r) \right] \tag{40}$$

$$U_{\mathrm{adh}} = \gamma \pi R^2 \tag{41}$$

Here, Δp is the difference between the trapped fluid pressure and the external pressure; $E_{2\mathrm{D}}$ is the 2D Young's modulus of the membrane and D is its bending stiffness.

Indeed, the height profile and strain components can be described by Equations (5) and (6).

The equilibrium condition for the system can be described by minimizing U_{tot} with respect to h_0 and R. From $\partial_h U_{\mathrm{tot}} = 0$ we get:

$$\Delta p = \frac{q+2}{2} \left[4\zeta(\nu, q) \frac{E_{2\mathrm{D}}}{1-\nu^2} f^2(\nu, q) \cdot \frac{h_0^3}{R^4} + 2\xi(\nu, q) D \cdot \frac{h_0}{R^4} \right] \tag{42}$$

where

$$\zeta(\nu, q) = \left[(1+\nu) \cdot \frac{q - 1 - g(\nu, q)}{q} + \frac{g^2(\nu, q) + 1 + 2\nu \cdot g(\nu, q)}{2(2q-1)} \right] \tag{43}$$

and

$$\xi(\nu, q) = q^2 \cdot \frac{q + 2(q-1)\nu}{2(q-1)} \tag{44}$$

Finally, by minimizing U_{tot} with respect to R and considering Equation (42), we get:

$$\gamma = 5\zeta(\nu, q) \frac{E_{2\mathrm{D}}}{1-\nu^2} f^2(\nu, q) \cdot \frac{h_0^4}{R^4} + 3\xi(\nu, q) D \cdot \frac{h_0^2}{R^4} \tag{45}$$

It should be noticed, however, that the bending term is generally negligible, unless very small and thick bubbles are considered. By neglecting the bending term, we see that the morphology of the bubble—described by its aspect ratio h_0/R—is directly linked to the ratio between the adhesion energy γ and the elastic modulus $E_{2\mathrm{D}}$, being $h_0/R \propto (\gamma/E_{2\mathrm{D}})^{1/4}$. This result agrees with the experiments discussed previously, showing how bubbles made of a given material on a given substrate are always characterized by the same universal aspect ratio.[38,39,72] This is exemplified in **Figure 20**a–b, where a statistical analysis of the aspect ratios measured for different homostructured bubbles (panel (a), where the bubble is made of the same material of the substrate) or heterostructured bubbles (panel (b), where the bubble and the substrate are made of different layered materials) was performed. Indeed, once the universal aspect ratio is determined, it is possible to estimate the adhesion energy γ via Equation (45), given that $E_{2\mathrm{D}}$ is known by experiments such as those discussed previously, the Poisson's ratio ν is known from theory, and the constant q in Equation (5) has been determined experimentally.[72] The adhesion energy values determined with this approach for several vdW material combinations are shown in Figure 20c and collected in **Table 3**.

Remarkably, γ varies by about one order of magnitude depending on the material combination, in contrast with the material-independent adhesion energy estimated for layered materials by DFT.[191,192] Indeed, on the one side DFT calculations encounter difficulties in finding appropriate functionals to describe the system whenever strong local atom bonds and weak nonlocal vdW forces coexist. On the other side, DFT

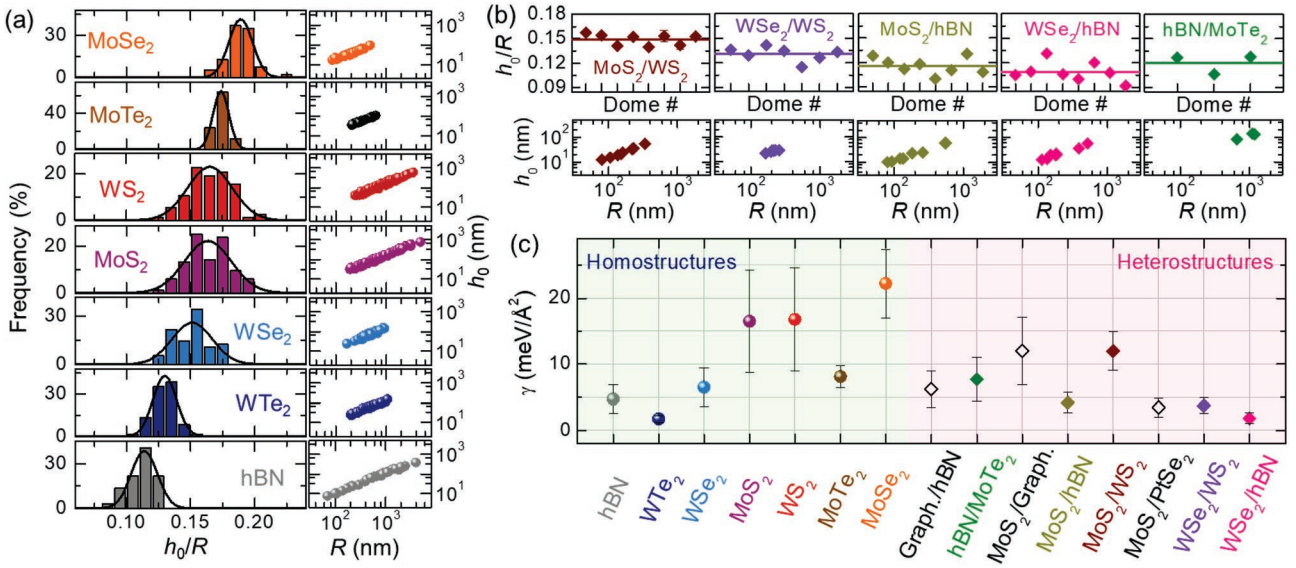

Figure 20. a) Histograms of the aspect ratios (left) and corresponding h_0 vs. R values (right) measured in homostructured bubbles. b) h_0/R values (top; the lines are average values) and corresponding h_0 vs. R values (bottom) obtained for heterostructured bubbles (where the first material refers to the bubble and the second one to the underlying substrate). c) Adhesion energies γ obtained via Equation 45. a–c) Reproduced with permission.[72] Copyright 2021, American Physical Society.

simulates an ideal system, which might differ from the real crystal, being characterized by the intrinsic presence of defects or subjected to oxidation. The development of methods to probe the adhesion energy experimentally—like those presented in this section—is therefore of prominent relevance.

Indeed, different material combinations are characterized by different adhesion energies, as a consequence of several possible factors such as the different interplay between covalent and vdW bonds in different chemical environments, the presence of a slightly ionic bonding character in some crystals, or the tendency of the materials to oxidize.[72]

To conclude this section, it should be noticed that several works reported on the formation of water-filled (or more generally, liquid-filled) bubbles when depositing 2D materials on a substrate.[70,195] Such water-filled bubbles typically form along with hydrocarbon-filled bubbles. Interestingly, these bubbles are still characterized by a constant aspect ratio (independent of the bubbles size), which is however lower than that of gas-filled bubbles.[70,72] To describe the mechanics of water-filled bubbles, Sanchez et al.[70] started from the membrane approach (height profile given by Equation (4)), and developed a modified description of the system where the adhesion energy is still related to the aspect ratio but comprises an additional term:

$$\gamma = \frac{E_{2D}}{\phi}\cdot\frac{h_0^4}{R^4} + \gamma_m(\cos\theta_m + \cos\theta_s) \tag{46}$$

Here, γ_m represents the liquid surface tension, and θ_m and θ_s are the liquid contact angles of the membrane and the substrate, respectively.[70] The bending term was neglected. The constant ϕ was discussed to depend on possible sliding effect and the authors assumed $\phi = 1.2$ corresponding to a weak interface model.[70] This model allowed to quantify the adhesion energy for several combinations of 2D material/substrate. It should be noticed, however, that the adhesion energy estimated for graphene/SiO_2 and for MoS_2/SiO_2 is remarkably smaller than that estimated with other methods; see Table 3. This discrepancy requires further investigation.

4.3. Blisters: Energy Minimization and Friction

A somehow similar approach used to study the equilibrium shape of the bubbles had been previously developed to study pressurized blisters. This approach allowed researchers to estimate the adhesion energy between 2D materials and Si-based or metallic substrates. We consider once more the total energy of the system, which is given by:[35,193,196]

$$U_{tot} = U_{int} + U_{stretch} + U_{bend} + U_{ext} + U_{adh} \tag{47}$$

The meaning of the different terms is analogous to that of Equation (37), plus U_{ext} that represents the free energy change of the external environment that is held at a constant pressure p_{ext}. In fact, at variance with the bubble case, we are here considering an isothermal gas expansion at a fixed number of molecules N. The bending contribution is generally negligible, so that hereinafter we will not consider it anymore. Let us consider a geometry analogous to that of Figure 5b, where R_0 is the radius of the cylindrical cavity, R is the actual radius of the bulged membrane, and h_0 is its maximum height (at the blister center). The free energy change due to isothermal expansion of the fixed number of gas molecules N in the microchamber, from an initial pressure and volume (p_0, V_0) to a final pressure and volume (p_{int}, $V_0 + V_b$), is:[35,193,196]

$$U_{int} = -\int p dV = -p_0 V_0 \ln\left[\frac{V_0 + V_b}{V_0}\right] \tag{48}$$

Table 3. Adhesion energy (γ) between different 2D materials on different substrates, obtained through the methods discussed in this work. The data by Deng et al. were rescaled since the authors employed a MoS_2 elastic modulus (E_{2D} = 124 N m^{-1}) lower than the elastic modulus on average measured in the literature ($E_{2D} \approx$ 170 N m^{-1} from the data in Table 2).

Material/substrate	Ref.	System	γ[meV Å^{-2}]
Graphene/HOPG	Sanchez et al. [70]	Liquid-filled bubbles – Energy Minimization	5.4 ± 1.0
Graphene/MoS_2	Sanchez et al. [70]	Liquid-filled bubbles – Energy Minimization	8.7 ± 1.6
Graphene/hBN	Blundo et al. [72]	Gas-filled bubbles – Energy Minimization	6.2 ± 2.7
Graphene/SiO_2	Boddeti et al. [193]	Blisters – Energy Minimization	15, ~27
	Koenig et al. [170]	Blisters – Energy Minimization	19
	Sanchez et al. [70]	Liquid-filled bubbles – Energy Minimization	5.81 ± 0.06
Graphene/Ice	Sanchez et al. [70]	Liquid-filled bubbles – Energy Minimization	7.9 ± 1.9
Graphene/CaF_2	Sanchez et al. [70]	Liquid-filled bubbles – Energy Minimization	6.5
hBN/hBN	Blundo et al. [72]	Gas-filled bubbles – Energy Minimization	4.7 ± 2.2
hBN/$MoTe_2$	Blundo et al. [72]	Gas-filled bubbles – Energy Minimization	7.7 ± 3.3
MoS_2/hBN	Blundo et al. [72]	Gas-filled bubbles – Energy Minimization	4.2 ± 1.6
MoS_2/MoS_2	Blundo et al. [72]	Gas-filled bubbles – Energy Minimization	16.7 ± 7.7
	Di Giorgio et al. [185]	Bubbles – Indentation	30 ± 16
MoS_2/Graphite	Blundo et al. [72]	Gas-filled bubbles – Energy Minimization	12.0 ± 5.1
MoS_2/WS_2	Blundo et al. [72]	Gas-filled bubbles – Energy Minimization	12.0 ± 2.9
MoS_2/$PtSe_2$	Blundo et al. [72]	Gas-filled bubbles – Energy Minimization	3.4 ± 1.4
MoS_2/SiO_2	Lloyd et al. [35]	Blisters – Energy Minimization	14 ± 2
	Deng et al. [197]	Wrinkles – Energy Minimization	14.4 ± 2.8
	Sanchez et al. [70]	Liquid-filled bubbles – Energy Minimization	5.12 ± 0.06
MoS_2/Si_3N_4	Deng et al. [197]	Wrinkles – Energy Minimization	21.3 ± 3.5
MoS_2/Al_2O_3	Sanchez et al. [70]	Liquid-filled bubbles – Energy Minimization	6.3 ± 0.9
WS_2/WS_2	Blundo et al. [72]	Gas-filled bubbles – Energy Minimization	16.8 ± 7.8
$MoSe_2$/$MoSe_2$	Blundo et al. [72]	Gas-filled bubbles – Energy Minimization	22.2 ± 5.2
WSe_2/WSe_2	Blundo et al. [72]	Gas-filled bubbles – Energy Minimization	6.5 ± 2.9
WSe_2/WS_2	Blundo et al. [72]	Gas-filled bubbles – Energy Minimization	3.7 ± 2.2
WSe_2/hBN	Blundo et al. [72]	Gas-filled bubbles – Energy Minimization	1.8 ± 0.8
$MoTe_2$/$MoTe_2$	Blundo et al. [72]	Gas-filled bubbles – Energy Minimization	8.1 ± 1.7
WTe_2/WTe_2	Blundo et al. [72]	Gas-filled bubbles – Energy Minimization	1.7 ± 0.5

It can also be shown that by assuming a quasistatic expansion of the gas:[35,193,196]

$$U_{\text{stretch}} = \frac{\Delta p V_b}{4} \tag{49}$$

where Δp is the difference between external and internal pressure. Additionally, as the blister expands by V_b, the volume of the surroundings decreases by an equal amount. Assuming the surroundings are maintained at a constant pressure p_{ext}, the energy then changes by:[35,193,196]

$$U_{\text{ext}} = p_{\text{ext}} \int dV = p_{\text{ext}} V_b \tag{50}$$

Finally, the adhesion term is given by:[35,193]

$$U_{\text{adh}} = \gamma \pi (R^2 - R_0^2) \tag{51}$$

When a device is removed from the pressure chamber, the bubble volume expands until the total energy of the system U_{tot} reaches a local minimum. Then, the equilibrium condition is obtained by minimization of the free energy $\partial_R U_{\text{tot}} = 0$. We should recall that $V_b \propto R^2 h_0$, and that—as in the bubble case (see Equation (42))—$h_0 \propto (\Delta p R^4 / E_{2D})^{1/3}$.

To study the system, we have to consider that two different regimes can be achieved depending on the initial device pressure p_0: i) if the pressure is below a certain critical value p_{cr} (i.e., $p_0 < p_{\text{cr}}$), the radius is fixed to the opening radius $R = R_0$ while the height of the blister varies with pressure (see blueish curves in **Figure 21**a and the top sketch in panel b); ii) if $p_0 > p_{\text{cr}}$, the membrane delaminates from the substrate close to the cavity edges, and the blister radius is therefore larger than the cavity radius, $R > R_0$ (see reddish curves in Figure 21a and the bottom sketch in panel b).

Interestingly, the transition from the two configurations is sharp: as shown in panel (a), $R = R_0$ up to 600.4 kPa, and then jumps to a higher value for p_0 = 605 kPa; at higher pressures up to 750 kPa, R varies very little (see inset).

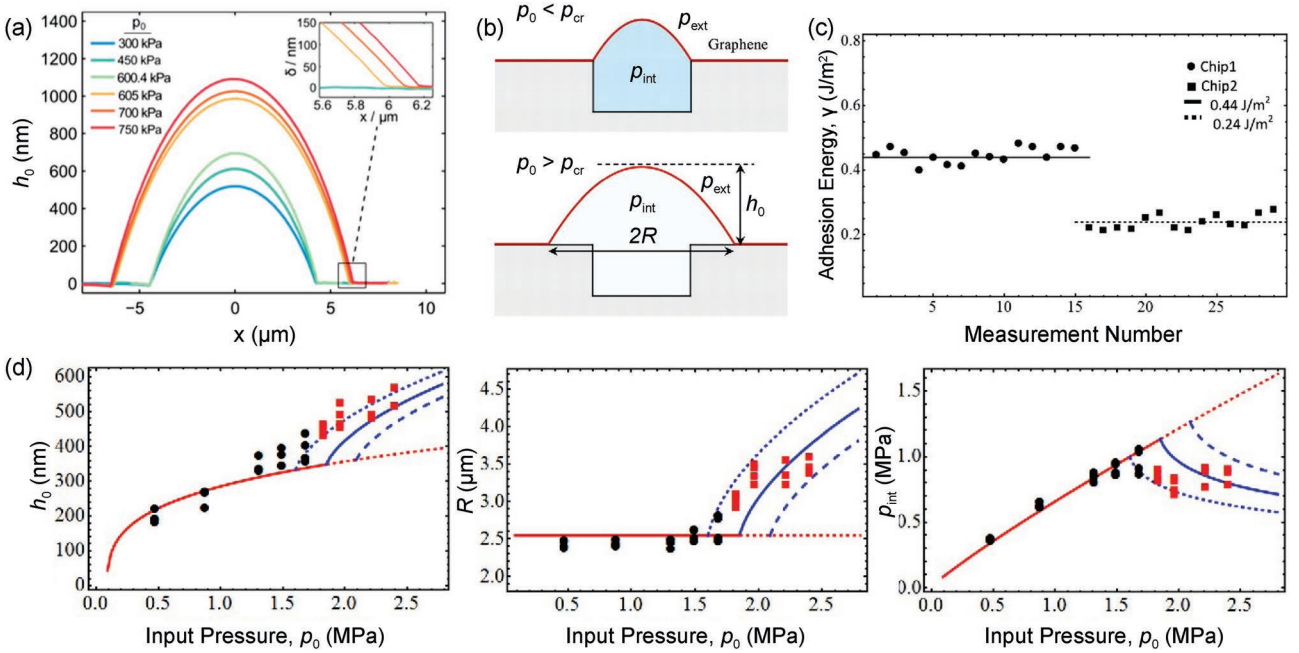

Figure 21. a) AFM cross-section of a MoS_2-based pressurized blister device for several pressure values (scale bar is 5 μm). A delamination occurs between 600.4 and 605 kPa. Adapted with permission.[35] Copyright 2017, American Chemical Society. b) Schematic cross-sections illustrating the two possible final configurations when the graphene membrane is deformed. Initially, the system is brought to a pressure p_0 in a pressure chamber. The device is then brought outside to the external atmospheric pressure p_{ext}, and the internal pressure consequently becomes p_{int}. If $p_0 < p_{cr}$, in the final state $R = R_0$, i.e., the blister radius coincides with the cavity radius (top); if instead $p_0 > p_{cr}$, the membrane delaminates from the substrate and $R > R_0$. The change of the blue color from a darker to a lighter shade indicates decreasing pressure. c) Adhesion energies for monolayer graphene membranes on two different SiO_2 substrates/chips. The average adhesion energy is 0.44 J m^{-2} for Chip 1 and 0.24 J m^{-2} for Chip 2. d) Maximum deflection (left), blister radius (center), and final internal pressure (right) in graphene blisters. The black symbols are from measurements and the solid curves are from the analysis with: no delamination (red), and delamination for different values of adhesion energy: $\gamma = 0.2$ J m^{-2} (dashed blue), $\gamma = 0.24$ J m^{-2} (solid blue) and $\gamma = 0.28$ J m^{-2} (long-dashed blue). The red symbols are those that were used to determine the adhesion energies in panel (c). b–d) Adapted with permission.[193] Copyright 2013, The American Society of Mechanical Engineers.

Considering that from the ideal gas law $p_0V_0 = p_{int}(V_0 + V_p)$, by minimizing the total energy ($\partial_R U_{tot}$) we have that in the delamination configuration:[35,193]

$$\gamma = \frac{5C(\nu)}{4}\left(\frac{p_0V_0}{V_0+V_b} - p_{ext}\right)h_0 \tag{52}$$

where $C(\nu)$ is a function of the Poisson's ratio that links the blister volume to its radius and height ($V_b = C(\nu)\pi R^2 h_0$).

In the experiments, p_0 and p_{ext} are known, as well as R and h_0 (which are measured by AFM) and in turn V_b, and finally $V_0 = \pi R_0^2 h$, where h is the cavity depth. The adhesion energy can thus be estimated analytically, as shown in Figure 21c for two devices where graphene sheets were deposited on SiO_2 substrates. Quite different adhesion energy values equal to 0.24 J m^{-2} = 15 meV $Å^{-2}$ and 0.44 J m^{-2} = 27 meV $Å^{-2}$ were estimated for the two devices. The constant $C(\nu)$ in Equation (52) was estimated by Hencky's model.[35,72,183,193] Similar adhesion energies of 0.31 J m^{-2} = 19 meV $Å^{-2}$ were found by the same authors in ref. [170]. The same approach was also employed by the same authors for MoS_2 blisters on SiO_x substrates,[35] and an adhesion energy $\gamma = (0.220 \pm 0.035)$ J m^{-2} = (14 ± 2) meV $Å^{-2}$ was estimated. The adhesion energies estimated with this method for several 2D material/substrate combinations are collected in Table 3.

By plugging $R = R_0$ into Equation (52), it is possible to calculate the critical pressure:[35,193]

$$p_{cr} = \frac{V_0 + V_b(R=R_0)}{V_0}\left(\frac{4\gamma}{5C(\nu)h_0(R=R_0)} + p_{ext}\right) \tag{53}$$

A comparison between the experimental and analytical data concerning the blister height h_0, the radius R, and the internal pressure p_{int} in graphene-based devices as a function of the input pressure p_0 is shown in Figure 21d. Three curves corresponding to slightly different values of the adhesion energy γ are shown in comparison to the experimental data in the delamination regime.

Indeed, this discussion shows how, from the study of the morphology of blisters as a function of the input pressure, it is possible to obtain precious information on the 2D material/substrate adhesion.

To conclude, it should be noticed that Equation (42) holds not only for the bubbles but also for the blisters. In fact, the only difference in modeling the equilibrium shape between bubbles and blisters is in the adhesion energy contribution, which has to be properly rescaled keeping into account the different contact area ($R^2 \to (R^2 - R_0^2)$), see Equations (41) and (51). However, the partial derivatives of U_{adh} with respect to h_0 and R are indeed unaffected by this change, so that the pressure Equation (42)

and the adhesion energy Equation (45) hold equivalently both for bubbles and delaminated blisters. Remarkably, in the blister case, the pressure is known experimentally, and therefore the blisters represent excellent platforms to measure the adhesion energy and the elastic modulus of the 2D membrane independently, instead of taking the latter from nanoindentation measurements.[35]

As a final remark, it's worth mentioning that the blisters, besides being excellent platforms to probe the elastic and adhesive properties of 2D materials, were also exploited to study friction. In particular, Zhang et al.[88] performed friction measurements at the center of graphene blisters subjected to small strains and on graphene deposited onto SiO_2 (referred to as supported graphene). **Figure 22**a shows the mean friction vs. normal load curves for both supported and suspended graphene samples. The corresponding coefficients of friction are displayed in panel (b).

Interestingly, supported graphene is known to be loosely bonded with intrinsic ripples, and in fact it shows remarkably larger friction. The friction of suspended graphene, which is lower to begin with, further decreases with increasing tensile strain, gradually leveling off at high strains. The coefficient of friction of graphene with 0.37% tensile strain is only 0.0013, which is in the regime of superlubricity. This shows how the blisters also allow one to tune friction in 2D materials.

4.4. Wrinkles: Energy Minimization

A similar approach to that developed for bubbles and blisters—based on the minimization of the total energy—was developed also for wrinkles. Interestingly, while the elastic properties of the material can be deduced by the collective study of an ensemble of wrinkles (namely, by studying their periodicity, see Section 3.3), the adhesive properties of the material can be deduced through the characterization of single, isolated wrinkles.[197] The mechanics of wrinkles was investigated by Vandeparre et al., who nicely showed how the same formalism can be applied from scales ranging from tens-of-nanometers for graphene sheets to meters for ordinary tissue curtains.[198] Deng et al. later employed the same formalism to show how it is possible to derive the adhesion energy from the knowledge of the wrinkles morphology.[197] Indeed, the shape of the wrinkle can be described through Equation (2) (see Figure 3e), h_0 and λ being the height and width of the wrinkle. Similarly to bubbles and blisters, in the most general case the total energy of the system can be written as:

$$U_{tot} = U_{stretch} + U_{bend} + U_{adh} \tag{54}$$

These energy contributions can be explicitly expressed as:[197,198]

$$U_{stretch} = \frac{1}{2} E_{2D} \left(\frac{\pi^2 h_0^2}{4\lambda} - L|\Delta|^2 \right) \tag{55}$$

$$U_{bend} = \frac{\pi^4 E_{2D} t^2 h_0^2}{12\lambda^3} \tag{56}$$

$$U_{adh} = \gamma(\lambda - L) \tag{57}$$

Here L is the lateral size of the wrinkled flake (in the direction perpendicular to the wrinkle) and $\Delta = (L - L_0)/L$, where L_0 is the size the flake would have in the absence of the wrinkle. Δ thus represents the plane strain. Interestingly, while in bubbles and blisters the mechanics of the system is dominated by the stretching term, and the bending term is negligible, the opposite happens in the case of wrinkles.[197] The stretching term can be therefore neglected, and the total energy reads:

$$U_{tot} = \frac{\pi^4 E_{2D} t^2 h_0^2}{12\lambda^3} + \gamma(\lambda - L) \tag{58}$$

By minimizing it with respect to h_0 and λ, one gets:

$$h_0 = \sqrt{|\Delta| \frac{L}{\lambda} - \frac{\pi^2 t^2 L}{3\lambda^3}}, \quad \frac{\pi^2 t^3}{3\lambda^3} \left(\frac{\pi^2 t^2}{3\lambda^2} - |\Delta| \right) + \frac{\gamma t}{2E_{2D} L} = 0 \tag{59}$$

Under the assumption that $|\Delta| \gg \pi^2 t^2 \lambda^{-2}/3$, the two expressions above give the following expression for the adhesion energy γ:

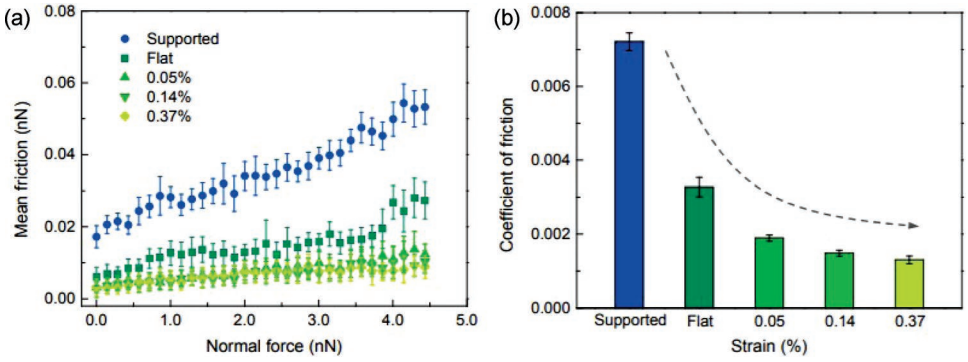

Figure 22. a) Friction versus normal force data measured on the supported graphene (i.e., graphene on a SiO_2 substrate) and suspended graphene blisters. The error bar represents the standard deviation of the repeated measurements under the same normal load. b) Variation of the coefficients of friction of graphene with strain, acquired by fitting linearly the mean friction vs. normal force curves in panel (a). Reproduced with permission.[88] Copyright 2019, National Academy of Sciences.

$$\gamma = \frac{\pi^4 E_{2D} t^2 h_0^2}{6\lambda^4} \tag{60}$$

This shows how to estimate the adhesion energy between a 2D material and a substrate by simply characterizing the height h_0 and width λ of the wrinkles. This approach was used by Deng et al., for MoS_2 flakes on several substrates.[197] For MoS_2 on SiO_2, the authors found an adhesion energy very close to that estimated using blisters by Lloyd et al. (see Table 3) which validates the use of this approach for the estimation of γ.

5. Nanomechanical Resonators and Other Applications

Nano-electromechanical systems (NEMS) are resonator devices able to transduce—and, thus, measure—signals from different physical environments by exploiting their effects on the vibrational modes of the resonator. The quantities that can be measured by NEMS devices include mechanical (e.g., mass, pressure, acceleration), chemical (e.g., gas composition), optical and biological parameters.[199] Within this context, 2D materials are excellent candidates for sensor applications, due to their large surface-to-volume ratio and unique electrical, mechanical, and optical properties. Moreover, the possibility to freely suspend 2D materials to form atomically thin membranes isolated from the substrate has further extended the potential of 2D materials for the fabrication of NEMS devices.[16] Pioneering studies on graphene-based NEMS soon demonstrated the high potential of 2D-based NEMS by reporting, for example, mass detection down to the hydrogen atom limit.[200,201] A critical parameter for a resonator device is the quality factor (Q), namely a dimensionless quantity defined as the ratio of the peak energy stored in a cycle of oscillation to the energy lost per cycle.[165] By definition, a less damped resonator has an intrinsically higher Q, which results in a large resonance peak ideal for NEMS implementations; having a high-quality factor is, indeed, imperative for taking reliable measurements with minimal noise. In a working device, the quality factor depends on a number of correlated factors, among which the material parameters, the working environment, and the device design; and generally it significantly increases as much as the device is isolated from the environment (i.e., kept in vacuum) or cooled down as close as possible to its fundamental quantum state (which is not usually viable for practical devices). Nowadays, the quality factors of 2D-based NEMS are generally lower than what is obtained by conventional semiconductors (i.e., silicon, silicon nitride, or quartz) NEMS.[202] On the other hand, silicon, the most conventional NEMS material, can only withstand small amounts of strain (on the order of 1–2%),[203] while 2D materials such as graphene,[3] BN,[4] and TMDs[5,6] have shown the ability to withstand strains in excess of 10%. Moreover, it was reported that the application of a tensile stress leads to a significant increase in the quality factors and mode frequencies of a mechanical resonator;[204] therefore—and in conjunction with their large Young's modulus and small atomic mass and with their peculiar electronic, optical, and thermal properties—2D materials are prime candidates for the fabrication of next-generation NEMS devices. In particular, being direct band-gap semiconductors, when reduced to the ML limit, TMDs are the natural choice for the observation (and practical exploitation) of electro- and opto-mechanical coupling phenomena.[205] For all these reasons, NEMS based on suspended 2D materials—and on TMDs in particular—have attracted a lot of interest and already demonstrated appealing characteristics for many different applications[159,166,199,202,206] as well as for fundamental physical problem investigations.[207,208] The main objective of a NEMS resonator is to detect small forces by measuring a resonator displacement. The force sensitivity of a NEMS resonator (δF), namely the minimal detectable force it can measure at resonance, is proportional to the square root of its effective mass (M_{eff}) and to the inverse of the square root of its quality factor (Q):

$$\delta F = \sqrt{\frac{8\pi M_{\text{eff}} f_n k_B T_{\text{res}}}{Q}} \tag{61}$$

where f_n is the mode frequency (in Hz), T_{res} is the resonator temperature, and k_B is Boltzmann's constant. The displacement sensitivity at resonance, on the other hand, is equal to

$$S_z^{\frac{1}{2}} = \sqrt{\frac{4k_B T_{\text{res}} Q}{(2\pi f_n)^3 M_{\text{eff}}}} \tag{62}$$

The displacement sensitivity of several MoS_2-based NEMS resonators was investigated by Lee et al. in the few-layer thickness range (6–68 nm).[166] A quality factor higher than 700 was reported at a frequency of about 20 MHz, for a residual pressure p = 6 mTorr, and for a circular membrane resonator with a diameter of about 6 µm; see **Figure 23**a. Given that $S_z^{\frac{1}{2}}$ improves (i.e., it gets smaller) for increasing mode frequency (see Equation (62)), it is interesting to note that the latter gets generally higher for smaller resonators. For circular suspended devices with diameter d, indeed, the frequency of the fundamental mode (f_0) is:[149,159,209]

$$f_0 = \sqrt{\left(\frac{2.4048}{\pi d}\right)^2 \frac{T}{\rho t} + \left(\frac{10.21t}{\pi d^2}\right)^2 \frac{E_{2D}}{3\rho(1-\nu^2)}} \tag{63}$$

where ρ is the mass density of the 2D membrane, T is pretension, and t is the membrane thickness. This equation effectively highlights the transition faced by circular resonators as a function of their thickness. Indeed, for relatively thick resonators, the system behaves as a simply supported circular plate (plate limit), with fundamental resonance frequency $f_0 = \frac{10.21t}{\pi d^2}\sqrt{\frac{E_{2D}}{3\rho(1-\nu^2)}}$. In this limit, the dependence of f_0 on the elastic properties of the material (E_{2D} and ν) is apparent. In the low-thickness regime, on the other hand, circular resonators reach the so-called membrane limit, for which f_0 tends to $\frac{2.4048}{\pi d}\sqrt{\frac{T}{\rho t}}$. In this regime, wherein all resonators based on TMD monolayers lie, the device behavior is dominated by the initial pre-tension, T; see Figure 23b. MoS_2 NEMS have shown the ability to sustain thermomechanical resonances even in ambient air; however, under this condition the quality factors drop to values on the order of ≈10, by following a power law of $Q \propto p^{-1/2}$ in the range of $p \sim$ 1–100 Torr, and then $Q \propto p^{-1}$ in the

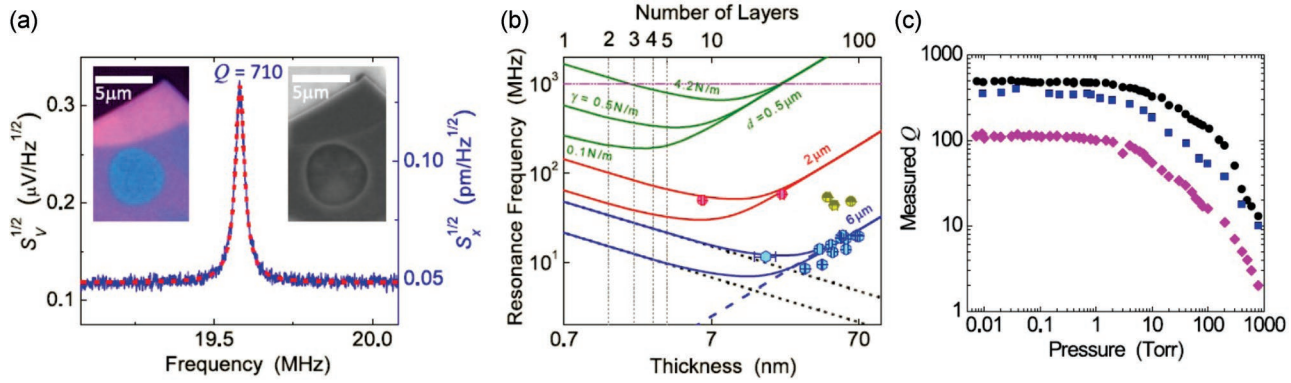

Figure 23. a) Displacement resonance of a NEMS device obtained by suspending a MoS_2 flake on a substrate patterned with micrometer-sized holes. Insets: Optical (right) and SEM (left) images of the device. b) Resonance frequency dependence on flake thickness (bottom axis) and number of layers (top axis) showing the transition between membrane and plate behavior for a circular resonator similar to that in panel (a). c) Dependence of the resonator quality factor as a function of the operation pressure measured on three different devices similar to that in panel (a). a–c) Reproduced with permission.[166] Copyright 2013, American Chemical Society.

range of $p \sim 100$–1000 Torr; see Figure 23c. Such an air damping phenomenon reported for 2D-based resonators is similar to the Q vs. p dependence measured in other membrane-structured MEMS/NEMS resonators.[210]

2D NEMS resonators based on MoS_2 membranes have been pushed down to the monolayer limit, reporting quality factors (≈50 at ambient air) of the same order as those reported for multilayer resonators,[159,166] frequency operation up to ≈120 MHz, and remarkably broad dynamic range (DR) up to more than 70 dB.[16] In particular, Castellanos-Gomez et al.[159] used a photothermal excitation technique to drive a monolayer MoS_2 NEMS resonator, first enabling to drive the resonator beyond the regime of harmonic oscillations, thus disclosing a nonlinear response regime of the device; see **Figure 24**. As a device resonates, the resulting large vibration amplitudes compared to the thickness of the device itself, result in an increased radial in-plane tension (in the case of a circular resonator), causing the frequency response of the device to extend beyond the linear regime.[211] Nonlinear resonators are normally described by a Duffing equation, obtained by solving the displacement x for a driven resonator, $M_{\text{eff}}\ddot{x} + (M_{\text{eff}} 2\pi f_{\text{n}}/Q)\dot{x} + k_1 x + k_3 x^3 = F_{\text{ext}}$, where $k_1 = M_{\text{eff}}(2\pi f_{\text{n}})^2$ is a linear damping term, k_3/k_1 represent the degree of cubic nonlinearity, and F_{ext} is the driving force.[212] Duffing nonlinearity well explains the nonlinear resonance behavior displayed in Figures 24c and 24e. Such a nonlinear behavior is characteristic of nanoresonators where the vibration displacement becomes comparable to the device thickness. For instance, in Figure 24c the membrane displacement is estimated to be on the order of 0.2 nm at the onset of the nonlinear regime. This regime has important implications for increasing the detector sensitivity, dynamical range, and for application as parametric sensing;[213] therefore several groups investigated the nonlinear regime in the last years demonstrating that 2D-based NEMS devices can exhibit strong nonlinear effects that can significantly affect the performance of the device.[214–217]

A detailed study on the dynamical range of MoS_2 resonators composed of mono- and few-layer membranes was performed by Lee et al.;[16] see **Figure 25**. Beyond the onset of Duffing nonlinearity, operations deep in the nonlinear regime are especially intriguing because MoS_2 atomic layers are greatly stretchable with ultrahigh strain limits.[32,185,218] Accordingly, on top of the linear regime dynamical range (DR_{linear}) it is possible to define a dynamic range of nonlinear operations ($DR_{\text{nonlinear}}$), namely the response dynamic from the onset of Duffing non-linearity to the maximum achievable deflection before the fracture limit (red regions in Figure 25b). Data taken on MoS_2 NEMS resonators show an extremely high DR_{linear} of ≈70 dB plus a $DR_{\text{nonlinear}}$ of ≈ 30 to 50 dB, thus demonstrating that 2D MEMS can reach dynamic ranges comparable to those obtained in top-down nanomachined structures (from conventional 3D crystals) that have much larger device volumes and much narrower frequency tunability.

Frequency tunability is, indeed, a desirable characteristic of a NEMS resonator and large tunability has been reported on 2D-based NEMS resonators. In the last years, different mechanisms have been investigated to tune the natural frequency of a 2D-based NEMS resonator, such as gamma radiation exposure or temperature. Gamma ray exposure turns out to be extremely powerful in the case of MoS_2 resonators, thus being of potential use as radiation detection devices.[219] On the other hand, the temperature can be a relevant parameter, as for example in graphene-based NEMS whose response is highly dependent on the number of layers[220] and that feature a frequency shift of more than 300% in the case of three-layer graphene; see **Figures 26**a–b. Alternatively, bending and bias gating were used to tune the resonance frequency in 2D-based NEMS, but generally the quality factor was reported to deteriorate following the frequency shift,[16] thus reducing the sensitivity of the device. Recently, besides the gate-tunability, an exciton-mechanical coupling was also demonstrated, which allowed for a dynamic control of the resonance frequency of the NEMS resonator.[205] A sketch of such a kind of device is given in Figure 26c. A silicon back gate can induce charges in a $MoSe_2$ membrane and pull it down, thus breaking the mirror symmetry of the mechanical device. Mechanical vibration of the membrane then creates an oscillating strain in the sample, which in turn produces a dynamical spectral shift in the exciton resonance due to the linear strain dependence of the exciton resonance energy;[221,222] see Figure 26d. As a result, illumination of the sample with light near the exciton resonance can generate a radiation force

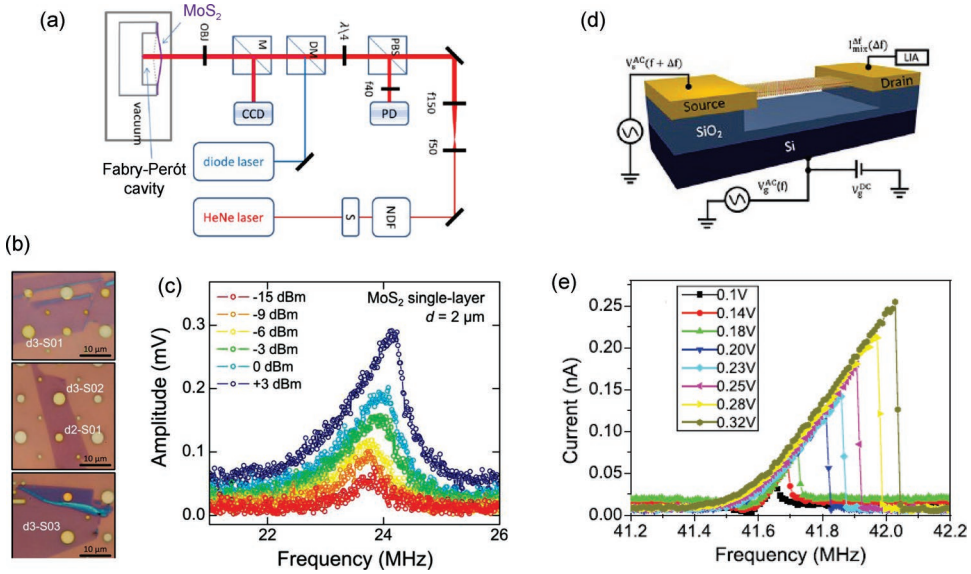

Figure 24. a) Optical interferometer setup used to measure the vibration of a MoS_2 NEMS kept in a vacuum changer and driven by photothermal excitation. b) Optical microscopy images of single-layer MoS_2 flakes transferred onto a pre-patterned substrate with holes of different diameter. c) Nonlinear response of a monolayer MoS_2 resonator. The frequency response measured for a 2 μm diameter monolayer NEMS resonator clearly shows a deviation from a harmonic response for increasing the optical excitation power above –9 dBm, thus indicating that the resonator is oscillating in the nonlinear regime. The membrane displacement is estimated to be on the order of 0.2 nm when clear signatures of a nonlinear response occur (blue line, driven at +3 dBm). a–c) Adapted or reproduced with permission.[159] Copyright 2013, Wiley-VCH. d) Schematic representation of a MoS_2 suspended resonator and of the electrical measurement setup to drive it. Reproduced with permission.[216] Copyright 2018, American Institute of Physics. e) Typical frequency response of the device shown in panel (d) driven at moderate bias and showing a strong nonlinear behaviour. Reproduced with permission.[215] Copyright 2015, American Institute of Physics.

with dynamical backaction,[223–225] producing exciton-optomechanical effects that opens the door for the dynamical control of mechanical motion through the exciton resonance of monolayer TMDs; see Figures 26e–f.

The same properties that make 2D materials so interesting for next generation NEMS devices—first of all, their inherent flexibility—make them also promising for innovative technological applications; such as wearable electronics (i.e., smart glasses, smartwatches, electronic tattoos),[226] flexible optoelectronics (i.e., flexible displays, flexible transistors),[227,228] or skin-mountable devices (i.e., touch, tactile, chemical, or biosignal sensors, displays, data transmission devices).[226] Such applications ideally require large-area nano-manufacturing of devices

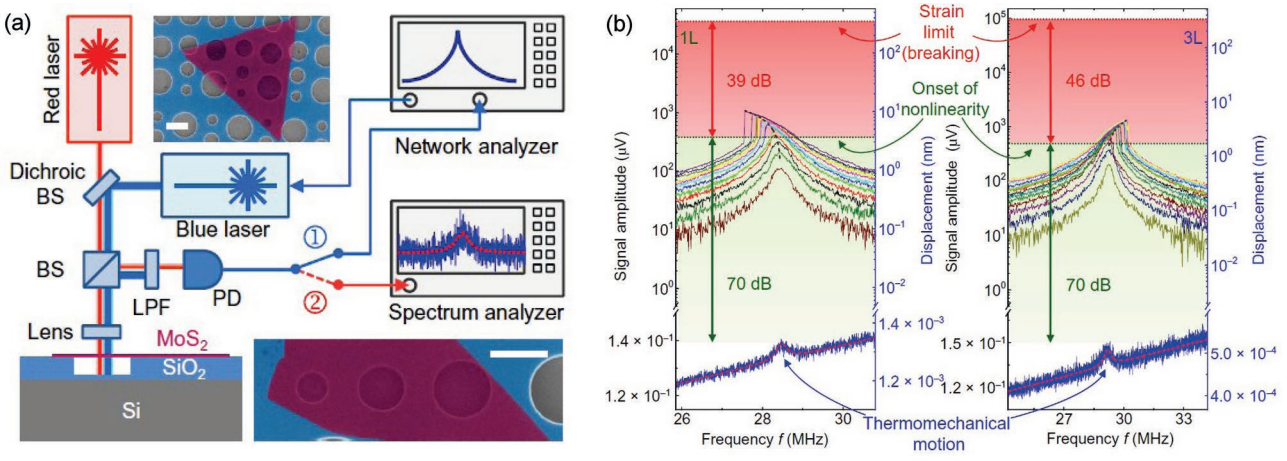

Figure 25. a) Schematic representation of an experimental setup to drive and measure a NEMS resonator obtained by suspending a MoS_2 flake on a substrate patterned with micrometer-size holes. A 633 nm red laser is used to probe both the natural thermomechanical vibrations of the device and the driven vibrations excited by a 405 nm blue laser. Images are SEM scans of arrays of single- (upper inset) and few-layer (lower inset) MoS_2 resonators. Scale bar of 1 μm. b) Dynamic range (DR) of a monolayer (left) and three-layer (right) MoS_2 resonator with a diameter of 1.5 μm for increasing driving amplitude. The DR for linear operation (green zone) is determined by the measurement of its lowest detectable value and the onset of nonlinearity. The DR for nonlinear operation (red zone) is limited by the fracture strength of the material. Reproduced with permission.[16] Copyright 2018, published by American Association for the Advancement of Science.

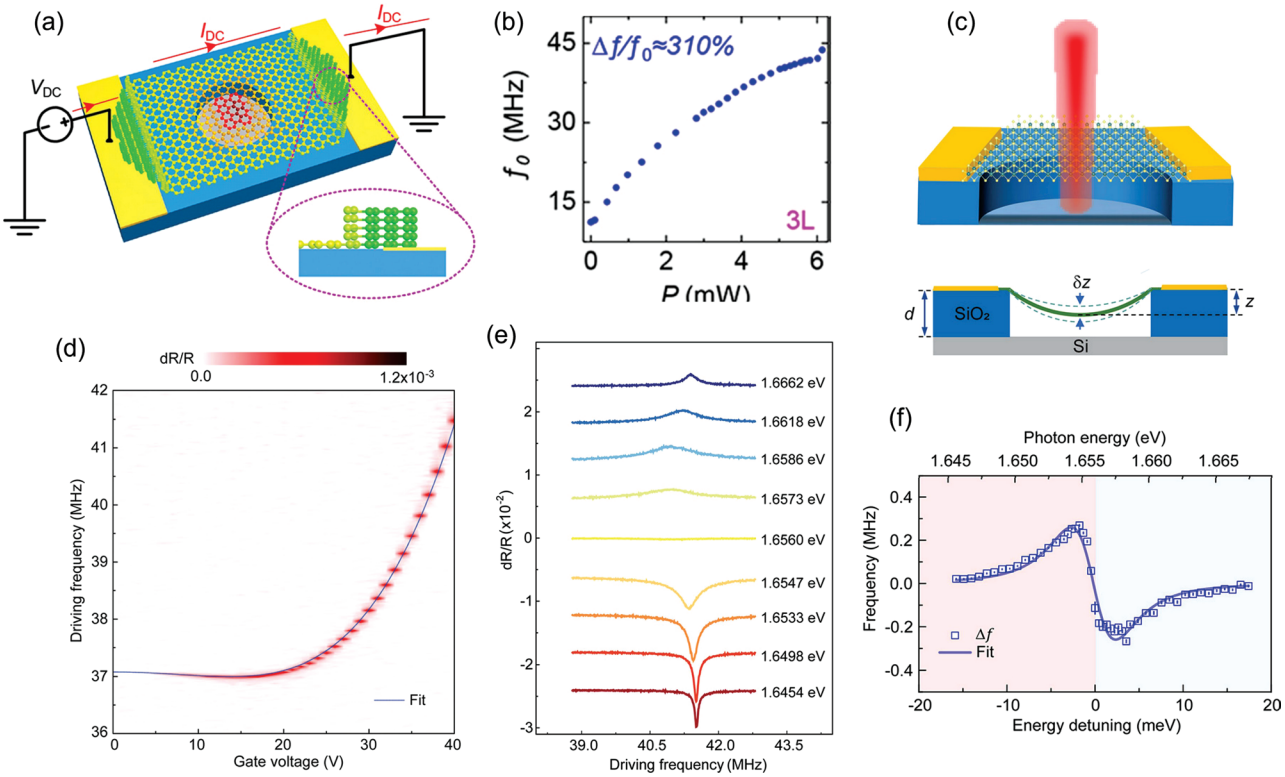

Figure 26. a) Illustration of a circular drumhead graphene resonator with Joule heating. The color of graphene bonds and atoms indicates the temperature gradient and profile (green and red colors represent low and high temperature of graphene, respectively). Inset: zoom-in view of graphene-graphite-metal contact region. b) Frequency of the resonator measured on a device as that shown in panel (a) in the case of three-layer graphene membrane. A shift of the natural frequency mode up to 310% is observed with increasing the heating power. a,b) Reproduced with permission.[220] Copyright 2018, American Chemical Society. c) Schematic illustration of a suspended monolayer $MoSe_2$ contacted by gold electrodes and illuminated by a laser beam. *z* represents the static vertical displacement of the membrane induced by a DC gate voltage and δz is the vibration amplitude induced by an AC gate voltage, which induces a dynamical shift in the exciton resonance and gives rise to dynamical back-action. d) Gate voltage dependence of the mechanical resonance frequency. e) Fractional change in reflection contrast as a function of the AC driving frequency at different probe photon energies near the exciton resonance (incident power ≈ 10 μW). The curves are vertically displaced for clarity purpose. Near-zero change is seen at the excitonic resonance. f) Relative resonance shift extracted from panel (e) as a function of the energy detuning (bottom axis) and incident photon energy (top axis). The blue- and red-shaded regions correspond to blue and red energy detuning, respectively. c–f) Reproduced with permission.[205] Copyright 2021, American Chemical Society.

based on ultra-thin functional materials—eventually transparent, energy efficient, and that can afford radio-frequency (RF) wireless connectivity—on a soft polymeric or plastic substrate. Indeed, their realization would lead to a new era of integrated flexible technology that can be manufactured at economically viable scales. Detailed reviews of applications based on flexible 2D materials are given in some papers that recently appeared in the literature.[228–232] In the following, we briefly review some of those applications where the mechanical and optical properties of the employed materials (i.e., TMDs) enable new opportunities. As a first example, TMDs have been found to be among the most promising 2D materials for skin-mountable electronics because of their high flexibility, robustness, and moderate bandgap energy (in the range of 1.1–2.5 eV), which provides unique optical and electrical property combinations that are hardly found even in the archetypal 2D material, graphene.[229] Moreover, good biocompatibility and chemical stability enable the direct integration of these 2D materials with the human body for sensing biochemical and physiological information, and healthcare applications.[226] Ideal materials for skin-mountable devices need to have a high flexibility—besides an accurate mechanical design of the device itself—to be fabricated and operated on unusual substrates like skin, as well as for achieving good sensing capabilities and stable device operation under high-strain conditions. Among all TMDs, MoS_2 is considered to be one of the most promising materials due to its extraordinary physicochemical properties, large abundance in nature as molybdenite, and controlled synthesis. Taking advantage of the relatively large (1.8 eV for ML and 1.2 eV for bulk) and strain-tunable bandgap properties, multilayer MoS_2 could endow transistors with a high field-effect mobility (≈140 $cm^2\ V^{-1}\ s^{-1}$) and an excellent performance stability even after thousand cycles of bending process.[233] Furthermore, the modulation in the bandgap and charge distribution by strain allows MoS_2-based strain gauges with a >200 gauge factor GF (defined as $\left[\frac{q(\varepsilon)-q(0)}{q(0)}\right]/\Delta\varepsilon$, where *q* is a strain sensitive measurable quantity, e.g., the current flowing in a piezoelectric device subjected to strain).[7] In particular, by virtue of the large piezoresistivity and ultrathin thickness of bilayer MoS_2, tactile sensors could achieve conformal contact with the skin, keeping high gauge factors (>70).[234]

Another paradigmatic example is the case of flexible, thin-film transistors (TFTs). In recent years, many different strategies have been developed to get flexible TFTs. Typically, low speed flexible electronics is based on organic or low temperature deposition-compatible amorphous semiconductors or metal oxide materials. On the other hand, RF capable flexible transistors, due to their wider signal handling capability, can extend flexible electronics applications toward wireless data transmission and wireless power transfer, or allow circuits to operate with much lower power consumption. The main challenges in the pursuit of RF flexible electronics included a lack of materials with sufficient mobility and simultaneous mechanical flexibility and difficulties in defining a small channel region using a scalable fabrication process. Some solutions have been developed to overcome these challenges with conventional semiconductors. For example, a flexible single crystalline semiconductor nanomembrane-based TFT was shown to operate at 100 GHz.[235] 2D materials have rapidly gained room in the field of TFTs, with graphene-based field-effect transistors (GFETs) being routinely commercialized today, after almost a decade-long period of research since the first prototype.[236] Also in this field, TMDs have recently shown some promising perspectives due to their unique combination of mechanical, transport, and optical properties. A finite bandgap is, indeed, a critical ingredient for building semiconductor devices, and although techniques to introduce a bandgap into graphene are possible (e.g., shaping it into nanoribbons,[237] applying a vertical electrical field[238] or by hydrogen irradiation[239]), they are all proved to be challenging. In a recent paper,[230] Kis recounts how the first transistor based on a single layer of MoS_2 was created, featuring room-temperature mobility (>200 $cm^2\ V^{-1}\ s^{-1}$) similar to that of graphene nanoribbons, room-temperature current on/off ratios of 1×10^8, and ultralow standby power dissipation. Since MoS_2 has a direct bandgap in the ML limit, it can also be used to construct interband tunnel FETs, which offer lower power consumption than classical transistors. MoS_2 MLs could also complement graphene in applications that require thin transparent semiconductors, such as in optoelectronics and energy harvesting. Moreover, MoS_2-MLs-based TFTs were successfully fabricated on flexible substrates, too,[233] thus indicating that a new era of flexible technology, mainly based on TMDs, is already developing.

6. Conclusions and Perspectives

In this review, we discussed the working principles of various experimental techniques employed to address the elasto-mechanical and adhesive properties of 2D crystals. We related each technique with the specific physical quantity to determine, thus providing a guidance for the choice of the most suitable experiment to perform. As a matter of fact, 2D materials offer a wealth of methods, such as indenting and bulging and their manifold variants, which enable a mechanical sampling of the material's elastic properties. The inherent surface nature of 2D crystals makes them a rich playground, wherein to explore and exploit their high sensitivity to external perturbations with great prospects for mass sensors and electro-mechanical transducers. In addition, the experimental characterization of 2D materials at the nanoscale, for example by SPM techniques, offers also the opportunity to observe novel phenomena, like superlubricity[88] and superelasticity-like behaviors.[185] Further, we highlighted the importance of theoretical modeling and interpretation of the mechanical measurements in order to achieve a reliable determination of the mechanical, elastic, and adhesive properties of 2D crystals. In discussing different state-of-the-art methods to experimentally probe the Young's modulus and adhesion energy of 2D materials, we also provided a collection of the values reported in the literature for both these two fundamental quantities. Mechanical deformations appear especially appealing in the developing field of 2D heterostructures, where controlled strain application represents a means to induce novel and re-configurable electronic states.[134]

Finally, we discussed in detail the enormous potential of these materials as nanomechanical resonators, and in general for the realization of flexible electronic devices. As detailed above, the possibility of fabricating NEMS based on vanishingly thin—possibly down to the monolayer limit—strained TMD crystals can be highly beneficial to the device performances. As evidenced by Equations (61) and (62), indeed, smaller, lighter resonators are characterized by better force and displacement sensitivities. Within the framework of strain-engineered 2D crystals, on the other hand, very interesting prospects for the achievement of high-frequency (>100 MHz) operation are opened by the observation that in the low-thickness regime (the so-called membrane limit), the frequency of the fundamental mode of the nanoresonator is ruled by the initial pre-tension, i.e., by the amount of strain in the device [see Equation (63)]. Moreover, 2D materials are inherently flexible, can withstand very large strains (in excess of 10%), and—in the case of TMD MLs—have shown large piezoelectric responses.[7,8] This paves the way to the realization of high-performance, robust nanoscale electromechanical sensors and actuators[206] and powering nanodevices,[7] crucial for the development of the next generation of flexible, skin-mountable electronic applications.[229]

Acknowledgements

C.D.G. and E.B. contributed equally to the work.

Open Access Funding provided by Universita degli Studi di Roma La Sapienza within the CRUI-CARE Agreement.

Conflict of Interest

The authors declare no conflict of interest.

Keywords

adhesion properties of 2D materials, deformation of 2D materials, elasticity, strain, 2D materials, van der Waals materials, Young's modulus

Received: November 12, 2021
Revised: January 10, 2022
Published online: April 4, 2022

[1] M. Felici, S. Birindelli, R. Trotta, M. Francardi, A. Gerardino, A. Notargiacomo, S. Rubini, F. Martelli, M. Capizzi, A. Polimeni, *Phys. Rev. Applied* **2014**, *2*, 064007.
[2] C. E. Murray, A. Ying, S. M. Polvino, I. C. Noyan, M. Holt, J. Maser, *J. Appl. Phys.* **2011**, *109*, 083543.
[3] C. Lee, X. Wei, J. W. Kysar, J. Hone, *Science* **2008**, *321*, 385.
[4] A. Falin, Q. Cai, E. J. Santos, D. Scullion, D. Qian, R. Zhang, Z. Yang, S. Huang, K. Watanabe, T. Taniguchi, M. R. Barnett, Y. Chen, R. S. Ruoff, L. H. Li, *Nat. Commun.* **2017**, *8*, 15815.
[5] C. Di Giorgio, E. Blundo, G. Pettinari, M. Felici, Y. Lu, A. M. Cucolo, A. Polimeni, F. Bobba, *Adv. Mater. Interfaces* **2020**, *7*, 2001024.
[6] E. Blundo, C. Di Giorgio, G. Pettinari, T. Yildirim, M. Felici, Y. Lu, F. Bobba, A. Polimeni, *Adv. Mater. Interfaces* **2020**, *7*, 2000621.
[7] W. Wu, L. Wang, Y. Li, F. Zhang, L. Lin, S. Niu, D. Chenet, X. Zhang, Y. Hao, T. F. Heinz, J. Hone, Z. L. Wang, *Nature* **2014**, *514*, 470.
[8] H. Zhu, Y. Wang, J. Xiao, M. Liu, S. Xiong, Z. J. Wong, Z. Ye, Y. Ye, X. Yin, X. Zhang, *Nat. Nanotechnol.* **2015**, *10*, 151.
[9] E. Blundo, M. Felici, T. Yildirim, G. Pettinari, D. Tedeschi, A. Miriametro, B. Liu, W. Ma, Y. Lu, A. Polimeni, *Phys. Rev. Res.* **2020**, *2*, 012024.
[10] A. Srivastava, M. Sidler, A. V. Allain, D. S. Lembke, A. Kis, A. Imamoğlu, *Nat. Nanotechnol.* **2015**, *10*, 491.
[11] M. Koperski, K. Nogajewski, A. Arora, V. Cherkez, P. Mallet, J. Y. Veuillen, J. Marcus, P. Kossacki, M. Potemski, *Nat. Nanotechnol.* **2015**, *10*, 503.
[12] T. T. Tran, K. Bray, M. J. Ford, M. Toth, I. Aharonovich, *Nat. Nanotechnol.* **2015**, *11*, 37.
[13] N. Levy, S. A. Burke, K. L. Meaker, M. Panlasigui, A. Zettl, F. Guinea, A. H. C. Neto, M. F. Crommie, *Science* **2010**, *329*, 544.
[14] A. Castellanos-Gomez, M. Buscema, R. Molenaar, V. Singh, L. Janssen, H. S. J. van der Zant, G. A. Steele, *2D Mater.* **2014**, *1*, 011002.
[15] J. S. Bunch, A. M. van der Zande, S. S. Verbridge, I. W. Frank, D. M. Tanenbaum, J. M. Parpia, H. G. Craighead, P. L. McEuen, *Science* **2007**, *315*, 490.
[16] J. Lee, Z. Wang, K. He, R. Yang, J. Shan, P. X.-L. Feng, *Sci. Adv.* **2018**, *4*, eaao6653.
[17] T. Zhang, X. Li, H. Gao, *Int. J. Fract.* **2015**, *196*, 1.
[18] Y. T. Megra, J. W. Suk, *J. Phys. D: Appl. Phys.* **2019**, *52*, 364002.
[19] K. K. Al-Quraishi, Q. He, W. Kauppila, M. Wang, Y. Yang, *Int. J. Smart Nano Mater.* **2020**, *11*, 207.
[20] X. Li, M. Sun, C. Shan, Q. Chen, X. Wei, *Adv. Mater. Interfaces* **2018**, *5*, 1701246.
[21] G. Cao, H. Gao, *Prog. Mater. Sci.* **2019**, *103*, 558.
[22] D. Akinwande, C. J. Brennan, J. S. Bunchm, P. Egberts, J. R. Felts, H. Gao, R. Huang, J.-S. Kim, T. Li, Y. Li, K. M. Liechti, N. Lu, H. S. Park, E. J. Reed, P. Wang, B. I. Yakobson, T. Zhang, Y.-W. Zhang, Y. Zhou, Y. Zhu, *Extreme Mech. Lett.* **2017**, *13*, 42.
[23] J. Choi, H. Kim, M. Wang, J. Leem, W. King, S. Nam, *Nano Lett.* **2015**, *15*, 4525.
[24] S. Kumar, A. Kaczmarczyk, B. D. Gerardot, *Nano Lett.* **2015**, *15*, 7567.
[25] A. Branny, S. Kumar, R. Proux, B. D. Gerardot, *Nat. Commun.* **2017**, *8*, 15053.
[26] Y. Luo, G. D. Shepard, J. V. Ardelean, D. A. Rhodes, B. Kim, K. Barmak, J. C. Hone, S. Strauf, *Nat. Nanotechnol.* **2018**, *13*, 1137.
[27] A. Reserbat-Plantey, D. Kalita, Z. Han, L. Ferlazzo, S. Autier-Laurent, K. Komatsu, C. Li, R. Weil, A. Ralko, L. Marty, S. Guéron, N. Bendiab, H. Bouchiat, V. Bouchiat, *Nano Lett.* **2014**, *14*, 5044.
[28] J. Kern, I. Niehues, P. Tonndorf, R. Schmidt, D. Wigger, R. Schneider, T. Stiehm, S. M. de Vasconcellos, D. E. Reiter, T. Kuhn, R. Bratschitsch, *Adv. Mater.* **2016**, *28*, 7101.
[29] T. Cai, S. Dutta, S. Aghaeimeibodi, Z. Yang, S. Nah, J. T. Fourkas, E. Waks, *Nano Lett.* **2017**, *17*, 6564.
[30] H. Li, A. W. Contryman, X. Qian, S. M. Ardakani, Y. Gong, X. Wang, J. M. Weisse, C. H. Lee, J. Zhao, P. M. Ajayan, J. Li, H. C. Manoharan, X. Zheng, *Nat. Commun.* **2015**, *6*, 7381.
[31] Y. K. Ryu, F. Carrascoso, R. López-Nebreda, N. Agraït, R. Frisenda, A. Castellanos-Gomez, *Nano Lett.* **2020**, *20*, 5339.
[32] S. Bertolazzi, J. Brivio, A. Kis, *ACS Nano* **2011**, *5*, 9703.
[33] S. Manzeli, A. Allain, A. Ghadimi, A. Kis, *Nano Lett.* **2015**, *15*, 5330.
[34] D. Lloyd, X. Liu, J. W. Christopher, L. Cantley, A. Wadehra, B. L. Kim, B. B. Goldberg, A. K. Swan, J. S. Bunch, *Nano Lett.* **2016**, *16*, 5836.
[35] D. Lloyd, X. Liu, N. Boddeti, L. Cantley, R. Long, M. L. Dunn, J. S. Bunch, *Nano Lett.* **2017**, *17*, 5329.
[36] G. Wang, Z. Dai, Y. Wang, P. Tan, L. Liu, Z. Xu, Y. Wei, R. Huang, Z. Zhang, *Phys. Rev. Lett.* **2017**, *119*, 036101.
[37] J. S. Bunch, S. S. Verbridge, J. S. Alden, A. M. van der Zande, J. M. Parpia, H. G. Craighead, P. L. McEuen, *Nano Lett.* **2008**, *8*, 2458.
[38] E. Khestanova, F. Guinea, L. Fumagalli, A. Geim, I. Grigorieva, *Nat. Commun.* **2016**, *7*, 12587.
[39] D. Tedeschi, E. Blundo, M. Felici, G. Pettinari, B. Liu, T. Yildrim, E. Petroni, C. Zhang, Y. Zhu, S. Sennato, Y. Lu, A. Polimeni, *Adv. Mater.* **2019**, *31*, 1903795.
[40] R. Hull, J. Bean, *Principles and Concepts of Strained-Layer Epitaxy*, Vol. *33*, Semiconductors and Semimetals, 1st Edition, Academic Press, San Diego **1990**.
[41] S. Mazzucato, D. Nardin, M. Capizzi, A. Polimeni, A. Frova, L. Seravalli, S. Franchi, *Mater. Sci. Eng. C* **2005**, *25*, 830.
[42] B. Li, C. Ji, W. Yang, J. Wang, K. Yang, R. Xu, W. Liu, Z. Cai, J. Chen, H. kwang Mao, *Proc. Natl. Acad. Sci. USA* **2018**, *115*, 1713.
[43] Y. S. Choi, T. Numata, T. Nishida, R. Harris, S. E. Thompson, *J. Appl. Phys.* **2008**, *103*, 064510.
[44] A. R. Goñi, K. Syassen, *Optical Properties of Semiconductors under Pressure*, Vol. *54*, Semiconductors and Semimetals, 1st Edition, Academic Press, San Diego **1998**.
[45] I. E. Itskevich, S. G. Lyapin, I. A. Troyan, P. C. Klipstein, L. Eaves, P. C. Main, M. Henini, *Phys. Rev. B* **1998**, *58*, R4250.
[46] G. Pettinari, A. Polimeni, F. Masia, R. Trotta, M. Felici, M. Capizzi, T. Niebling, W. Stolz, P. J. Klar, *Phys. Rev. Lett.* **2007**, *98*, 146402.
[47] X. Fu, C. Su, Q. Fu, X. Zhu, R. Zhu, C. Liu, Z. Liao, J. Xu, W. Guo, J. Feng, D. Yu, *Adv. Mater.* **2014**, *26*, 2572.
[48] J. C. Meyer, A. K. Geim, M. I. Katsnelson, K. S. Novoselov, T. J. Booth, S. Roth, *Nature* **2007**, *446*, 60.
[49] E. Stolyarova, K. T. Rim, S. Ryu, J. Maultzsch, P. Kim, L. E. Brus, T. F. Heinz, M. S. Hybertsen, G. W. Flynn, *Proc. Natl. Acad. Sci. USA* **2007**, *104*, 9209.
[50] M. Ishigami, J. H. Chen, W. G. Cullen, M. S. Fuhrer, E. D. Williams, *Nano Lett.* **2007**, *7*, 1643.
[51] T. J. Booth, P. Blake, R. R. Nair, D. Jiang, E. W. Hill, U. Bangert, A. Bleloch, M. Gass, K. S. Novoselov, M. I. Katsnelson, A. K. Geim, *Nano Lett.* **2008**, *8*, 2442.
[52] K. R. Knox, S. Wang, A. Morgante, D. Cvetko, A. Locatelli, T. O. Mentes, M. A. Nino, P. Kim, J. R. M. Osgood, *Phys. Rev. B* **2008**, *78*, 201408(R).
[53] U. Stoberl, U. Wurstbauer, W. Wegscheider, D. Weiss, J. Eroms, *Appl. Phys. Lett.* **2008**, *93*, 051906.
[54] V. Geringer, M. Liebmann, T. Echtermeyer, S. Runte, M. Schmidt, R. Rückamp, M. C. Lemme, M. Morgenstern, *Phys. Rev. Lett.* **2009**, *102*, 076102.
[55] A. Fasolino, J. H. Los, M. I. Katsnelson, *Nat. Mater.* **2007**, *6*, 858.
[56] C. H. Lui, L. Liu, K. F. Mak, G. W. Flynn, T. F. Heinz, *Nature* **2009**, *462*, 339.

[57] W. Zhu, T. Low, V. Perebeinos, A. A. Bol, Y. Zhu, H. Yan, J. Tersoff, P. Avouris, *Nano Lett.* **2012**, *12*, 3431.
[58] K. Kim, Z. Lee, B. D. Malone, K. T. Chan, B. Alemán, W. Regan, W. Gannett, M. F. Crommie, M. L. Cohen, A. Zettl, *Phys. Rev. B* **2011**, *83*, 245433.
[59] H. Hattab, A. T. N'Diaye, D. Wall, C. Klein, G. Jnawali, J. Coraux, C. Busse, R. van Gastel, B. Poelsema, T. Michely, F.-J. M. Zu Heringdorf, M. Horn- von Hoegen, *Nano Lett.* **2012**, *12*, 678.
[60] T. M. Paronyan, E. M. Pigos, G. Chen, A. R. Harutyunyan, *ACS Nano* **2011**, *5*, 9619.
[61] Y. Zhang, T. Gao, Y. Gao, S. Xie, Q. Ji, K. Yan, H. Peng, Z. Liu, *ACS Nano* **2011**, *5*, 4014.
[62] S. J. Chae, F. Güneş, K. K. Kim, E. S. Kim, G. H. Han, S. M. Kim, H.-J. Shin, S.-M. Yoon, J.-Y. Choi, M. H. Park, C. W. Yang, D. Pribat, Y. H. Lee, *Adv. Mater.* **2009**, *21*, 2328.
[63] X. Duan, C. Wang, J. C. Shaw, R. Cheng, Y. Chen, H. Li, X. Wu, Y. Tang, Q. Zhang, A. Pan, J. Jiang, R. Yu, Y. Huang, X. Duan, *Nat. Nanotechnol.* **2014**, *9*, 1024.
[64] Y. Gong, J. Lin, X. Wang, G. Shi, S. Lei, Z. Lin, X. Zou, G. Ye, R. Vajtai, B. I. Yakobson, H. Terrones, M. Terrones, B. K. Tay, J. Lou, S. T. Pantelides, Z. Liu, W. Zhou, P. M. Ajayan, *Nat. Mater.* **2014**, *13*, 1135.
[65] K. Bogaert, S. Liu, J. Chesin, D. Titow, S. Gradečak, S. Garaj, *Nano Lett.* **2016**, *16*, 5129.
[66] Y. Gong, S. Lei, G. Ye, B. Li, Y. He, K. Keyshar, X. Zhang, Q. Wang, J. Lou, Z. Liu, R. Vajtai, W. Zhou, P. M. Ajayan, *Nano Lett.* **2015**, *15*, 6135.
[67] F. Ullah, Y. Sim, C. T. Le, M.-J. Seong, J. I. Jang, S. H. Rhim, B. C. Tran Khac, K.-H. Chung, K. Park, Y. Lee, K. Kim, H. Y. Jeong, Y. S. Kim, *ACS Nano* **2017**, *11*, 8822.
[68] S. Xie, L. Tu, Y. Han, L. Huang, K. Kang, K. U. Lao, P. Poddar, C. Park, D. A. Muller, R. A. D. Jr, J. Park, *Science* **2018**, *359*, 1131.
[69] T. Georgiou, L. Britnell, P. Blake, R. V. Gorbachev, A. Gholinia, A. K. Geim, C. Casiraghi, K. S. Novoselov, *Appl. Phys. Lett.* **2011**, *99*, 093103.
[70] D. A. Sanchez, Z. Dai, P. Wang, A. Cantu-Chavez, C. J. Brennan, R. Huang, N. Lu, *Proc. Natl. Acad. Sci. USA* **2018**, *115*, 7884.
[71] Z. Dai, Y. Hou, D. A. Sanchez, G. Wang, C. J. Brennan, Z. Zhang, L. Liu, N. Lu, *Phys. Rev. Lett.* **2018**, *121*, 266101.
[72] E. Blundo, T. Yildirim, G. Pettinari, A. Polimeni, *Phys. Rev. Lett.* **2021**, *127*, 046101.
[73] A. V. Kretinin, Y. Cao, J. S. Tu, G. L. Yu, R. Jalil, K. S. Novoselov, S. J. Haigh, A. Gholinia, A. Mishchenko, M. Lozada-Hidalgo, T. Georgiou, C. R. Woods, F. Withers, P. Blake, G. Eda, A. Wirsig, C. Hucho, K. Watanabe, T. Taniguchi, A. K. Geim, R. V. Gorbachev, *Nano Lett.* **2014**, *14*, 3270.
[74] G. H. Ahn, M. Amani, H. Rasool, D.-H. Lien, J. P. Mastandrea, J. W. A. III, M. Dubey, D. C. Chrzan, A. M. Minor, A. Javey, *Nat. Commun.* **2017**, *8*, 608.
[75] Y. Sun, J. Pan, Z. Zhang, K. Zhang, J. Liang, W. Wang, Z. Yuan, Y. Hao, B. Wang, J. Wang, Y. Wu, J. Zheng, L. Jiao, S. Zhou, K. Liu, C. Cheng, W. Duan, Y. Xu, Q. Yan, K. Liu, *Nano Lett.* **2019**, *19*, 761.
[76] K. Liu, J. Wu, *J. Mater. Res.* **2015**, *31*, 832.
[77] H. Moon, G. Grosso, C. Chakraborty, C. Peng, T. Taniguchi, K. Watanabe, D. Englund, *Nano Lett.* **2020**, *20*, 6791.
[78] J. Tao, W. Shen, S. Wu, L. Liu, Z. Feng, C. Wang, C. Hu, P. Yao, H. Zhang, W. Pang, X. Duan, J. Liu, C. Zhou, D. Zhang, *ACS Nano* **2015**, *11*, 11362.
[79] F. A. Benimetskiy, V. A. Sharov, P. A. Alekseev, V. Kravtsov, K. B. Agapev, I. S. Sinev, I. S. Mukhin, A. Catanzaro, R. G. Polozkov, E. M. Alexeev, A. I. Tartakovskii, A. K. Samusev, M. S. Skolnick, D. N. Krizhanovskii, I. A. Shelykh, I. V. Iorsh, *APL Mater.* **2019**, *7*, 101126.
[80] M. G. Harats, J. N. Kirchhof, M. Qiao, K. Greben, K. I. Bolotin, *Nat. Photon.* **2020**, *14*, 234.
[81] X. Liu, A. K. Sachan, S. T. Howell, A. Conde-Rubio, A. W. Knoll, G. Boero, R. Zenobi, J. Brugger, *Nano Lett.* **2020**, *20*, 8250.
[82] M. R. Rosenberger, C. K. Dass, H.-J. Chuang, S. V. Sivaram, K. M. McCreary, J. R. Hendrickson, B. T. Jonker, *ACS Nano* **2019**, *13*, 904.
[83] D. Vella, J. Bico, A. Boudaoud, B. Roman, P. M. Reis, *Proc. Natl. Acad. Sci. USA* **2009**, *106*, 10901.
[84] C. M. Stafford, C. Harrison, K. L. Beers, A. Karim, E. J. Amis, M. R. VanLandingham, H.-C. Kim, W. Volksen, R. D. Miller, E. E. Simonyi, *Nat. Mater.* **2004**, *3*, 545.
[85] K. P. Dhakal, S. Roy, H. Jang, X. Chen, W. S. Yun, H. Kim, J. Lee, J. Kim, J.-H. Ahn, *Chem. Mater.* **2017**, *29*, 5124.
[86] A. Castellanos-Gomez, R. Roldán, E. Cappelluti, M. Buscema, F. Guinea, H. S. J. van der Zant, G. A. Steele, *Nano Lett.* **2013**, *13*, 5361.
[87] J. Lee, S. J. Yun, C. Seo, K. Cho, T. S. Kim, G. H. An, K. Kang, H. S. Lee, J. Kim, *Nano Lett.* **2021**, *21*, 43.
[88] S. Zhang, Y. Hou, S. Lie, L. Liu, Z. Zhang, X.-Q. Feng, Q. Li, *Proc. Natl. Acad. Sci. USA* **2019**, *116*, 24452.
[89] S. P. Koenig, L. Wang, J. Pellegrino, J. S. Bunch, *Nat. Nanotechnol.* **2012**, *7*, 728.
[90] E. Blundo, E. Cappelluti, M. Felici, G. Pettinari, A. Polimeni, *Appl. Phys. Rev.* **2021**, *8*, 021318.
[91] J. Lu, A. C. Neto, K. P. Loh, *Nat. Commun.* **2012**, *3*, 823.
[92] E. Stolyarova, D. Stolyarov, K. Bolotin, S. Ryu, L. Liu, K. T. Rim, M. Klima, M. Hybertsen, I. Pogorelsky, I. Pavlishin, K. Kusche, J. Hone, P. Kim, H. L. Stormer, V. Yakimenko, G. Flynn, *Nano Lett.* **2009**, *9*, 332.
[93] D. A. Sanchez, Z. Dai, N. Lu, *Trends Chem.* **2021**, *3*, 204.
[94] L. He, H. Wang, L. Chen, X. Wang, H. Xie, C. Jiang, C. Li, K. Elibol, J. Meyer, K. Watanabe, T. Taniguchi, Z. Wu, W. Wang, Z. Ni, X. Miao, C. Zhang, D. Zhang, H. Wang, X. Xie, *Nat. Commun.* **2019**, *10*, 2851.
[95] M. Lozada-Hidalgo, S. Hu, O. Marshall, A. Mishchenko, A. N. Grigorenko, R. A. W. Dryfe, B. Radha, I. V. Grigorieva, A. K. Geim, *Science* **2016**, *351*, 68.
[96] H. Rostami, F. Guinea, M. Polini, R. Roldán, *npj 2D Mater. Appl.* **2018**, *2*, 51.
[97] V. Shahnazaryan, H. Rostami, *Phys. Rev. B* **2021**, *8*, 085405.
[98] T. P. Darlington, A. Krayev, V. Venkatesh, R. Saxena, J. W. Kysar, N. J. Borys, D. Jariwala, P. J. Schuck, *J. Chem. Phys.* **2020**, *153*, 024702.
[99] K. Yue, W. Gao, R. Huang, K. M. Liechti, *J. Appl. Phys.* **2012**, *112*, 083512.
[100] P. Wang, W. Gao, Z. Cao, K. M. Liechti, R. Huang, *J. Appl. Mech.* **2013**, *80*, 040905.
[101] K. Zollner, P. E. F. Junior, J. Fabian, *Phys. Rev. B* **2019**, *100*, 195126.
[102] P. Johari, V. B. Shenoy, *ACS Nano* **2012**, *6*, 5449.
[103] M. Ghorbani-Asl, S. Borini, A. Kuc, T. Heine, *Phys. Rev. B* **2013**, *87*, 235434.
[104] C.-H. Chang, X. Fan, S.-H. Lin, J.-L. Kuo, *Phys. Rev. B* **2013**, *88*, 195420.
[105] C. Musumeci, *Crystals* **2017**, *7*, 7.
[106] W. Wang, S. Yang, A. Wang, *Sci. Rep.* **2017**, *7*, 8244.
[107] M. Brooks, G. Burkard, *Phys. Rev. B* **2018**, *97*, 195454.
[108] B. Vasic, M. Kratzer, A. Matkovic, A. Nevosad, U. Ralevic, D. Jovanovic, C. Ganser, C. Teichert, R. Gajic, *Nanotechnology* **2013**, *24*, 015303.
[109] J. H. Lee, S. Lee, J. H. Jeon, D. Y. Oh, M. Shin, M. J. Lee, S. Shinde, J.-H. Ahn, C. J. Roh, L. J. Seok, B. H. Park, *NPG Asia Mater.* **2018**, *10*, 1069.
[110] W. Zhou, Y.-Y. Zhang, J. Chen, D. Li, J. Zhou, Z. Liu, M. F. Chisholm, S. T. Pantelides, K. P. Loh, *Sci. Adv.* **2018**, *4*, eaap9096.
[111] C. Zhu, M. Yu, J. Zhou, Y. He, Q. Zeng, Y. Deng, S. Guo, M. Xu, J. Shi, W. Zhou, L. Sun, L. Wang, Z. Hu, Z. Zhang, W. Guo, Z. Liu, *Nat. Commun.* **2020**, *11*, 772.
[112] P. Kun, B. Fulop, G. Dobrik, p. Nemes-Incze, I. E. Lukacs, S. Csonka, C. Hwang, L. Tapaszto, *npj 2D Mater. Appl.* **2020**, *4*, 43.
[113] P. Nemes-Incze, G. Kukucska, J. Koltai, J. Kurti, C. Hwang, L. Tapaszto, L. P. Biro, *Sci. Rep.* **2017**, *7*, 3035.

[114] B. Vasić, M. Kratzer, A. Matković, A. Nevosad, U. Ralević, D. Jovanović, C. Ganser, C. Teichert, R. Gajić, *Nanotechnology* **2012**, *24*, 015303.
[115] C. Lee, Q. Li, W. Kalb, X.-Z. Liu, H. Berger, R. W. Carpick, J. Hone, *Science* **2010**, *328*, 76.
[116] M. V. Rastei, B. Heinrich, J. L. Gallani, *Phys. Rev. Lett.* **2013**, *111*, 084301.
[117] M. V. Rastei, P. Guzmán, J. L. Gallani, *Phys. Rev. B* **2014**, *90*, 041409.
[118] M. Dienwiebel, G. S. Verhoeven, N. Pradeep, J. W. M. Frenken, J. A. Heimberg, H. W. Zandbergen, *Phys. Rev. Lett.* **2004**, *92*, 126101.
[119] J. S. Choi, J.-S. Kim, I.-S. Byun, D. H. Lee, M. J. Lee, B. H. Park, C. Lee, D. Yoon, H. Cheong, K. H. Lee, Y.-W. Son, J. Y. Park, M. Salmeron, *Science* **2011**, *333*, 607.
[120] J. S. Choi, J.-S. Kim, I.-S. Byun, D. H. Lee, I. R. Hwang, B. H. Park, T. Choi, J. Y. Park, M. Salmeron, *Rev. Sci. Instrum.* **2012**, *83*, 073905.
[121] P. Gallagher, M. Lee, F. Amet, P. Maksymovych, J. Wang, S. Wang, X. Lu, G. Zhang, K. Watanabe, T. Taniguchi, D. Goldhaber-Gordon, *Nat. Commun.* **2016**, *7*, 10745.
[122] M. J. Boland, M. Nasseri, D. P. Hunley, A. Ansary, D. R. Strachan, *RSC Adv.* **2015**, *5*, 92165.
[123] J. A. Kellar, J. M. P. Alaboson, Q. H. Wang, M. C. Hersam, *Appl. Phys. Lett.* **2010**, *96*, 143103.
[124] G. Fisichella, S. Di Franco, P. Fiorenza, R. Lo Nigro, F. Roccaforte, C. Tudisco, G. G. Condorelli, N. Piluso, N. Spartá, S. Lo Verso, C. Accardi, C. Tringali, S. Ravesi, F. Giannazzo, *Beilstein J. Nanotechnol.* **2013**, *4*, 234.
[125] G. Fisichella, G. Greco, F. Roccaforte, F. Giannazzo, *Nanoscale* **2014**, *6*, 8671.
[126] S. Sonde, F. Giannazzo, V. Raineri, R. Yakimova, J.-R. Huntzinger, A. Tiberj, J. Camassel, *Phys. Rev. B* **2009**, *80*, 241406.
[127] F. Giannazzo, G. Fisichella, A. Piazza, S. Agnello, F. Roccaforte, *Phys. Rev. B* **2015**, *92*, 081307.
[128] R. Maiti, M. A. S. R. Saadi, R. Amin, V. O. Ozcelik, B. Uluutku, C. Patil, C. Suer, S. Solares, V. J. Sorger, *ACS Appl. Electron. Mater.* **2021**, *3*, 3781.
[129] Y. Peng, M. Que, J. Tao, X. Wang, J. Lu, G. Hu, B. Wan, Q. Xu, C. Pan, *2D Mater.* **2018**, *5*, 042003.
[130] P. Lin, c. Pan, Z. Wang, *Mater. Today Nano* **2018**, *4*, 17.
[131] S. K. Kim, R. Bhatia, T.-H. Kim, D. Seol, J. H. Kim, H. Kim, W. Seung, Y. Kim, Y. H. Lee, S.-W. Kim, *Nanoenergy* **2016**, *22*, 483.
[132] G. d. C. Rodrigues, P. Zelenovskiy, K. Romanyuk, S. Luchkin, Y. Kopelevich, A. Kholkin, *Nat. Commun.* **2015**, *6*, 7572.
[133] M. Zelisko, Y. Hanlumyuang, S. Yang, Y. Liu, C. Lei, J. Li, P. M. Ajayan, P. Sharma, *Nat. Commun.* **2014**, *5*, 4284.
[134] Y. Bai, L. Zhou, J. Wang, W. Wu, L. J. McGilly, D. Halbertal, C. F. B. Lo, F. Liu, J. Ardelean, P. Rivera, N. R. Finney, X.-C. Yang, D. N. Basov, W. Yao, X. Xu, v. Hone, A. N. Pasupathy, X.-Y. Zhu, *Nat. Mater.* **2020**, *19*, 1068.
[135] S. S. Datta, D. R. Strachan, E. J. Mele, A. T. C. Johnson, *Nano Lett.* **2009**, *9*, 7.
[136] E. M. Alexeev, N. Mullin, P. Ares, H. Nevison-Andrews, O. Skrypka, T. Godde, A. Kozikov, L. Hague, Y. Wang, K. S. Novoselov, L. Fumagalli, J. K. Hobbs, A. I. Tartakovskii, *ACS Nano* **2020**, *14*, 11110.
[137] D. J. Trainer, Y. Zhang, F. Bobba, X. Xi, S.-W. Hla, M. Iavarone, *ACS Nano* **2019**, *13*, 8284.
[138] H. Li, A. Chen, L. Wang, W. Ren, S. Lu, B. Yang, Y.-P. Jiang, F.-S. Li, *Appl. Phys. Lett.* **2020**, *117*, 161601.
[139] X. Qian, J. Liu, L. Fu, J. Li, *Science* **2014**, *346*, 1344.
[140] D. Waters, Y. Nie, F. Lüpke, Y. Pan, S. Fölsch, Y.-C. Lin, B. Jariwala, K. Zhang, C. Wang, H. Lv, K. Cho, D. Xiao, J. A. Robinson, R. M. Feenstra, *ACS Nano* **2020**, *14*, 7564.
[141] C. R. Woods, L. Britnell, A. Eckmann, R. S. Ma, J. C. Lu, H. M. Guo, X. Lin, G. L. Yu, Y. Cao, R. V. Gorbachev, A. V. Kretinin, J. Park, L. A. Ponomarenko, M. I. Katsnelson, Y. N. Gornostyrev, K. Watanabe, T. Taniguchi, C. Casiraghi, H.-J. Gao, A. K. Geim, K. S. Novoselov, *Nat. Phys.* **2014**, *10*, 451.
[142] F. R. Eder, J. Kotakoski, K. Holzweber, C. Mangler, V. Skakalova, J. C. Meyer, *Nano Lett.* **2013**, *13*, 1934.
[143] K. Elibol, S. Hummel, B. C. Bayer, J. C. Meyer, *Sci. Rep.* **2020**, *10*, 4839.
[144] K. Elibol, B. C. Bayer, S. Hummel, J. Kotakoski, G. Argentero, J. C. Meyer, *Sci. Rep.* **2016**, *6*, 28485.
[145] S. Hummel, K. Elibol, D. Zhang, K. Sampathkumar, O. Frank, D. Eder, C. Schwalb, J. Kotakoski, J. C. Meyer, B. C. Bayer, *Appl. Phys. Lett.* **2021**, *118*, 103104.
[146] L. D. Landau, E. M. Lifshitz, *Theory of Elasticity*, 2nd revised edition, Vol. *7*, Course on Theoretical Physics, Pergamon Press, Oxford **1970**.
[147] E. Ventsel, T. Krauthammer, *Appl. Mech. Rev.* **2002**, *55*, B72.
[148] A. Pacheco-Sanjuán, R. Batra, *Int. J. Mech. Sci.* **2019**, *163*, 105154.
[149] A. Castellanos-Gomez, M. Poot, G. A. Steele, H. S. J. van der Zant, N. Agraït, G. Rubio-Bollinger, *Adv. Mater.* **2012**, *24*, 772.
[150] A. Castellanos-Gomez, M. Poot, A. Amor-Amorós, G. A. Steele, H. S. J. van der Zant, N. Agraït, G. Rubio-Bollinger, *Nano Res.* **2012**, *5*, 550.
[151] X. Wei, B. Fragneaud, C. A. Marianetti, J. W. Kysar, *Phys. Rev. B* **2009**, *80*, 205407.
[152] F. Liu, P. Ming, J. Li, *Phys. Rev. B* **2007**, *76*, 064120.
[153] L. Zhou, G. Cao, *Phys. Chem. Chem. Phys.* **2016**, *18*, 1657.
[154] R. C. Cooper, C. Lee, C. A. Marianetti, X. Wei, J. Hone, J. W. Kysar, *Phys. Rev. B* **2013**, *87*, 035423.
[155] S. Xiong, G. Cao, *Nanotechnology* **2015**, *26*, 185705.
[156] D. Vella, B. Davidovitch, *Soft Matter* **2017**, *13*, 2264.
[157] U. Komaragiri, M. R. Begley, J. G. Simmonds, *J. Appl. Mech.* **2005**, *72*, 202.
[158] H. Chen, P. Huang, D. Guo, G. Xie, *J. Phys. Chem. C* **2016**, *120*, 29491.
[159] A. Castellanos-Gomez, R. van Leeuwen, M. Buscema, Herre, S. J. van der Zant, G. A. Steele, W. J. Venstra, *Adv. Mater.* **2013**, *25*, 6719.
[160] G.-H. Lee, R. C. Cooper, S. J. An, S. Lee, A. van der Zande, N. Petrone, A. G. Hammerberg, C. Lee, B. Crawford, W. Oliver, J. W. Kysar, J. Hone, *Science* **2013**, *340*, 1073.
[161] Q.-Y. Lin, G. Jing, Y.-B. Zhou, Y.-F. Wang, J. Meng, Y.-Q. Bie, D.-P. Yu, Z.-M. Liao, *ACS Nano* **2013**, *7*, 1171.
[162] C. S. Ruiz-Vargas, H. L. Zhuang, P. Y. Huang, A. M. van der Zande, S. Garg, P. L. McEuen, D. A. Muller, R. G. Hennig, J. Park, *Nano Lett.* **2011**, *11*, 2259.
[163] H. Rasool, C. Ophus, W. Klug, A. Zettl, J. Gimzewski, *Nat. Commun.* **2013**, *4*, 2811.
[164] M. Poot, H. S. J. van der Zant, *Appl. Phys. Lett.* **2008**, *92*, 063111.
[165] C. Wong, M. Annamalai, Z. Wang, M. Palaniapan, *J. Micromech. Microeng.* **2010**, *20*, 1150209.
[166] J. Lee, Z. Wang, K. He, J. Shan, P. X.-L. Feng, *ACS Nano* **2013**, *7*, 6086.
[167] I. W. Frank, D. M. Tanenbaum, A. M. van der Zande, P. L. McEuen, *J. Vac. Sci. Technol., B: Microelectron. Nanometer Struct.–Process., Meas., Phenom.* **2007**, *25*, 2558.
[168] F. Traversi, F. J. Gúzman-Vázquez, L. G. Rizzi, V. Russo, C. S. Casari, C. Gómez-Navarro, R. Sordan, *New J. Phys.* **2010**, *12*, 023034.
[169] S. Sengupta, H. S. Solanki, V. Singh, S. Dhara, M. M. Deshmukh, *Phys. Rev. B* **2010**, *82*, 155432.
[170] S. P. Koenig, N. G. Boddeti, N. L. Dunn, J. S. Bunch, *Nat. Nanotechnol.* **2011**, *6*, 543.
[171] H. Jiang, L. Zheng, Z. Liu, X. Wang, *InfoMat* **2020**, *2*, 1077.

[172] K. Liu, Q. Yan, M. Chen, W. Fan, Y. Sun, J. Suh, D. Fu, S. Lee, J. Zhou, S. Tongay, J. Ji, J. B. Neaton, J. Wu, *Nano Lett.* **2014**, *14*, 5097.
[173] C. Lee, X. Wei, Q. Li, R. Carpick, J. W. Kysar, J. Hone, *Physica Status Solidi B* **2009**, *246*, 2562.
[174] M. Annamalai, S. Mathew, M. Jamali, D. Zhan, M. Palaniapan, *J. Micromech. Microeng.* **2012**, *22*, 105024.
[175] N. Iguiñiz, R. Frisenda, R. Bratschitsch, A. Castellanos-Gomez, *Adv. Mater.* **2019**, *31*, 1807150.
[176] Y. Li, C. Yu, Y. Gan, P. Jiang, J. Yu, Y. Ou, D.-F. Zou, C. Huang, J. Wang, T. Jia, Q. Luo, X.-F. Yu, H. Zhao, C.-F. Gao, J. Li, *NPJ Comput. Mater.* **2018**, *4*, 49.
[177] J. Lee, F. Ye, Z. Wang, R. Yang, J. Hu, Z. Mao, J. Wei, P. X.-L. Feng, *Nanoscale* **2016**, *8*, 7854.
[178] F. Wang, S. Li, M. A. Bissett, I. A. Kinloch, Z. Li, R. J. Young, *2D Mater.* **2020**, *7*, 045022.
[179] Y. Yang, X. Li, M. Wen, E. Hacopian, W. Chen, Y. Gong, J. Zhang, B. Li, W. Zhou, P. M. Ajayan, Q. Chen, T. Zhu, J. Lou, *Adv. Mater.* **2019**, *29*, 1604201.
[180] R. Zhang, V. Koutsos, R. Cheung, *APL Mater.* **2016**, *108*, 042104.
[181] A. Castellanos-Gomez, V. Singh, H. S. J. van der Zant, G. A. Steele, *Ann. Phys.* **2015**, *527*, 27.
[182] G. Wang, Z. Dai, J. Xiao, S. Feng, C. Weng, L. Liu, Z. Xu, R. Huang, Z. Zhang, *Phys. Rev. Lett.* **2019**, *123*, 116101.
[183] W. B. Fichter, *NASA Technical Paper* **1997**, *3658*, 1.
[184] B. H. Tan, J. Zhang, J. Jin, C. H. Ooi, Y. He, R. Zhou, K. Ostrikov, N.-T. Nguyen, H. An, *Nano Lett.* **2020**, *20*, 3478.
[185] C. Di Giorgio, E. Blundo, G. Pettinari, M. Felici, A. Polimeni, F. Bobba, *ACS Appl. Mater. Interfaces* **2021**, *13*, 48228.
[186] J. Zang, S. Ryu, N. Pugno, Q. Wang, Q. Tu, M. J. Buehler, X. Zhao, *Nat. Mater.* **2013**, *12*, 321.
[187] C. Feng, Z. Yi, L. F. Dumée, C. J. Garvey, F. She, B. Lin, S. Lucas, J. Schütz, W. Gao, Z. Peng, L. Kong, *Carbon* **2015**, *93*, 878.
[188] C. Cao, H. F. Chan, J. Zang, K. W. Leong, X. Zhao, *Adv. Mater.* **2014**, *26*, 1763.
[189] C. M. Gabardo, J. Yang, N. J. Smith, R. C. Adams-McGavin, L. Soleymani, *ACS Nano* **2016**, *10*, 8829.
[190] F. Greco, A. Bellacicca, M. Gemmi, V. Cappello, V. Mattoli, P. Milani, *ACS Appl. Mater. Interfaces* **2015**, *7*, 7060.
[191] T. Björkman, A. Gulans, A. V. Krasheninnikov, R. M. Nieminen, *Phys. Rev. Lett.* **2012**, *108*, 235502.
[192] N. Mounet, M. Gibertini, P. Schwaller, D. Campi, A. Merkys, A. Marrazzo, T. Sohier, I. E. Castelli, A. Cepellotti, G. Pizzi, N. Marzari, *Nat. Nanotech.* **2018**, *13*, 246.
[193] N. G. Boddeti, S. P. Koenig, R. Long, J. Xiao, J. S. Bunch, M. L. Dunn, *J. Appl. Mech.* **2013**, *80*, 040909.
[194] X. Liu, N. G. Boddeti, M. R. Szpunar, L. Wang, M. A. Rodriguez, R. Long, J. Xiao, M. L. Dunn, J. S. Bunch, *Nano Lett.* **2013**, *13*, 2309.
[195] P. Cao, K. Xu, J. O. Varghese, J. R. Heath, *Nano Lett.* **2011**, *11*, 5581.
[196] K.-T. Wan, Y.-W. Mai, *Acta Metall. Mater.* **1995**, *13*, 4109.
[197] S. Deng, E. Gao, Z. Xu, V. Berry, *ACS Appl. Mater. Interfaces* **2017**, *9*, 7812.
[198] H. Vandeparre, M. Pineirua, F. Brau, B. Roman, J. Bico, C. Gay, W. Bao, C. N. Lau, P. M. Reis, P. Damman, *Phys. Rev. Lett.* **2011**, *106*, 224301.
[199] M. C. Lemme, S. Wagner, k. Lee, X. Fan, G. J. Verbiest, S. Wittmann, S. Lukas, R. J. Dolleman, F. Niklaus, H. S. J. van der Zant, G. S. Duesberg, P. G. Steeneken, *Research* **2020**, *2020*, 8748602.
[200] T. Mashoff, V. Pratzer, M. Geringer, T. J. Echtermeyer, *Nano Lett.* **2010**, *10*, 461.
[201] J. Bunch, A. M. van der Zande, S. S. Verbridge, W. Frank, D. M. Tanenbaum, J. M. Parpia, H. G. Craighead, P. L. McEuen, *Science* **2007**, *315*, 5811.
[202] N. Morell, A. Reserbat-Plantey, I. Tsioutsios, K. G. Schädler, F. Dubin, F. H. L. Koppens, A. Bachtold, *Nano Lett.* **2016**, *16*, 5102.
[203] C. N. Arutt, M. L. Alles, W. Liao, H. Gong, J. L. Davidson, R. D. Schrimpf, R. A. Reed, R. A. Weller, K. Bolotin, R. Nicholl, T. T. Pham, A. Zettl, Q. Du, J. Hu, M. Li, B. Alphenaar, J.-T. Lin, P. Deb Shurva, S. McNamara, K. Walsh, P. X. L. Feng, B. Homeijer, R. G. Polcawich, R. Proie, J. L. Jones, E. R. Glaser, C. D. Cress, N. Bassiri-Gharb, *Semicond. Sci. Technol.* **2017**, *32*, 013005.
[204] S. S. Verbridge, D. F. Shapiro, H. Craighead, J. M. Parpia, *Nano Lett.* **2007**, *7*, 1728.
[205] H. Xie, S. Jiang, D. A. Rhodes, J. C. Hone, J. Shan, K. F. Mak, *Nano Lett.* **2021**, *21*, 2538.
[206] T. Yildirim, L. Zhang, G. P. Neupane, S. Chen, J. Zhang, H. Yan, M. M. Hasan, G. Yoshikawa, Y. Lu, *Nanoscale* **2020**, *12*, 22366.
[207] M. Šiškins, M. Lee, S. Mañas-Valero, E. Coronado, Y. M. Blanter, H. S. J. van der Zant, P. G. Steeneken, *Nat. Commun.* **2020**, *11*, 2698.
[208] A. Eichler, J. Moser, J. Chaste, I. Zdrojek, M. Wilson-Rae, A. Bachtold, *Nat. Nanotechnol.* **2011**, *6*, 339.
[209] T. Wah, *J. Acoust. Soc. Am.* **1962**, *34*, 275.
[210] D. R. Southworth, H. G. Craighead, J. M. Parpia, *APL Mater.* **2009**, *94*, 213506.
[211] T. Yildirim, J. Zhang, S. Sun, G. Alici, S. Zhang, W. Li, *J. Vib. Acoust.* **2018**, *140*, 034502.
[212] D. T. M. A. H. Nayfeh, *Nonlinear Oscillations*, John Wiley & Sons, New York **1995**.
[213] J. S. Aldridge, A. N. Cleland, *Phys. Rev. Lett.* **2005**, *94*, 156403.
[214] D. Davidovikj, F. Alijani, S. J. Cartamil-Bueno, H. S. J. van der Zant, M. Amabili, P. G. Steeneken, *Nat. Commun.* **2017**, *8*, 1253.
[215] C. Samanta, P. R. Yasasvi Gangavarapu, A. K. Naik, *Appl. Phys. Lett.* **2015**, *107*, 173110.
[216] C. Samanta, N. Arora, A. K. Naika, *Appl. Phys. Lett.* **2018**, *113*, 113101.
[217] F. Guan, P. Kumaravadivel, D. V. Averin, X. Du, *Appl. Phys. Lett.* **2015**, *107*, 193102.
[218] R. Yang, J. Lee, S. Ghosh, H. Tang, R. M. Sankaran, C. A. Zorman, P. X.-L. Feng, *Nano Lett.* **2017**, *17*, 4568.
[219] J. Lee, M. J. Krupcale, P. X.-L. Feng, *APL Mater.* **2016**, *108*, 023106.
[220] F. Ye, J. Lee, P. X.-L. Feng, *Nano Lett.* **2018**, *18*, 1678.
[221] K. He, C. Poole, K. F. Mak, , J. Shan, *Nano Lett.* **2013**, *13*, 2931.
[222] J. O. Island, A. Kuc, E. H. Diependaal, R. Bratschitsch, H. S. J. van der Zant, T. Heine, A. Castellanos-Gomez, *Nanoscale* **2016**, *8*, 2589.
[223] C. Metzger, I. Favero, A. Ortlieb, K. Karrai, *Phys. Rev. B* **2008**, *78*, 035309.
[224] T. J. Kippenberg, K. J. Vahala, *Science* **2008**, *321*, 1172.
[225] M. Aspelmeyer, T. J. Kippenberg, F. Marquardt, *Rev. Mod. Phys.* **2014**, *86*, 1391.
[226] Y. Pang, Z. Yang, Y. Yang, T.-L. Ren, *Small* **2020**, *16*, 1901124.
[227] D. Jiang, Z. Liu, Z. Xiao, Z. Qian, Y. Sun, Z. Zeng, R. Wang, *J. Mater. Chem. A* **2022**, *10*, 89.
[228] D. Akinwande, N. Petrone, J. Hone, *Nat. Commun.* **2014**, *5*, 5678.
[229] J. Kim, Y. Lee, M. Kang, L. Hu, S. Zhao, J.-H. Ahn, *Adv. Mater.* **2021**, *33*, 2005858.
[230] A. Kis, *Nat. Electron.* **2021**, *4*, 853.
[231] S. Das, A. Sebastian, E. Pop, C. J. McClellan, A. D. Franklin, T. Grasser, T. Knobloch, Y. Illarionov, A. V. Penumatcha, J. Appenzeller, Z. Chen, W. Zhu, I. Asselberghs, L.-J. Li, U. E. Avci, N. Bhat, T. D. Anthopoulos, R. Singh, *Nat. Electron.* **2021**, *4*, 786.
[232] P. Sriram, A. Manikandan, F.-C. Chuang, Y.-L. Chueh, *Small* **2020**, *16*, 1904271.
[233] W. G. Song, H.-J. Kwon, J. Park, J. Yeo, M. Kim, S. Park, S. Yun, K.-U. Kyung, C. P. Grigoropoulos, Y. K. Kim, S. Hong, *Adv. Funct. Mater.* **2016**, *26*, 2426.

[234] M. Park, Y. J. Park, X. Chen, Y.-K. Park, M.-S. Kim, J.-H. Ahn, *Adv. Mater.* **2016**, *28*, 2556.
[235] J.-H. Seo, T. Ling, S. Gong, W. Zhou, A. L. Ma, L. Z. Guo, Z. Ma, *Sci. Rep.* **2016**, *6*, 24771.
[236] M. C. Lemme, T. J. Echtermeyer, M. Baus, H. Kurz, *IEEE Electron Device Lett.* **2007**, *28*, 282.
[237] A. Celis, M. N. Nair, A. Taleb-Ibrahimi, E. H. Conrad, C. Berger, W. A. de Heer, *T. A., J. Phys. D: Appl. Phys.* **2016**, *49*, 143001.
[238] K. F. Mak, C. H. Lui, J. Shan, T. F. Heinz, *Phys. Rev. Lett.* **2009**, *102*, 256405.
[239] M. M. S. Abdelnabi, E. Blundo, M. G. Betti, G. Cavoto, E. Placidi, A. Polimeni, A. Ruocco, K. Hu, Y. Ito, C. Mariani, *Nanotechnology* **2021**, *32*, 035707.

Cinzia Di Giorgio is a Researcher at the Physics Department of University of Salerno (Italy). She received her Ph.D. in Physics in 2016, she worked for three years (2016–2019) as a postdoctoral researcher in the Scanning Probe Microscopy and Nano-Matter Laboratory, at the University of Salerno (Italy), and she boasts numerus long- and short-stay visits in several condensed matter physics' laboratories in Europe and USA. Her research focuses on the investigation of the microscopic, mechanical, and electronic properties of low-dimensional materials.

Elena Blundo is a Ph.D. student in Physics at La Sapienza, University of Rome (Italy), in the Optical Spectroscopy of Nanostructured Materials Laboratory led by Prof. Antonio Polimeni. Her activity is mostly focused on the study of two-dimensional materials and semiconductors. In particular, she is investigating the opto-electronic and mechanical properties of two-dimensional crystals, the effects of high strain on their peculiar properties (both experimentally and theoretically), and their interaction with hydrogen beams. She is also an international Taekwondo player in the field of "Poomsae" and Head Coach of the Youth sector of the Italian National Poomsae Team.

Giorgio Pettinari is a staff researcher at the Institute for Photonics and Nanotechnologies of the National Research Council of Italy. He received his Ph.D. in Materials Science from Sapienza University of Rome (Italy, 2008), and was an Assistant Researcher at the High Field Magnet Laboratory of the Radboud University of Nijmegen (The Netherlands, 2009–2011) and a Marie Curie Research Fellow at the University of Nottingham (UK, 2011–2013). His research interests range from the experimental investigation (optics, transport, surface probe microscopies) to the micro- and nano-fabrication of low-dimensional systems, photonic and plasmonic devices, as well as of detector arrays for astrophysical applications.

Marco Felici is an Associate Professor at the Physics Department of Sapienza University of Rome (Italy). He received his Ph.D. in Materials Science in 2007, and he worked for four years (2007–2011) as a postdoctoral researcher in the Laboratory of Physics of Nanostructures, at the Ecole Polytechnique Fédérale de Lausanne (EPFL, Switzerland). His research focuses on the investigation of the optical properties of low-dimensional systems (eventually integrated with photonic structures) and of the effects of their interaction with atomic hydrogen.

Fabrizio Bobba is an Associate Professor at the Physics Department of University of Salerno (Italy). He received his Ph.D. in Physics in 1998, and since 2018 he leads the Scanning Probe Microscopy and Nano-Matter Laboratory, at the University of Salerno (Italy). During his post-doctoral activity, he visited numerus condensed matter physics' laboratories in Europe, for long- and short-stays. Since 2016 he has collaborated actively with several institutions in Italy and USA, on the investigation of the microscopic, mechanical, and electronic properties of low-dimensional materials

Antonio Polimeni received his Ph.D. in Physics in 1997. He is an Associate Professor at Sapienza University (Rome, Italy) and coordinates the "Optical Spectroscopy of Nanostructured Materials" group. He worked (1997–1999) at the Nottingham University (UK), where he investigated the optical, transport and laser applications of quantum dots. Since 2000, he is at Sapienza University working on the electronic and optical properties of nanostructured semiconductors. Part of his activity comprises the magneto-optical properties of nanowires and other systems studied at high magnetic field facilities. Recently, he pioneered the strain engineering of the electronic and mechanical properties of two-dimensional materials by hydrogen irradiation.